

國立交通大學

電子物理學系

博士論文

氮化銦鎵/氮化鎵量子井聯合態密度的變化及 V 型

結構對元件特性的影響

Optical joint density of states and effects of V-shaped structures in

InGaN/GaN quantum wells

研究生：王俞授

指導教授：陳振芳 博士

中華民國一百零一年六月

氮化銦鎵/氮化鎵量子井聯合態密度的變化及 V 型結構對元件特  
性的影響

Optical joint density of states and effects of V-shaped structures in  
InGaN/GaN quantum wells

研 究 生：王俞授

Student : Yu-shou Wang

指 導 教 授：陳振芳

Advisor : Dr. Jenn-Fang Chen

國 立 交 通 大 學

電 子 物 理 學 系

博 士 論 文

A Thesis

Submitted to Department of Electro-physics

College of Science

National Chiao Tung University

in partial Fulfillment of the Requirements

for the Degree of

Master

In

Electro-physics

June 2012

Hsinchu, Taiwan, Republic of China

中華民國一百零一年六月

## 致謝

漫長的六年博士生涯期間，經歷過各種嚴峻挑戰，從執行計畫遇到無法突破的瓶頸、發表論文不斷地被退稿、實驗上不斷出現與預期不符的結果以及實驗機台遇到突發的故障，然而這些挫折隨著持續不斷的挑戰被一一克服了，並且也順利的完成學位口試，此時我深刻體會到，這幾年不斷失敗的過程與歷練比贏得博士學位更有價值，我也會不斷地警惕要時時刻刻保持謙虛學習的態度進入社會。

首先感謝我的指導教授陳振芳老師給予我充分的自由從事研究並適時的給予指導，也特別感謝我的共同指導教授陳乃權老師，從我大學專題生時就給予我特別的關懷，非常感激你多年來的苦心栽培與指導，我會銘記在心。

感謝教導我 MOCVD 的施權峰老師以及感謝 MOCVD 實驗室的狗海與大鳥從大學一路到博士班的陪伴，一起體會研究生的辛酸，一起打籃球相約到台北看晚場的電影，讓我的求學過程一點都不寂寞，感謝每次都在旁邊笑的學弟俊逸，沒有你的幫忙我無法順利完成我的論文，感謝阿吉哥的鼓勵與幫忙，感謝脾氣火爆的軍人建茗、球技驚讚的小葉與竣翔、愛打壘球的鈺翔及正妹學妹莞潔在實驗室的幫忙，替實驗室增添不少樂趣。

感謝畢業的邱安平學長，在工作之餘還時常回來實驗室關心學弟妹的狀況並提供寶貴的建議，感謝建元學長和傑哥，你們都是一路陪伴我從碩士班到博士班一起努力打拼的好朋友。感謝渠哥及仁智學長，在執行計畫中給予我寶貴的意見和鼓勵。

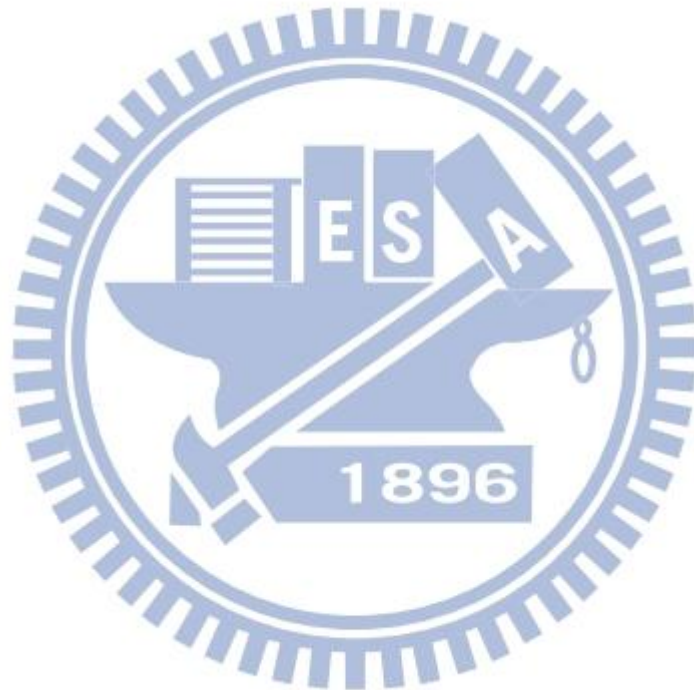
感謝交大實驗室的同学江振豪，時常給予我寶貴的資訊和鼓勵，感謝學弟謝孟謙，雖然你每次講話都酸酸的，但是實際上還是很有義氣地給予我協助，感謝政鴻時常在研究上的交流，讓我獲益良多，也感謝陪我去日本吃鰻魚飯的家峰和學弟妹亞青、國豪、俊泓、哲倫、敬恩及家偉在口試期間的幫忙。

另外特別感謝一路從碩士班到博士班陪伴我執行計畫的好夥伴宥楠學長，我們一起熬夜做實驗，一起討論研究的進度，一起分享生活的喜怒哀樂，甚至畢業後也一直關心我的求學及找工作的狀況，你真的幫助我太多太多了，你不但是我的好學長也是我最好的

朋友，真的由衷的感激。

感謝我的父母與弟弟，有了你們長期在背後默默地支持與陪伴，讓我能夠無憂無慮的完成學業，謝謝你們。

最後感謝我的女朋友李鈞婷，從我碩士班開始就不離不棄的陪伴我到現在，在求學過程中的酸甜苦辣我們都一起經歷過，相信將來會成為我們共同美好的回憶。



俞授

謹識於新竹風城交大 民國一百零一年六月

# 氮化銦鎵/氮化鎵量子井聯合能態密度的變化及 V 型結構對 元件特性的影響

研究生：王俞授

指導教授：陳振芳 博士

國立交通大學電子物理研究所

## 摘 要

由於 III-V 族氮化鎵具有較寬的材料能隙，再搭配銦及鋁成份的調變，其能隙可從 0.7eV 到 6.2eV，涵蓋了所有可見光的部分。因此 III-V 族氮化物適合作為發光二極體的材料，近年來更被廣泛的應用在指示燈、顯示器的背光源及照明上，然而受限其磊晶基板的選擇，目前較為普遍使用的藍寶石基板與氮化鎵材料存在著極大的晶格不匹配差異，因此氮化鎵磊晶結構易形成密度高達  $10^8 \sim 10^{10} \text{cm}^{-2}$  的貫穿式差排。貫穿式差排一般被認為是非幅射複合中心，會造成元件的發光效率下降，然而實際上氮化鎵藍光二極體的發光效率並沒有顯著的下降，這些特徵被認為可能來自銦原子群聚現象所產生的影響，並持續受到矚目。

本研究是利用有機金屬氣相磊晶機台成長氮化鎵發光二極體元件並針對其複合機制進行討論。我們引入一套自發性幅射光譜模型可用來描述磷化鋁鎵銦及氮化銦鎵發光二極體之螢光光譜，並可直接透過元件之螢光光譜，得到其量子井之聯合能態密度分佈，此方法所取得之聯合能態密度分佈與光電流量測所得到的吸收光譜相符。進一步的利用聯合能態密度分佈分析不同波長之氮化物發光二極體(紫光、藍光、綠光)隨電流變化的影響，發現波長隨電流增加所產生之藍移現象與聯合能態密度的變化息息相關。該現象可以解釋為當外加電流時，量子井的極化現象受到額外注入的載子而產生屏蔽效應，進而產生波長藍移。而低能態之聯合能態密度則是反應出銦原子群聚所形成之局部能態的現象，並導致較寬的螢光光譜。

另外，透過變溫光激螢光及時間解析螢光光譜分析載子在氮化物發光二極體中之動態行為。研究發現輻射複合的位置主要發生在銜聚集所形成之局部低能態，此局部低能態可以有效的捕捉載子防止載子擴散至貫穿式差排的位置產生非輻射複合使得發光效率下降。

最後我們研究 V 型結構於量子井對氮化物發光二極體元件的影響。V 型結構是透過貫穿式差排所形成，其側邊所形成之較窄的多重量子井結構可提供較大的能隙，防止一般量子井中的載子與貫穿式差排產生非輻射複合。研究並指出，透過磊晶填平 V 型結構可形成電流阻擋層，進一步抑制電流的注入貫穿式差排，因此氮化物發光二極體可透過此磊晶結構的調整大幅的改善其發光效率。



# Optical joint density of states and effects of V-shaped structures in InGaN/GaN quantum wells

Student : Yu-Shou Wang

Advisor : Dr. Jenn-Fang Chen

Department of Electrophysics  
National Chiao Tung University

## Abstract

The wide range of energy gaps in group-III nitride-based materials allows for adjustment of the direct band gap energies from 0.7eV to 6.2eV by varying the compositions of In and Al contents, including all visible energy. Therefore, among the many commercial applications of nitride-based light-emitting diodes (LEDs) include indicator lights, backlight displays and light bulbs. However, these devices typically have a high density of dislocations ( $10^8$ – $10^{10}$ cm<sup>-2</sup>) that thread through active regions, due to the significant lattice mismatch between nitride epilayers and sapphire substrates. Although being identified as efficient nonradiative centers, threading dislocations do not significantly degrade the performances of LEDs. This feature is recognized as the effects of self-formed In-rich regions in InGaN quantum wells and continues to draw considerable attention, thus warranting further study.

This work studies the recombination mechanism of InGaN LEDs grown by metal organic chemical vapor deposition. An analytical method is also developed for determining the optical joint densities of states of AlGaInP LEDs and InGaN LEDs. Capable of extracting the optical joint density of states, the proposed method can be obtained from photoluminescence (PL) or electroluminescence spectrum of the devices, results of which correlate with the absorption spectrum evaluated by photo current measurements. Furthermore, the optical joint densities of

states of three InGaN LEDs with different emission wavelengths (violet, blue and green) operated at various currents are examined. Experimental results indicate that the blueshift of the emissions with an increasing current is related to the variation in optical joint densities of states and can be attributed to the carrier screening of quantum-confined Stark effect induced by the piezoelectric field. Tails at the low-energy end of the density of states, corresponding to localized states, is found, and these tails broaden the spectra of the devices.

Moreover, the carrier dynamic process of InGaN LEDs is investigated by using temperature dependence of PL and time-resolved PL. Experimental results indicate that the internal high efficiency of InGaN LEDs is mainly related to the spontaneously formed In-rich regions. The electron-hole pairs injected into wells typically drift to low-energy locations and then recombine radiatively rather than diffuse to dislocations.

Furthermore, the extent to which V-shaped structures affect the internal quantum efficiency of nitride LEDs is investigated. The V-shaped structures are initiated at threading dislocations, subsequently enclosing them. Since quantum wells grown on the sidewalls of V-shaped structures are thin, electron and hole transition energy is higher than that of normal wells due to the quantum confinement effect. This increased energy functions as a potential barrier, preventing carriers in normal wells from diffusing into dislocations. Moreover, our sample contains an unintentionally formed current blocking mechanism, suppressing the current density in the region around dislocations. Since both possible paths have been blocked, electrically injected electron-hole pairs cannot generally reach the dislocations, reducing drawbacks associated with threading dislocations in nitride LEDs.



## Table of contents

Acknowledgements .....	i
Abstract (in Chinese) .....	iii
Abstract.....	v
Table of contents.....	vii
List of figures .....	x
<b>Chapter 1 Introduction .....</b>	<b>1</b>
Reference.....	4
<b>Chapter 2 Background .....</b>	<b>5</b>
2.1 Epitaxial technique.....	5
2.2 MOCVD .....	5
2.3 Photoluminescence .....	7
2.4 Electroluminescence.....	7
2.5 Scanning electron microscope.....	7
2.6 Transmission electron microscopy .....	8
Reference.....	9
<b>Chapter 3 Spontaneous emission spectrum in light-emitting diodes .....</b>	<b>14</b>
3.1 Introduction .....	14
3.2 Optical joint density of state.....	14
3.3 Spontaneous emission .....	17
3.4 Absorption .....	18
3.5 Emission spectrum .....	19
3.6 Photo current .....	20
3.7 Conclusion.....	22
Reference.....	23

**Chapter 4 Optical joint density of states in InGaN/GaN multiple-quantum-well**

**light-emitting diodes** ..... 36

4.1 Introduction ..... 36

4.2 Current dependent..... 38

4.3 Temperature dependent..... 42

Reference ..... 45

**Chapter 5 Diffusion-controlled effects of luminescence efficiency in InGaN/GaN**

**light-emitting diodes** ..... 63

5.1 Introduction ..... 63

5.2 Experiments ..... 64

5.3 Transmission electron microscopy ..... 65

5.4 Photoluminescence ..... 65

5.5 Time-resolved photoluminescence ..... 66

5.6 Radiative lifetime ..... 68

5.7 Nonradiative lifetime ..... 70

5.8 Conclusion ..... 74

References ..... 75

**Chapter 6 Potential barriers and current-blocking structures induced by V-shaped**

**pits in InGaN/GaN light-emitting diodes** ..... 88

6.1 Introduction ..... 88

6.2 Experiments ..... 89

6.3 Transmission electron microscopy ..... 89

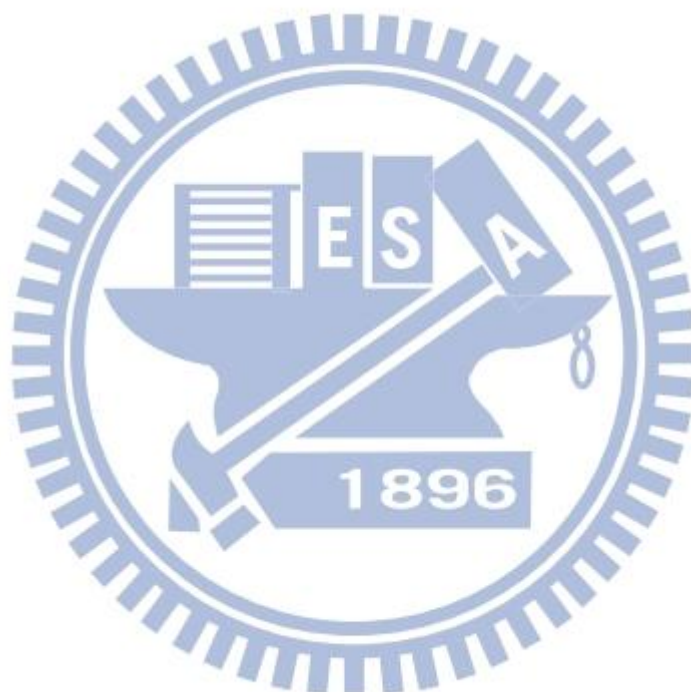
6.4 Photoluminescence ..... 98

6.5 Electroluminescence ..... 92

6.6 Conclusions ..... 94

References ..... 96

Publish list .....	111
A. Refereed Papers .....	111
B. Conference papers .....	111
a. International conference.....	111
b. Domestic conference .....	113



## List of figures

Fig. 2.1 MOCVD Aixtron 200/4 RF-s .....	10
Fig. 2.2 Deposition process .....	10
Fig. 2.3 Reactor of MOCVD .....	11
Fig. 2.4 Sapphire substract and susceptor.....	11
Fig. 2.5 RF-Coil and lightpipe.....	12
Fig. 2.6 In-situ reflectometry .....	12
Fig. 2.7 PL measurement .....	13
Fig. 2.8 EL measurement.....	13
Fig. 3.1 Dispersion relation of electron-hole recombination and phonon emission.....	24
Fig. 3.2 Density of states in two-dimensional .....	25
Fig. 3.3 Theoretical emission spectrum in two-dimensional quantum structure.....	25
Fig. 3.4 Theoretical emission spectrum of an LED .....	26
Fig. 3.5 Sample structure of an AlGaInP LED.....	27
Fig. 3.6 Power spectra of the LED measured at 10 mA, and the temperature ranges from 400 to 120 K .....	28
Fig. 3.7 Photon density spectra measured at 10 mA on a semi-log scale and the temperature ranges from 400K to 120K .....	28
Fig. 3.8 Junction temperature obtained from gradients of high-energy tails in an EL spectrum at 300K.....	29
Fig. 3.9 Dependences of junction temperatures on ambient temperatures obtained from gradients of high-energy tails .....	29
Fig. 3.10 Temperature dependence of optical joint densities of states form 400K to 120K .....	30
Fig. 3.11 Sample structure of the red LED.....	31

Fig. 3.12 Sample structure of the yellow LED .....	31
Fig. 3.13 Sample structure of the yellow-green LED.....	32
Fig. 3.14 Photo current spectrum and EL spectrum of the red LED .....	32
Fig. 3.15 Photo current spectrum and EL spectrum of the yellow LED .....	33
Fig. 3.16 Photo current spectrum and EL spectrum of the yellow-green LED .....	33
Fig. 3.17 Simulation of the DBR.....	34
Fig. 3.18 Absorption spectrum of GaP in red LED .....	34
Fig. 3.19 Absorption spectrum of GaP in yellow LED.....	35
Fig. 3.20 Absorption spectrum of GaP in yellow-green LED .....	35
Fig. 4.1 EL spectra of (a) violet, (b) blue, and (c) green InGaN/GaN-based LEDs at various currents from 10 to 80 mA at 300K. Emission peak shifts in the three spectra are 0 meV, 19 meV, and 37 meV, respectively .....	49
Fig. 4.2 Relative optical joint density of states in violet, blue, and green LEDs under currents from 10 to 80 mA, calculated by dividing EL spectra by thermal distribution.....	50
Fig. 4.3 Band diagrams and wave functions of elections and holes under (a) piezoelectric field and (b) screened piezoelectric field.....	51
Fig. 4.4 Theoretical emission spectra obtained by two-dimensional quantum structure at various currents from 10 to 80 mA at 300K.....	53
Fig. 4.5 Experimental and theoretical EL peak shifts with current in blue (green) LED are denoted by solid circles (solid squares) and open circles (open squares), respectively .....	54
Fig. 4.6 The FWHMs of the experimental spectra and simulated spectra for violet, blue and green LEDs.....	56

Fig. 4.7 PL spectra of an LED at various temperatures from 20 to 340K .....	57
Fig. 4.8 The emission peak positions of the PL spectra at various temperatures from 20 to 340K .....	57
Fig. 4.9 Relative optical joint density of states under temperatures from 20 to 340K, calculated by dividing PL spectra by thermal distribution.....	58
Fig. 4.10 The linear fitted lines of the steep increased of optical joint density of states at 140K, 240K and 340K.....	58
Fig. 4.11 The theoretical emission spectra obtained by two-dimensional quantum structure from 20 to 340K .....	59
Fig. 4.12 The optical joint density of states with eliminating linear fitted lines at 140K, 240K and 340K.....	60
Fig. 4.13 The theoretical emission spectra obtained by localized states from 20 to 340K .....	60
Fig. 4.14 The peak positions of experimental emission spectrum and theoretical emission spectrum obtained by two-dimensional quantum structure and localized states from 60 to 340K .....	61
Fig. 4.15 The experimental emission spectrum and theoretical emission spectrum obtained by two-dimensional quantum structure and localized states at (a) 140 K and (b) 340K.....	62
Fig. 5.1 Diffusion-controlled kinetics of recombination process for line-sink defects .....	77
Fig. 5.2 Cross-sectional TEM image of the LED structure. Inset: magnified TEM shows a dislocation thread through the active layers where point A is the location of active layers and point B is the location of a dislocation .....	78
Fig. 5.3 Temperature dependence of PL spectra.....	79
Fig. 5.4 The fitted Arrhenius plot of the PL intensity.....	80
Fig. 5.5 (a) Temperature dependence of TRPL (b)Temperature dependence of the PL lifetimes .....	81

Fig. 5.6. (a) Arrhenius plot of the PL intensity. (b) The temperature dependence of carrier lifetime, radiative lifetime and nonradiative lifetime, respectively .....	82
Fig. 5.7 Schematic band diagram of the recombination processes with carriers and dislocations.....	83
Fig. 5.8 (a) PL spectrum at 20K. (b) PL decay time as function of the emission energy ..	84
Fig. 5.9 The Schematic representation of localized excitonic states and processes in GaAs <sub>1-x</sub> P <sub>x</sub> alloys .....	85
Fig. 5.10 The PL spectrum at 20K with PL decay time as function of the emission energy .....	86
Fig. 5.11 Temperature dependence of nonradiative lifetime. The trend of nonradiative lifetime with varied temperature is controlled by diffusivity .....	87
Fig. 6.1 Sample structure.....	98
Fig. 6.2 (a) Cross-sectional TEM image of the LED structure. (b) The magnified image of a V-shaped pit. The well grown on the sidewall is narrower than that on the c-plane .....	99
Fig. 6.3 The Cross-sectional TEM images of the MQWs on normal plane .....	100
Fig. 6.4 (a) These V-shaped pits have a six-wall structure with the walls corresponding to the six symmetrical {10 $\bar{1}$ 1} planes. (b) The void associated with V-shaped pits can be filled by <i>p</i> -type layers.....	101
Fig. 6.5 (a) Cross-sectional TEM image of the LED structure. (b) Magnified image of a V-shaped pit. The dashed line shows one quantum well, and A, B, and C identify three different points in the well .....	102
Fig. 6.6 (a) The PL spectra measured at different temperatures. (b) The log scale of the PL spectra .....	103
Fig. 6.7 (a) The PL spectra measured at different temperatures. (b) The PL intensities and intensity ratio of the high-energy peak and main peak in (a) .....	104
Fig. 6.8 Band diagram of the well along the dashed line (Fig. 1(b)). A, B, and C	

denote different points and correspond to A, B, and C in Fig. 1(b), respectively.

The solid lines denote the conduction band and valence band edges, while

dashed lines denote the ground-states of electrons and holes. The electrons

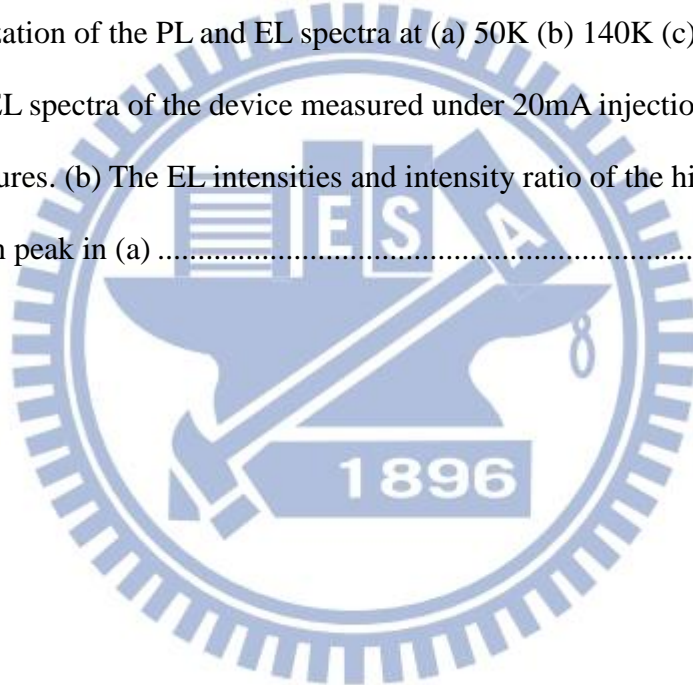
and holes are denoted by solid and empty circles, respectively ..... 105

Fig. 6.9 The EL spectra of the device measured under 20mA injection at different temperatures ..... 106

Fig. 6.10 The EL spectra of the device measured under 20mA injection in the different range of temperatures. (a) 60K - 160K (b) 170K – 300K ..... 107

Fig. 6.11 Normalization of the PL and EL spectra at (a) 50K (b) 140K (c) 300K ..... 109

Fig. 6.12 (a) The EL spectra of the device measured under 20mA injection at different temperatures. (b) The EL intensities and intensity ratio of the high-energy peak and main peak in (a) ..... 110





# Chapter 1 Introduction

Gallium nitride (GaN) is a wurtzite crystal structure with wide bandgap, high heat capacity, high breakdown voltage and high thermal conductivity [1]. Therefore, these materials are commonly used in many high power devices, such as detectors, high power amplifiers, high electron mobility transistors (HEMTs), light-emitting diodes (LEDs) and laser diodes (LDs) [2].

GaN of high crystalline quality can be obtained by using low temperature deposited buffer layer technology. This technology successfully led to the commercialization of high performance of nitride based devices. In recently years, nitride LEDs are widely used in many applications due to their special properties, such as outdoor display, backlighting, traffic signals and illumination. The dramatic increase of the development can be mainly attributed to the improvement of the light efficiency of these devices. However, due to the significant lattice mismatch between nitride epilayers and sapphire substrates (around 13%) [3], these devices typically have a high density of dislocations ( $10^8$ – $10^{10}$  cm<sup>-2</sup>) that thread through active regions. Although threading dislocations have been identified as efficient nonradiative centers, the performances of LEDs are not significantly decreased by these dislocations [4]. Although much investigation of these structures has been reported in decades, the mechanism of emission luminescence is still much left unknown. Therefore, we aimed at the recombination mechanism of the nitride LEDs. In chapter 2, we introduced the experimental procedures of our research. The InGaN/GaN-based LEDs in our work were grown by using metal organic chemical vapor

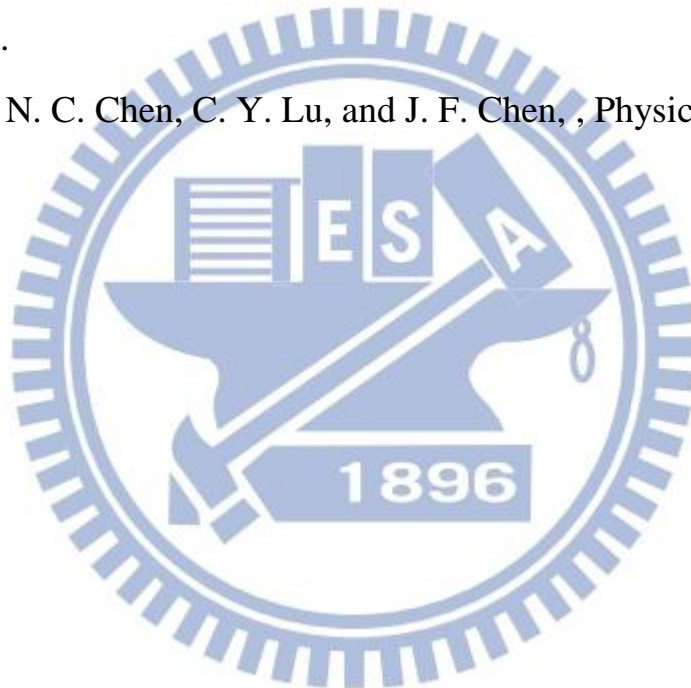
deposition (MOCVD). Following crystal growth, the wafers were processed to form standard LEDs for electrical injection measurements. In chapter 3, a model for describing the shape of the spontaneous emission spectrum from a quantum-well structure [5] was presented. Based on this model, the coexisting carrier thermal broadening and effective band gap broadening in the spontaneous emission spectrum can be separated from each other. In chapter 4, the optical joint densities of states of three InGaN/GaN-based LEDs with different emission wavelengths (violet, blue and green) operated at various currents was investigated. The results indicate that the blueshift of the emission with increasing current is related to the variation in optical joint density of states. Thus, the blueshift is ascribed to the screening of the piezoelectric field by carriers [6]. A tail at the low-energy end of the density of states, corresponding to localized states, was found, and the presence of these tails broadens the spectra of the devices. In chapter 5, the recombination process in InGaN/GaN LEDs by temperature dependence of photoluminescence (PL) and time-resolved photoluminescence (TRPL) was investigated. The decrease of luminescence efficiency with temperature is related to the increase of radiative lifetime and decrease of nonradiative lifetime. Since threading dislocations which recognized as nonradiative center are locally distributed, the diffusion-controlled kinetic should be considered. Our results exhibited that the nonradiative lifetime is mainly attributed to the diffusion-controlled kinetic rather than Shockley-Read-Hall (SRH) theory and in agreement with the theoretical result. In Chapter 6, the influences of V-shaped pits on the internal quantum efficiency of nitride LEDs were investigated. The V-shaped pits are initiated at threading dislocations and, thus, enclose them. Since quantum wells grown on the sidewalls of V-shaped pits are thin, electron and hole transition energy is higher

than that of normal wells due to the quantum confinement effect. This increased energy acts as a potential barrier, preventing carriers in normal wells from diffusing into dislocations. Moreover, an unintentionally formed current blocking mechanism exists in our sample, and can suppress the current density in the region around dislocations. Since both possible paths have been blocked, electrically injected electron-hole pairs cannot generally reach the dislocations and, thus, the drawbacks associated with threading dislocations in nitride LEDs are effectively reduced.



## Reference

- [1] J. Karpinski and S. Porowski, *J. Cryst. Growth* 66(1) 11 (1984)
- [2] S. Nakamura and G. Fasol, *The blue laser diode*, Springer-Verlag, Berlin, pp.277 (1997)
- [3] S. Nakamura, T. Mukai, M. Senoh, and N. Iwasa, *J. Appl. Phys.* 31(2B), L139 (1992)
- [4] S. Nakamura, *IEICE Trans. E83-C(4)*, 529 (2000)
- [5] N. C. Chen, C. M. Lin, C. Shen, W. C. Lien, and T. Y. Lin, *Opt. Express* **16**, 20759 (2008).
- [6] Y. S. Wang, N. C. Chen, C. Y. Lu, and J. F. Chen, *Physica B.* 406, 4300 (2011).



# Chapter 2 Background

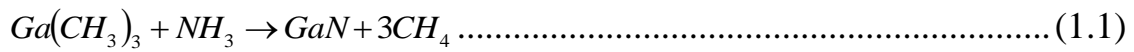
## 2.1 Epitaxial technique

Many epitaxial techniques are available for growth of semiconductor materials, such as liquid-phase epitaxy (LPE), hydride vapor-phase epitaxy (HVPE), molecular-beam epitaxy (MBE), chemical-beam epitaxy (CBE) and metal organic chemical vapor deposition (MOCVD) [1]. In recent years, high quality epitaxial III-V films and heterostructures for devices have been accomplished by MOCVD technique. MOCVD is a nonequilibrium growth technique relies on vapor transport of the precursors and subsequent reactions of group III alkyls and group V hydrides in a heated zone. This technique originated from Manasevit (1968) who demonstrated that triethylgallium (TEGa) and arsine deposited single crystal GaAs pyrolytically in an open tube cold-water reactor. Manasevit (1960) [2-4] and Hess (1979) subsequently expanded the use of this technique for growth of GaAsP, GaAsSb, and Al containing compound. Today, the MOCVD techniques are frequently used for commercial production operations.

## 2.2 MOCVD

In this study, MOCVD Aixtron 200/4 RF-s was used [5], as shown in Fig. 2.1. It is a system for epitaxial growth of uniform layers of all III-V and nitride semiconductors. It can be used in research and development as well as in production areas. The chemical reaction of GaN is using triethylgallium (TEGa) or trimethylgallium (TMGa) and ammonia ( $\text{NH}_3$ ) as source gases for group III and V species, respectively. The precursors are carried to the reaction chamber

by a carrier gas such as hydrogen (H<sub>2</sub>) or nitrogen (N<sub>2</sub>). Figure 2.2 shows the basic reaction GaN and can be briefly described as below:



The precursors do not mix until they reach the chamber, as shown in Fig. 2.3, and the chemical reaction of precursors can occur at the surface of the substrate by controlling the temperature of the substrate. The substrates usually rests on a block of graphite called a susceptor (Fig. 2.4) that can be heated by a radio frequency (RF) coil, as shown in Fig. 2.5. The reactor of the MOCVD is a chamber of a material that does not react with chemicals being used. It must withstand high temperatures. This chamber is composed of liner, a susceptor, gas injection units, and temperature control units. The cooling water must be flowing through the channels within the reactor walls to prevent overheating. In chamber, only the susceptor is heated that gases do not react before they reach the wafer surface. To enhance the uniformity of the deposited films, a rotating susceptor was used. The horizontal reactor permits the handling of up to 1 x 4 inch wafers and the pressure of the system can be pumped from 1000 to 10<sup>-3</sup> mbar. The wafer size we used is 2 inch. Basically, the reactor is operated under 50~100 mbar. The rotation rate is kept in 100~120 rpm and controlled by gas flow while the epilayers were growth. The MO sources enter the reactor chamber by carrier gases and stream outward across the deposition zone. In the same time, the susceptor is heated and the deposition reactions on the substrate occur. It is heated with an RF-Coil using the reaction of RF-Frequency generated by an RF-Generator and an oscillator. The temperature can be heated to 1150 °C and measured by a lightpipe. During growth process, the growth-rate and crystalline quality of the epilayers can be observed directly by the In-situ

reflectometry, as shown in Fig. 2.6. It is used to monitor the reflectance between substrate and epilayers [6,7].

### **2.3 Photoluminescence**

Photoluminescence (PL) is a process in which a substance absorbs photons and then re-radiates photons, as shown in Fig. 2.7. In quantum mechanism, this can be described as an excitation to a higher energy state and then a return to a lower energy state accompanied by the emission of a photon. Therefore, PL can be used as a break-less analysis technology which can reveal the band gap and the carrier transportation behaviors of materials. This is an important technique for measuring the purity and crystalline quality of semiconductor such as GaAs, InP and GaN. In this work, the samples were excited by a 325nm HeCd laser. In addition, some variation of PL measurements was used, such as photoluminescence excitation (PLE) and time-resolved photoluminescence (TRPL).

### **2.4 Electroluminescence**

Electroluminescence (EL) is an optical phenomenon and electrical phenomenon in which a material is produced by current injection and usually measured on processed samples, as shown in Fig. 2.8. It is produced when an electric current is passed through a semiconductor and as excited electrons pass over these holes, they are emitted into the free air as particles known as photons. EL is the results of radiative recombination of electrons and holes in a material.

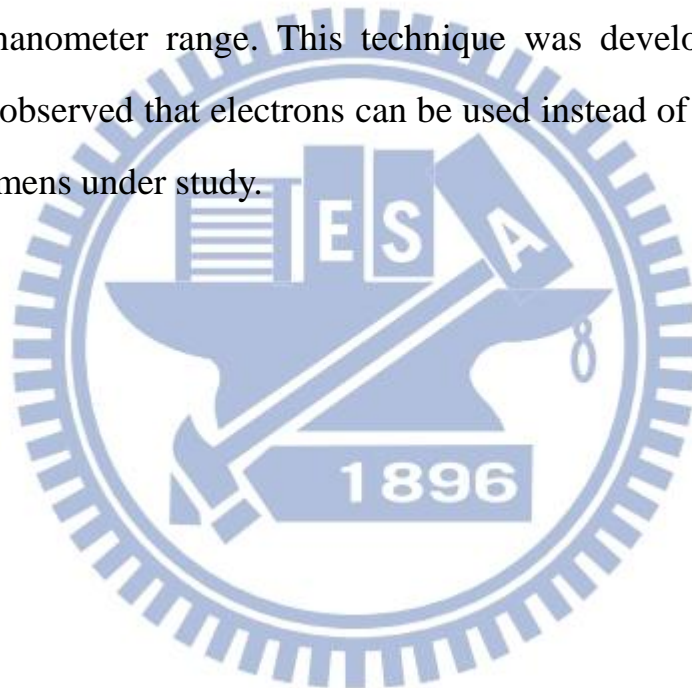
### **2.5 Scanning electron microscope**

Scanning electron microscope (SEM) is images a sample by scanning it with a high-energy beam of electrons. SEM is one of the widely used tools of modern science for studying morphology and composition of biological and physical materials. It is used to measure the surface properties such as surface topography,

composition and electrical conductivity. Moreover, the images of the measurement can magnify up to 100,000x without the need for extensive sample preparation and without damaging the sample. In this work, the JSM-7000F SEM was used.

## **2.6 Transmission electron microscopy**

Transmission electron microscopy (TEM) is a microscopy technique that uses electron beams instead of light to transmit through a very thin film and images the resolution of the thin film allowing for magnification of up to 100,000x and nanometer range. This technique was developed in the 1930s when scientists observed that electrons can be used instead of light to "magnify" objects or specimens under study.





## Reference

- [1] G. B. Stringfellow. Reports on progress in Physics 45 469 (1982)
- [2] H. M. Manasevit, Appl. Phys. Lett. 116 1725 (1969)
- [3] H. M. Manasevit and W. I. Simpson. J. Electrochem. Soc. 12 156 (1968)
- [4] H. M. Manasevit. J. rys. Growth 13/14 306 (1972)
- [5] R. A. Talalaev, E. V. Yakovlev, S. Yu. Karpov, Yu. N. Makarov, O. Schoen, M. Heuken, G. Strauch and Holger Juergensen, MRS Internet J. Nitride Semicond. Res. 4, 5 (1999)
- [6] C. Kirchner, and M. Seyboth, Dept. of Optoelectronics, University of Ulm, Annual Report 18 (1999)
- [7] K. Christiansen, M. Luennenbuerger, B. Schineller, M. Heuken, and H. Juergensen, Opto-electro. Rev 10(4) 237 (2002)

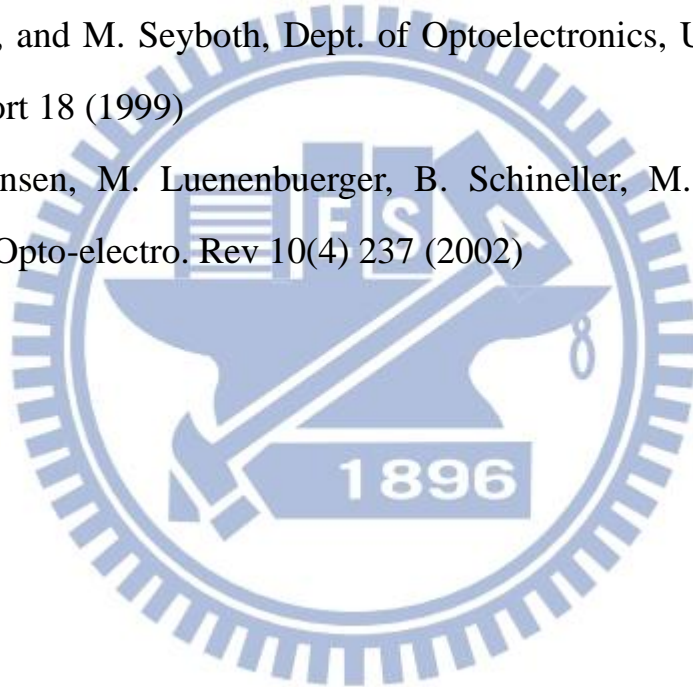




Fig. 2.1 MOCVD Aixtron 200/4 RF-s

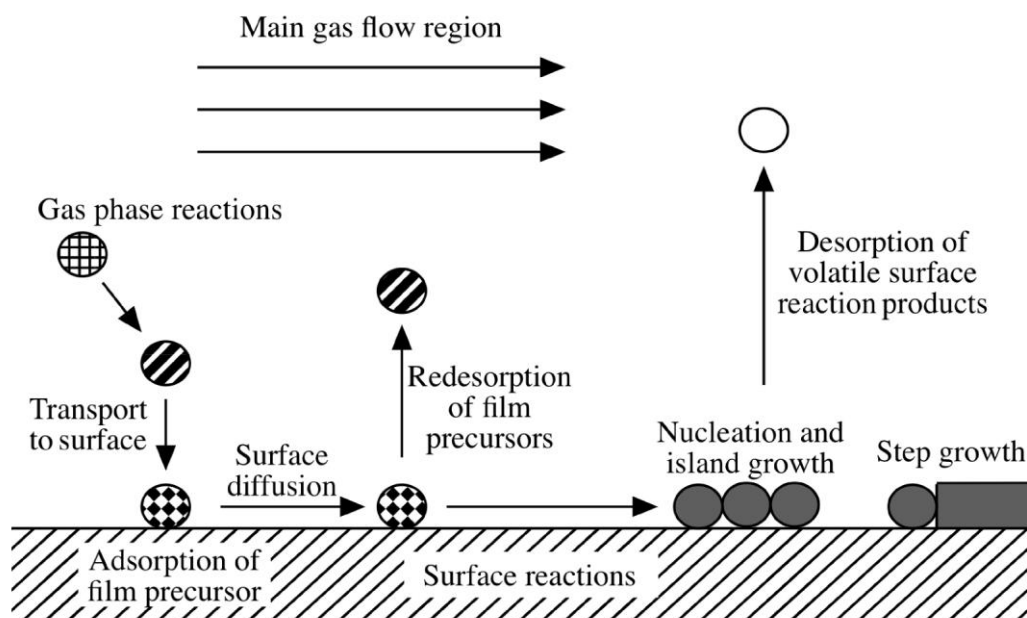


Fig. 2.2 Deposition process

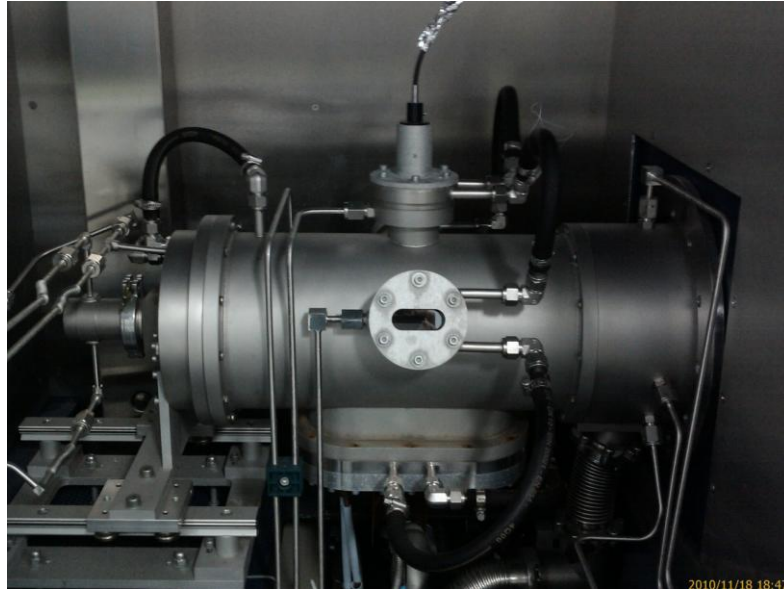


Fig. 2.3 Reactor of MOCVD

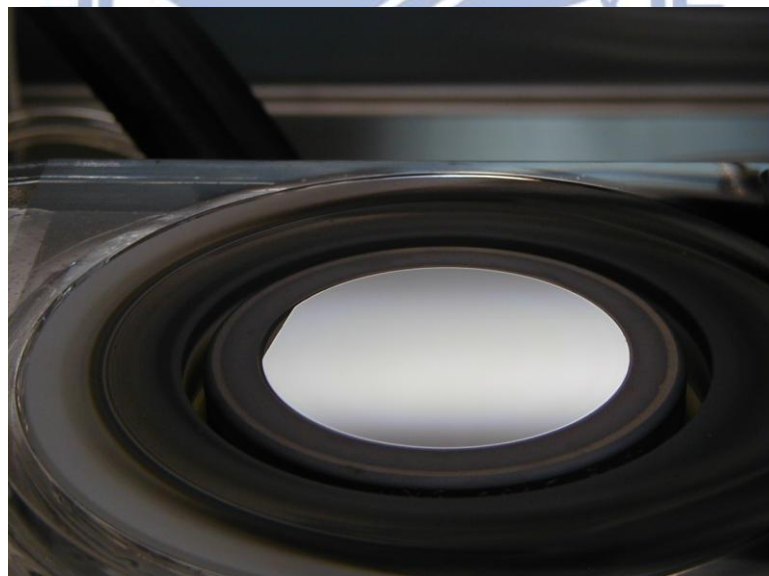


Fig. 2.4 Sapphire substrate and susceptor

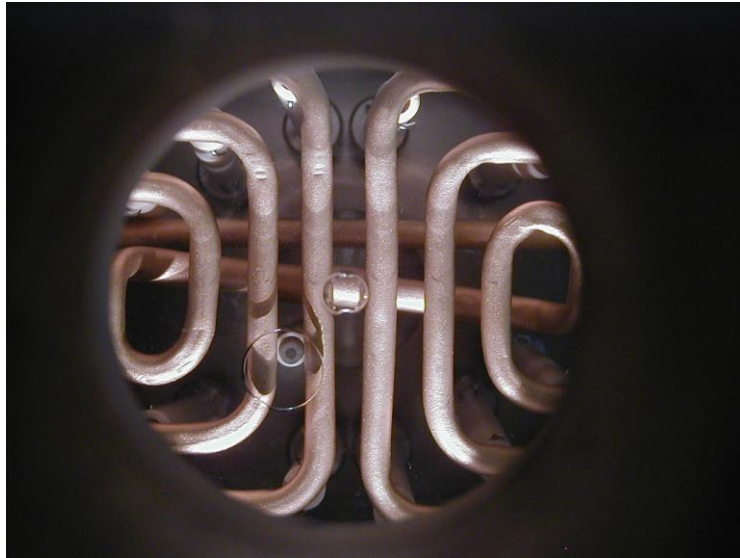


Fig. 2.5 RF-Coil and lightpipe

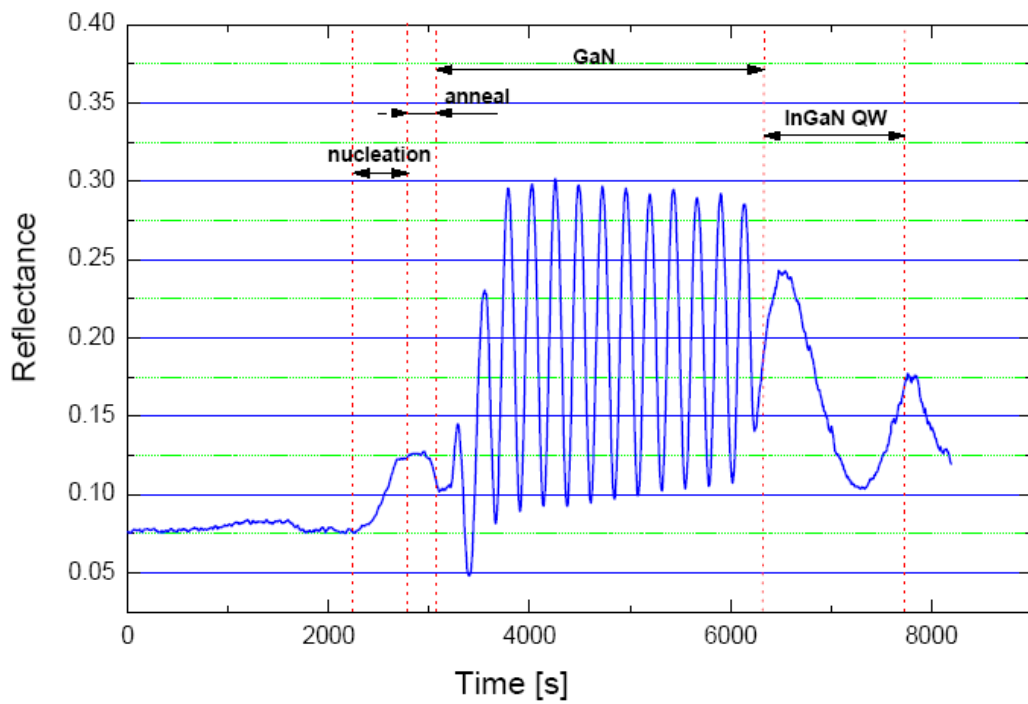


Fig. 2.6 In-situ reflectometry

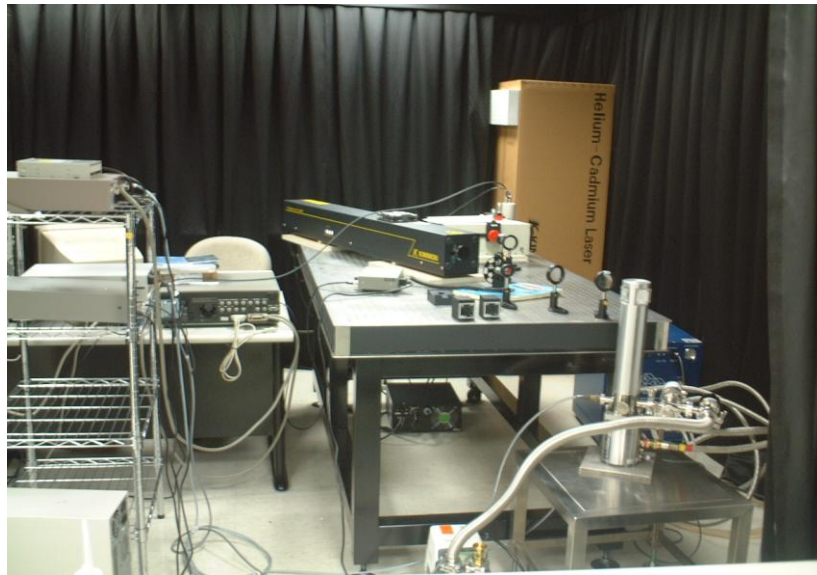


Fig. 2.7 PL measurement

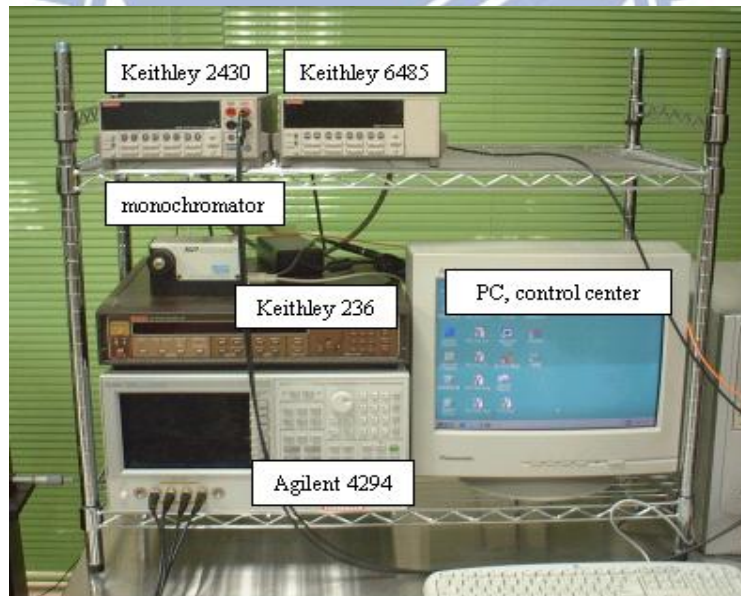
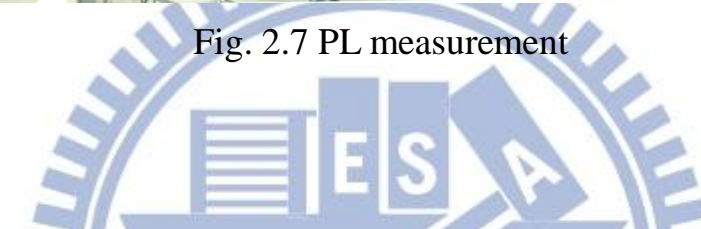


Fig. 2.8 EL measurement

# Chapter3 Spontaneous emission spectrum in light-emitting diodes

## 3.1 Introduction

This work presents a model for describing the shape of the spontaneous emission spectrum from a quantum-well structure [1]. A function is introduced to specify the probability distribution for the effective band gap. Based on this model, the coexisting carrier thermal broadening and effective band gap broadening in the spontaneous emission spectrum can be separated from each other. Applying this model to the spectra of AlGaInP light-emitting diodes (LEDs) reveals that the probability distribution functions are almost obtained by Gaussian function. Therefore, the emission spectra can be described by an analytical expression with fitted parameters. Possible reasons for this band gap broadening are discussed. The determination of the junction temperatures from the emission spectra and possible deviations of the results thus determined are also elaborated.

## 3.2 Optical joint density of state

To fully understand the spontaneous emission spectrum, the definition of optical joint density of state is described. The optical joint density of state is the density of allowable transition states that satisfy the k-selection rule, or equivalently, the density of states for electron-hole pairs. Thus, the definition of density of states in quantum well should be discussed. First, the density of allowed quantum states for a free electron as a function of energy in three-dimensional can be written as:

$$g(E) = \frac{4\pi(2m)^{3/2}}{h^3} \sqrt{E} \dots\dots\dots(3.1)$$

and the density of energy states in the conduction band and valence can be written as

$$g_c(E) = \frac{4\pi(2m_n^*)^{3/2}}{h^3} \sqrt{E - E_c} \dots\dots\dots(3.2)$$

$$g_v(E) = \frac{4\pi(2m_p^*)^{3/2}}{h^3} \sqrt{E_v - E} \dots\dots\dots(3.3)$$

To further consider the density of allowed states for electron-hole pair, an electron-hole recombination process is discussed. Figure 3.1 shows the dispersion relation of electrons in conduction band and holes in valence band. Thus, the photon energy can be written as the joint dispersion relation:

$$h\nu = (E_c - E_v) + \frac{\hbar^2 k_r^2}{2m_e^*} + \frac{\hbar^2 k_r^2}{2m_h^*} \dots\dots\dots(3.4)$$

where  $m_r$  is the reduced mass given by

$$\frac{1}{m_r} = \frac{1}{m_e^*} + \frac{1}{m_h^*} \dots\dots\dots(3.5)$$

To further differentiate Eq. 3.4, we have

$$dh\nu = \frac{\hbar^2 k_r}{m_r} dk_r = \frac{\hbar^2 k_r}{m_e^*} dk_r + \frac{\hbar^2 k_r}{m_h^*} dk_r = dE_e + dE_h$$

$$\Rightarrow dE_e = \frac{\hbar^2 k_r}{m_e^*} dk_r, \quad dE_h = \frac{\hbar^2 k_r}{m_h^*} dk_r$$

and hence we have

$$E_e = \frac{\hbar^2 k_r^2}{2m_e^*} = \frac{m_r}{m_e^*} \frac{\hbar^2 k_r^2}{2m_r} = \frac{m_r}{m_e^*} \frac{\hbar^2}{2m_r} (\frac{2m_r}{\hbar^2} \sqrt{h\nu - E_g})^2$$

$$\Rightarrow E_e = \frac{m_r}{m_e^*} (h\nu - E_g)$$

given by Eq. 3.2

$$g(E_e) = \frac{(2m_e^*)^{3/2}}{2\pi^2 \hbar^3} \sqrt{\frac{m_r}{m_e^*} (E_{h\nu} - E_g)} \dots\dots\dots (3.6)$$

using the joint dispersion relation

$$g(E_e)dE_e = \rho(h\nu)dh\nu \dots\dots\dots (3.7)$$

where

$$\frac{dE_e}{dh\nu} = \frac{m_r}{m_e^*}$$

the optical joint density of states in three-dimensional can be written as

$$\rho(h\nu) = \frac{(2m_e^*)^{3/2}}{2\pi^2 \hbar^3} \sqrt{\frac{m_r}{m_e^*} (h\nu - E_g)} \times \frac{m_r}{m_e^*} = \frac{(2m_r)^{3/2}}{2\pi^2 \hbar^3} \sqrt{h\nu - E_g}$$

$$\Rightarrow \rho(h\nu) = \frac{(2m_r)^{3/2}}{2\pi^2 \hbar^3} \sqrt{h\nu - E_g} \dots\dots\dots (3.8)$$

In two-dimensional system, the density of states is a step function, as shown in Fig. 3.2, and the optical joint density of states can be calculated

$$g(E) = \frac{m}{L\pi\hbar^2} u(E) \dots\dots\dots (3.9)$$

where  $u()$  is a step function and  $L$  is the well width

using  $E_e = \frac{m_r}{m_e^*} (h\nu - E_g)$  into Eq 3.9, we have

$$g(E_e) = \frac{m_e^*}{d\pi\hbar^2} u(h\nu - E_g) \dots\dots\dots (3.10)$$

Therefore, the optical joint density of states in two-dimensional can be written as



$$\rho(h\nu) = g(E_e) \frac{dE_e}{dh\nu} = \frac{m_e^*}{d\pi\hbar^2} u(h\nu - E_g) \times \frac{m_r}{m_e^*}$$

$$\Rightarrow \rho(h\nu) = \frac{m_r}{\pi\hbar^2 d} u(h\nu - E_g) \dots\dots\dots (3.11)$$

where  $m_r$  is the reduced mass of an electron-hole pair and  $u(h\nu - E_g)$  is a step-function.

### 3.3 Spontaneous emission

For a direct band gap semiconductor, the spontaneous emission rate can be written as [2]:

$$\gamma_{sp}(h\nu) = \frac{1}{\tau_r} \rho(h\nu) f_e(h\nu) \dots\dots\dots (3.12)$$

where  $\tau_r$  is the radiative lifetime of electron-hole recombination,  $\rho(h\nu)$  is the optical joint density of state,  $f_e(h\nu)$  is the occupancy probability of electron-hole pairs [3]. Since the occupancy probability of electrons  $f(E_2)$  in conduction band and the occupancy probability of holes  $[1 - f(E_1)]$  in valance band are both obtained by the Boltzmann distribution, as shown in Fig. 3.3, the occupancy probability of electron-hole pairs can be written as

$$f_e(h\nu) = f(E_2)[1 - f(E_1)] \dots\dots\dots (3.13)$$

$$\Rightarrow f_e(h\nu) = (e^{\frac{E_2 - E_{fn}}{KT}} + 1)^{-1} [1 - (e^{\frac{E_1 - E_{fp}}{KT}} + 1)^{-1}] = \frac{e^{\frac{E_1 - E_{fp}}{KT}}}{(e^{\frac{E_2 - E_{fn}}{KT}} + 1)(e^{\frac{E_1 - E_{fp}}{KT}} + 1)}$$

In low level injection, the occupancy probability of electron-hole pairs can be approximated to [4,5]:

$$f_e(h\nu) = f(E_2)[1 - f(E_1)] \approx e^{-\frac{E_2 - E_{fn}}{KT}} e^{-\frac{E_{fp} - E_1}{KT}}$$

$$= e^{\frac{E_{fn}-E_{fp}}{KT}} e^{-\frac{E_2-E_1}{KT}} \dots\dots\dots (3.14)$$

where  $E_{fn} - E_{fp}$  is the separation between the quasi-Fermi energies of the electron and the hole. Since  $E_2 - E_1 = h\nu$ , the Eq 3.14 can be rewritten as

$$f_e(h\nu) = e^{\frac{E_{fn}-E_{fp}}{KT}} e^{-\frac{h\nu}{KT}} \dots\dots\dots (3.15)$$

Therefore, we have the spontaneous emission rate in low level injection

$$\gamma_{sp}(h\nu) = \frac{1}{\tau_r} \rho(h\nu) e^{\frac{E_{fn}-E_{fp}}{KT}} e^{-\frac{h\nu}{KT}} \dots\dots\dots (3.16)$$

Using the optical joint density of states in three-dimensional (Eq. 3.8) and two-dimensional (Eq. 3.11), the spontaneous emission rate can be rewritten as

$$\gamma_{sp}(h\nu) = \frac{(2m_r)^{3/2} \sqrt{h\nu - E_g}}{2\tau_r \pi^2 \hbar^3} e^{\frac{E_{fn}-E_{fp}}{KT}} e^{-\frac{h\nu}{KT}} \quad (3-D) \dots\dots\dots (3.17)$$

$$\gamma_{sp}(h\nu) = \frac{m_r u (h\nu - E_g)}{\tau_r \pi \hbar^2 d} e^{\frac{E_{fn}-E_{fp}}{KT}} e^{-\frac{h\nu}{KT}} \quad (2-D) \dots\dots\dots (3.18)$$

Therefore, the spontaneous emission spectrum of LEDs can be fully ascribed by the multiplying of optical joint density of states and Boltzmann distribution, as shown in Fig. 3.4.

### 3.4 Absorption

For a direct band gap semiconductor, the absorption coefficient can be written as:

$$\begin{aligned} \alpha(h\nu) &= \frac{\lambda^2}{8\pi_r} \rho(h\nu) [f_a(h\nu) - f_e(h\nu)] \\ &= \frac{\lambda^2}{8\pi_r} \rho(h\nu) \{f_c(h\nu)[1 - f_v(h\nu)] - [1 - f_c(h\nu)]f_v(h\nu)\} \\ &= \frac{\lambda^2}{8\pi_r} \rho(h\nu) [f_c(h\nu) - f_v(h\nu)] \approx \frac{\lambda^2}{8\pi_r} \rho(h\nu) \dots\dots\dots (3.19) \end{aligned}$$

Since optical joint density of states is a factor of absorption coefficient, the optical joint density of states of LEDs can be obtained from absorption spectrum.

### 3.5 Emission spectrum

To verify the theoretical theory, an AlGaInP LED with varying temperature (120K to 400K) measured at 10mA was discussed. Figure 3.5 shows the wafer structure of the sample which has an *n*-type GaAs substrate, a 390-nm-thick *n*-type  $\text{Al}_{0.5}\text{In}_{0.5}\text{P}$  hole-blocking layer, 65 pairs of multiple quantum wells (MQWs), each of which comprises a 3.3 nm  $(\text{Al}_{0.3}\text{Ga}_{0.7})_{0.5}\text{In}_{0.5}\text{P}$  well / 2.9 nm  $(\text{Al}_{0.58}\text{Ga}_{0.42})_{0.5}\text{In}_{0.5}\text{P}$  barrier, a 517-nm-thick *p*-type  $\text{Al}_{0.5}\text{In}_{0.5}\text{P}$  electron-blocking layer, and a 9.38- $\mu\text{m}$ -thick *p*-type GaP current spreading layer. The sample made from the wafer had an area of  $225 \times 225 \mu\text{m}^2$  and a height of 180  $\mu\text{m}$ . The sample was mounted onto a heat sink using a metal solder. The heat sink was a Bergquist thermal clad substrate with an area of  $3 \times 3 \text{ cm}^2$  and a height of 0.2 cm. The device spectra were obtained by placing the device onto the sample holder of a cryostat, electrically driving the device, collecting the top emission using a microscope, and then analyzing the wavelength-dependent energy spectral density functions  $P(\lambda)$  using a monochromator and a silicon photodetector. The overall system wavelength-dependent response comprised of the responsivity of the silicon photodetector and the reflectivity of the grating was taken into account. Figure 3.6 presents the spectra of the sample that was operated at 10 mA, at temperatures from 120 to 400 K in steps of 20 K. As the ambient temperature increased, the peaks were redshifted and the intensities attenuated. As each photon represents a transition event in the active layer, the photon density spectrum is more useful than the power spectrum in obtaining information about spontaneous emission and the related phenomena.  $P(\lambda)$  was

then transformed to the corresponding frequency-dependent energy spectra  $P(h\nu)$ , according to  $P(h\nu)=(\lambda^2/hC_0)P(\lambda)$ , where  $C_0$  is the speed of light in a vacuum and  $h$  is Planck's constant [6].

The relative photon density spectra  $r(h\nu)$  were then obtained using  $r(h\nu)=P(h\nu)/h\nu$ , and the results are plotted as solid curves on a semi-log scale in Figs. 3.7. As indicated by the solid curves in Figs. 4, although the ambient temperature covers a rather wide range (from 120 to 400 K), the slopes of the low-energy tails of the measured spectra do not change appreciably with the temperature. This fact is consistent with Eq. 3.16, which states that the low-energy tails of these spectra depend strongly on the broadening of the band gap but weakly on the junction temperature. In contrast, the high-energy tails of these spectra are accurately described by straight lines whose gradients depend strongly on the temperature. Thus, the junction temperatures can be obtained from the high-energy tails of the spectra. Figure 3.8 shows the EL spectrum of the sample at 300K and the dashed line revealed that the junction temperature is around 307.65K, which is very close to the ambient temperature. Figure 3.9 plots the junction temperatures obtained from the gradients, which are very close to the ambient temperatures. This result agrees with the theoretical theory and this method can be applied to measure the junction temperatures from emission spectra. Furthermore, it was also observed that the optical joint densities of states of the sample shift toward higher energy with decreased of temperature, as shown in Fig. 3.10. This result indicated that the shift of the emission spectrum was obtained by the Varshni equation.

### **3.6 Photo current**

Furthermore, the photo-current measurement was used to investigate the absorption spectra of LEDs. Three AlGaInP LEDs with different wavelength

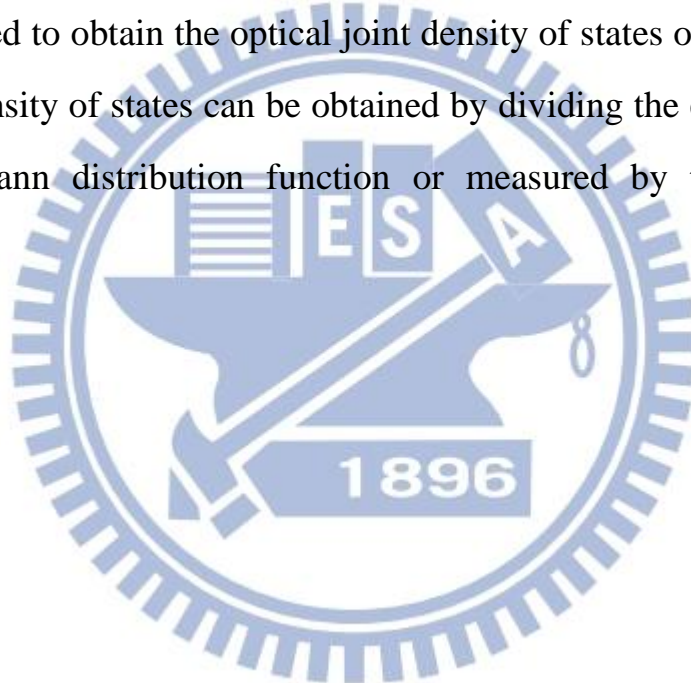
(red, yellow and yellow-green) were used. The wafer structure of the samples which has an *n*-type GaAs substrate, a 600-nm-thick *n*-type Al<sub>0.5</sub>In<sub>0.5</sub>P hole-blocking layer, a 600-nm-thick *p*-type Al<sub>0.5</sub>In<sub>0.5</sub>P electron-blocking layer, and a 11μm-thick *p*-type GaP current spreading layer. The emission wavelength and distributed Bragg reflector (DBR) for each sample was to adjust the structure of MQWs, as shown in Fig. 3.11, Fig. 3.12 and Fig. 3.13.

Figure 3.14 to figure 3.16 shows the photo-current spectrum under varying reverse bias (0V, -5V, -10V) and EL spectrum measured at 20mA. The photo current spectrum shows independent with reverse bias. It is indicated that the MQWs of the samples are in the depletion regions, thus, when laser excited the electron-hole pairs in MQWs, both electrons and holes will sweep out toward *n*-type layer and *p*-type layer, respectively. At low energy tail, the photo current spectrum shows similar feature with the EL spectrum. That is due to the optical joint density of state is a factor of the absorption spectrum and emission spectrum (Eq. 3.12 and Eq. 3.19). On the other hand, the increased of the photo current spectrum with interference can be attributed the existence of the DBR under *n*-type layer. Therefore, the penetrated laser form MQWs can be reflexed to MQWs and reabsorbed. The intensity of the reflection and the width can be simulated from the index of the sample structures, as shown in Fig. 3.17. Moreover, both of the intensity of the photo current spectra decreased when  $E_g > 2.3\text{eV}$ . The reason of the decrease of the intensity can be explained by the absorption of the GaP. As we assumed that the absorption spectrum of the MQWs is a step function, the absorption spectrum of GaP can be obtained from the dividing the step function and photo current spectrum, as shown in Fig. 3.18, Fig. 3.19 and Fig. 3.20. Despite the influence of the DBR and absorption of GaP, the photo current spectrum shows the same feature with the optical joint density

of states obtained from the EL spectrum. This result indicated that the

### **3.7 Conclusion**

This work presents a model for describing the spectra of quantum wells. The carrier temperature can be determined from the high-energy tail of the spectrum and the probability distribution function can be deduced by further numerical processing. This model was applied to an AlGaInP LED, and the measured carrier temperatures were found to be very close to the temperatures. This finding is important evidence of the validity of the proposed model. Two methods are used to obtain the optical joint density of states of the samples. The optical joint density of states can be obtained by dividing the emission spectrum by the Boltzmann distribution function or measured by the photo current measurement.



## Reference

- [1] N. C. Chen, C. M. Lin, C. Shen, W. C. Lien, and T. Y. Lin, *Opt. Express* **16**, 20759 (2008).
- [2] B. E. A. Saleh, and M. C. Teich, *Fundamentals of Photonics*, (John Wiley & Sons, 1991). P.593
- [3] H. D. Summers, J. D. Thomson, P. M. Snowton, P. Blood, and M. Hopkinson, *Semicon. Sci. Tech.*, vol.16, p.140, (2001).
- [4] P. Blood, E. D. Fletcher, P. J. Hulyer, and P. M. Snowton, *Appl. Phys. Lett.*, vol.48, p.1111, (1986).
- [5] P. Blood, A. I. Kucharska, J. P. Jacobs, and K. Griffiths, *J. Appl. Phys.*, vol.70, p.1144, (1991).
- [6] N. C. Chen, Y. N. Wang, C. Y. Tseng, and Y. K. Yang, *Appl. Phys. Lett.* **89**, 101114 (2006).
- [7] N. C. Chen, W. C. Lien, Y. K. Yang, C. Shen, Y. S. Wang, and J. F. Chen, *J. Appl. Phys.* 106, 074514 (2009).

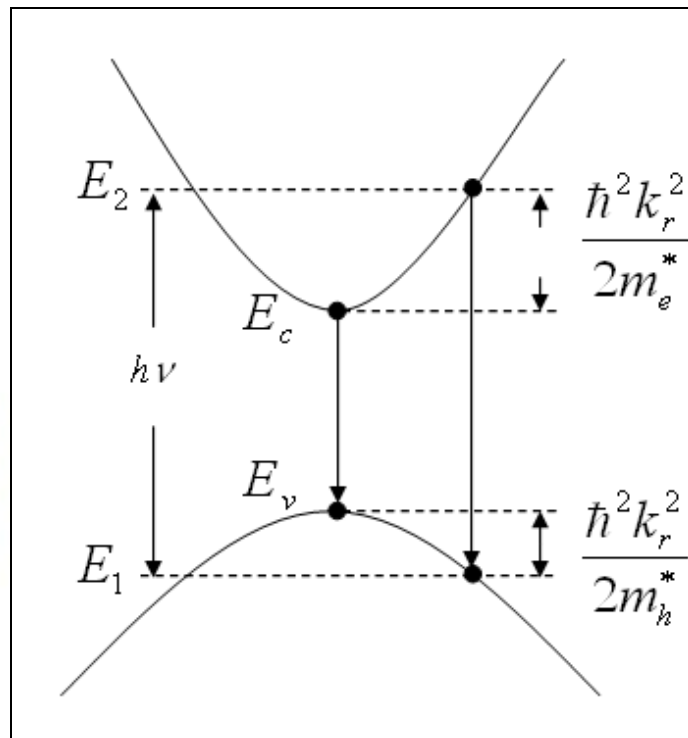


Fig. 3.1 Dispersion relation of electron-hole recombination and phonon emission



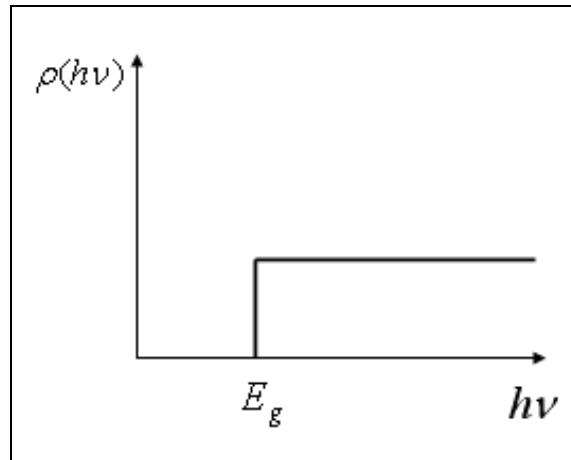


Fig. 3.2 Density of states in two-dimensional

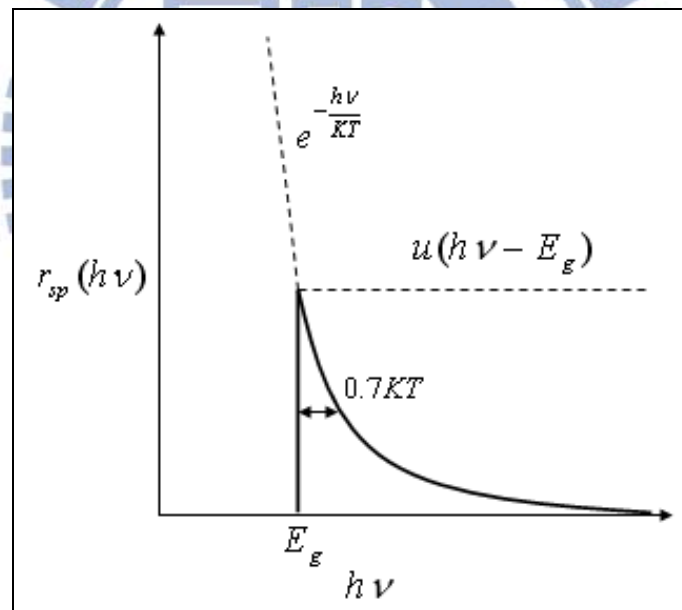


Fig. 3.3 Theoretical emission spectrum in two-dimensional quantum structure

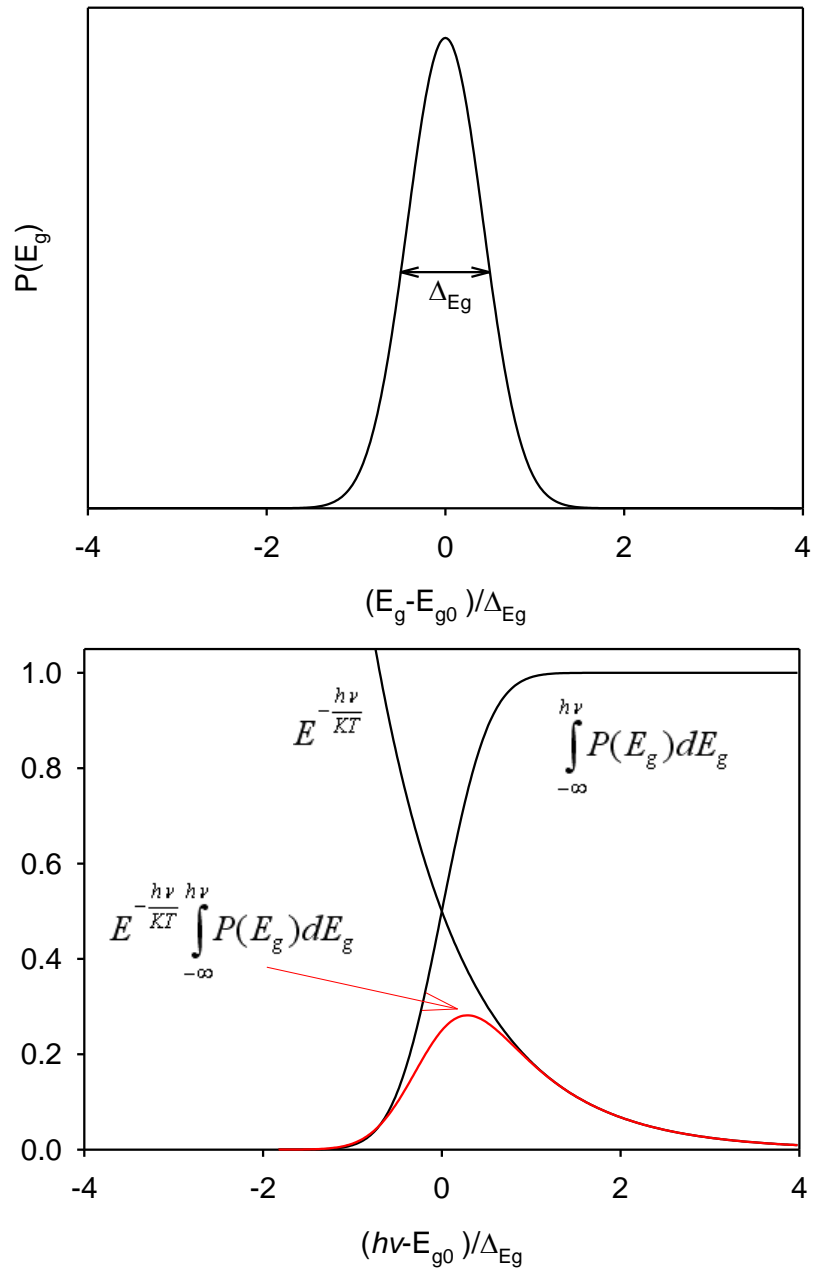


Fig. 3.4 Theoretical emission spectrum of an LED

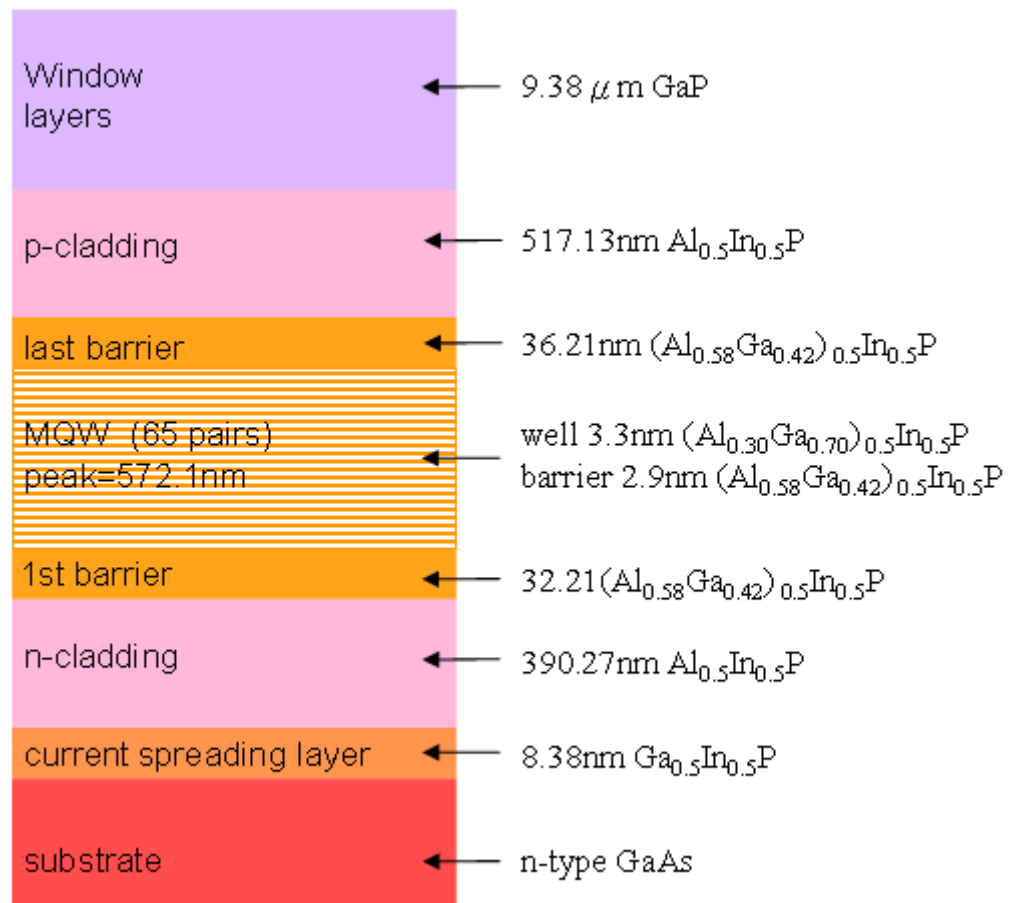


Fig. 3.5 Sample structure of an AlGaInP LED

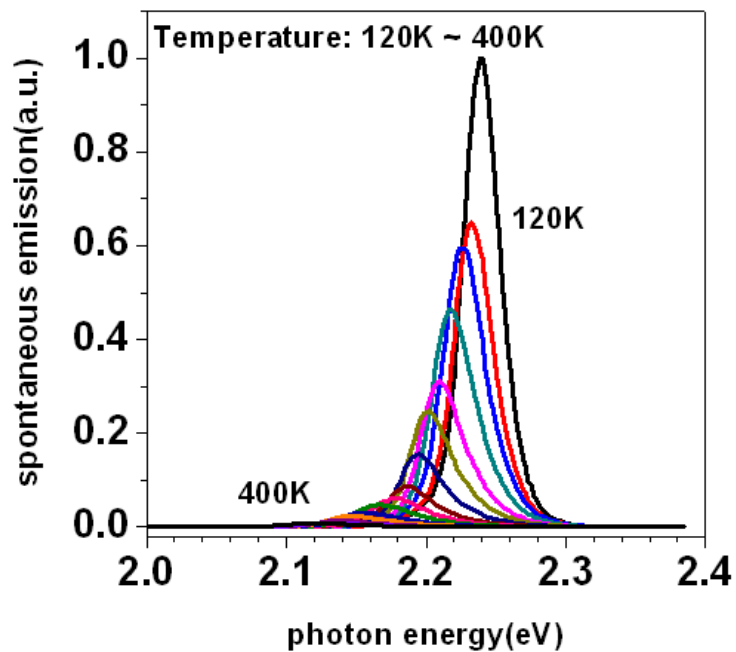


Fig. 3.6 Power spectra of the LED measured at 10 mA, and the temperature ranges from 400 to 120 K

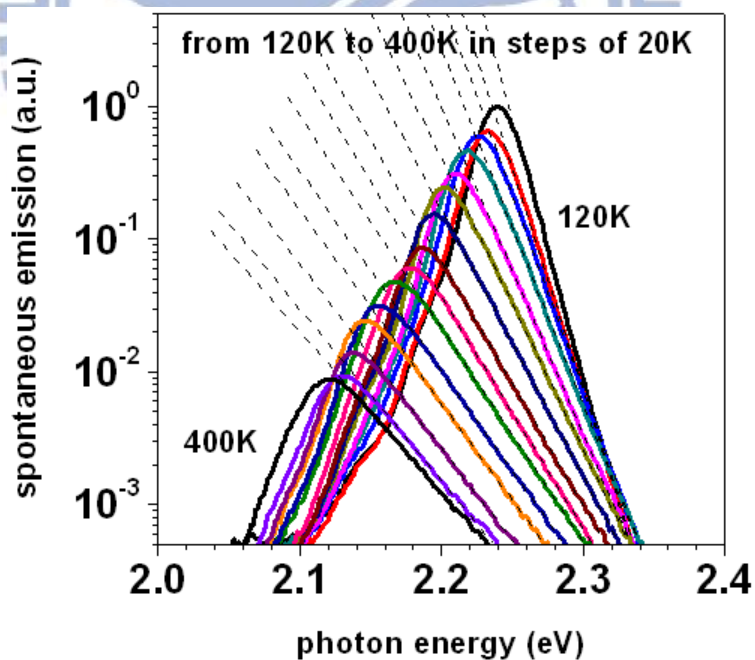


Fig. 3.7 Photon density spectra measured at 10 mA on a semi-log scale and the temperature ranges from 400K to 120K

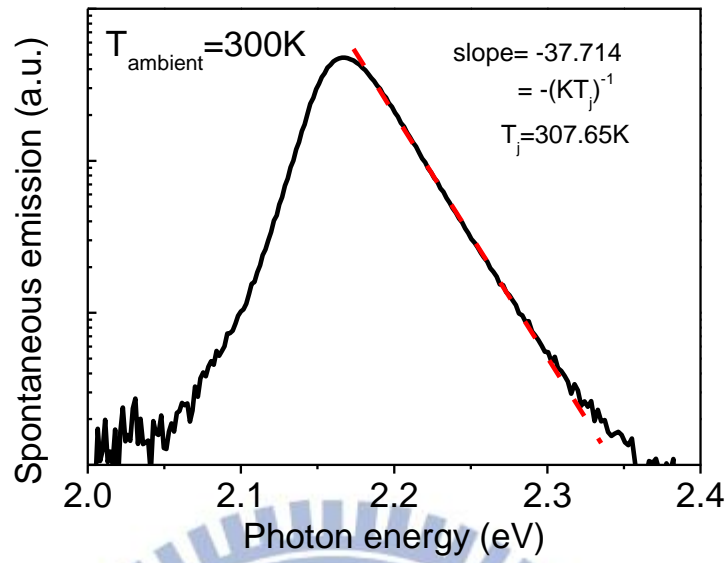


Fig. 3.8 Junction temperature obtained from gradients of high-energy tails in an EL spectrum at 300K

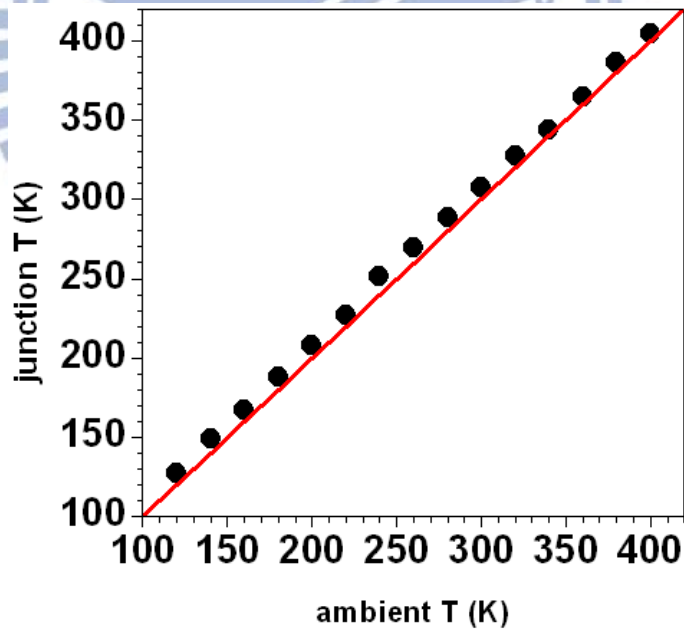


Fig. 3.9 Dependences of junction temperatures on ambient temperatures obtained from gradients of high-energy tails

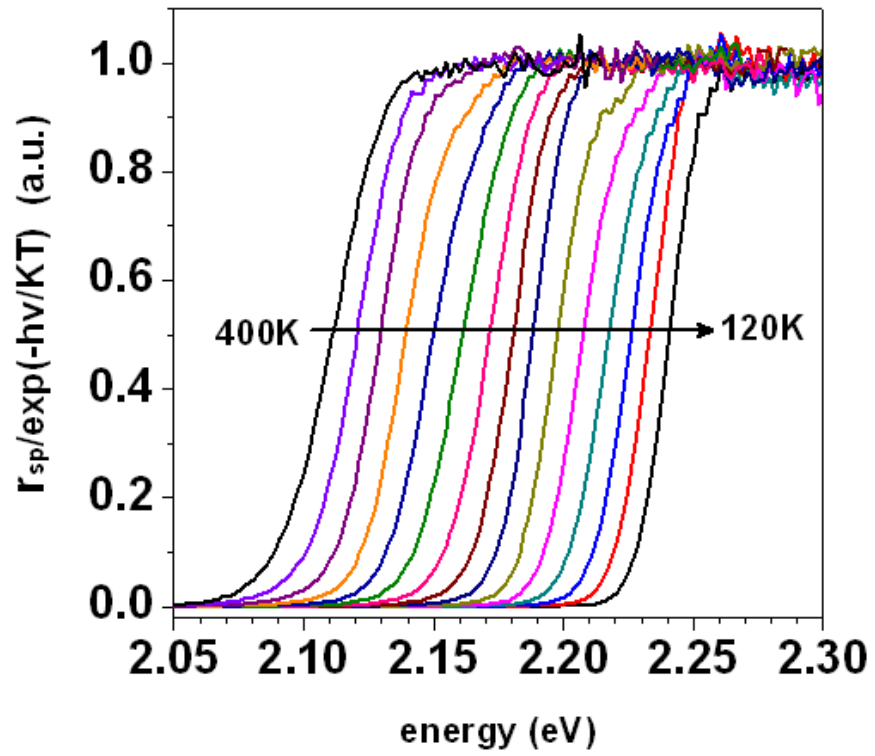


Fig. 3.10 Temperature dependence of optical joint densities of states from 400K to 120K



Fig. 3.11 Sample structure of the red LED



Fig. 3.12 Sample structure of the yellow LED



Fig. 3.13 Sample structure of the yellow-green LED

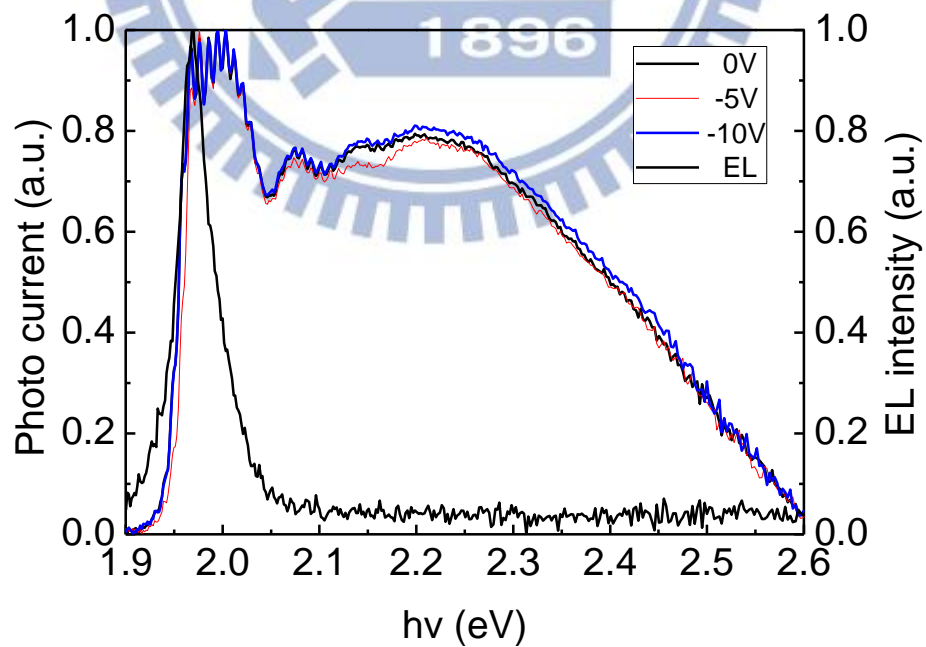


Fig. 3.14 Photo current spectrum and EL spectrum of the red LED



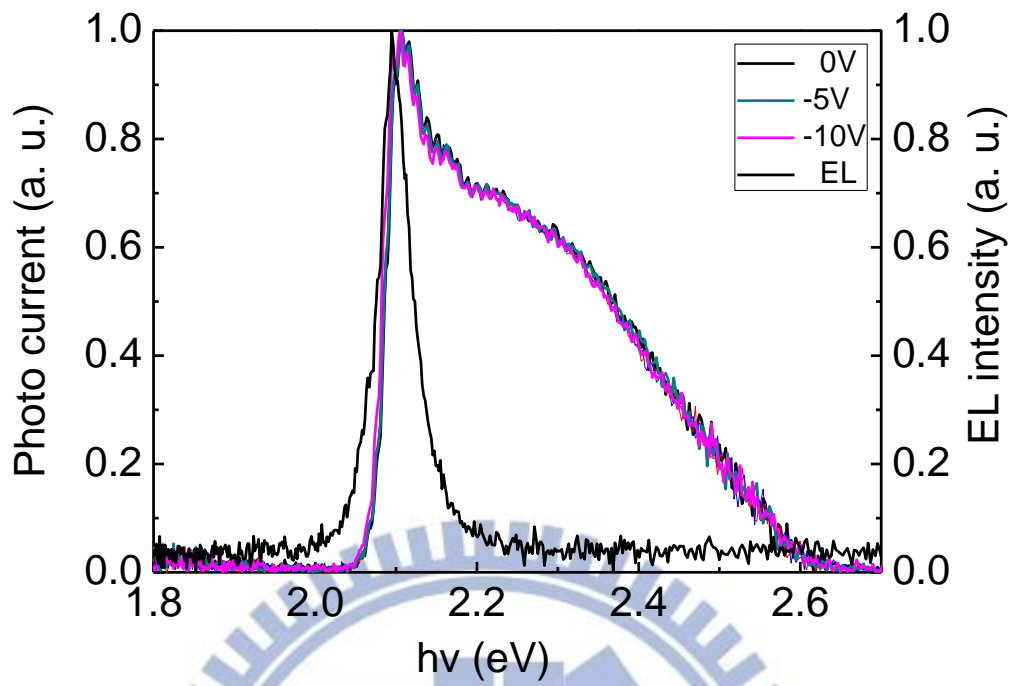


Fig. 3.15 Photo current spectrum and EL spectrum of the yellow LED

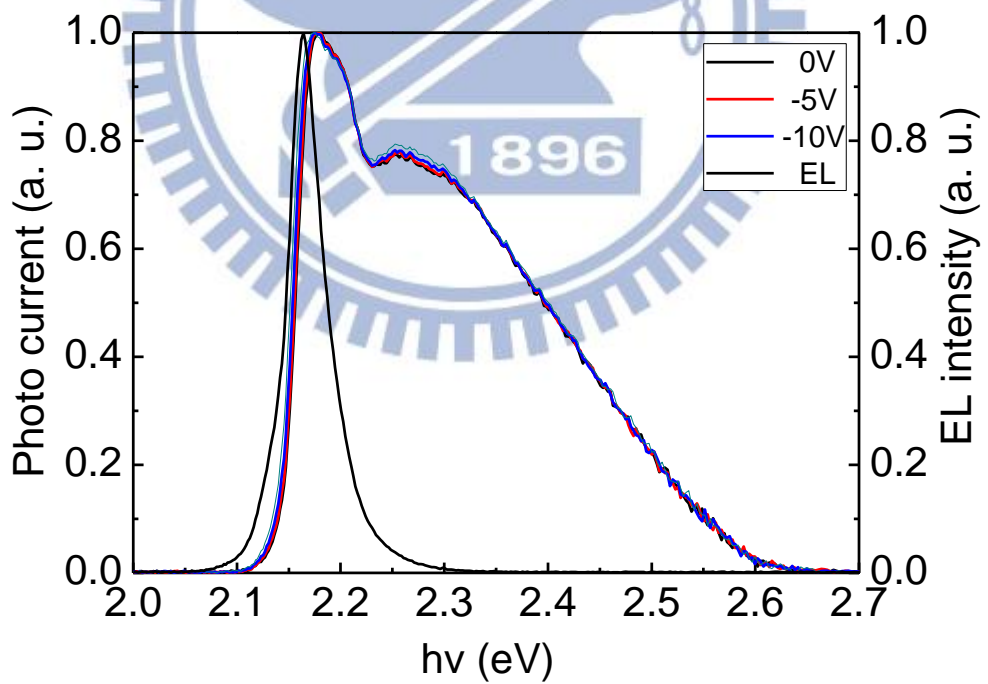


Fig. 3.16 Photo current spectrum and EL spectrum of the yellow-green LED

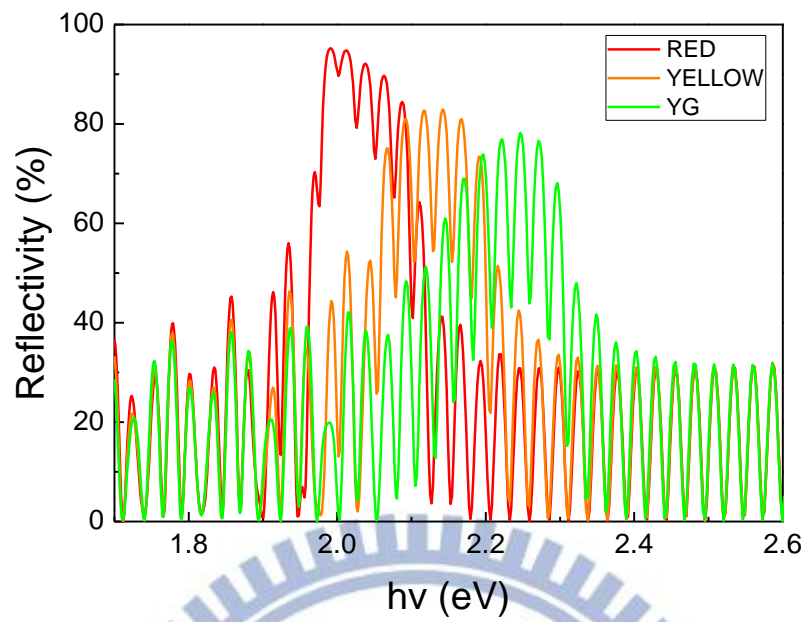


Fig. 3.17 Simulation of the DBR

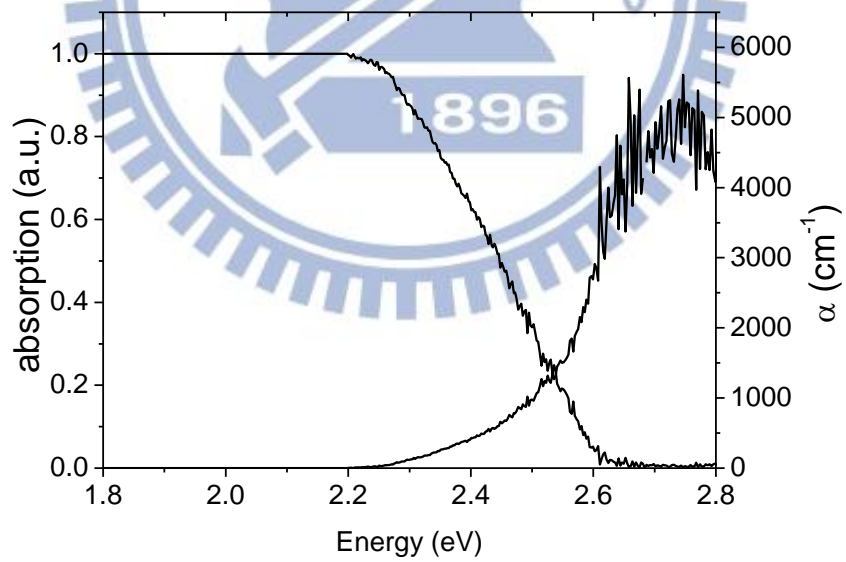


Fig. 3.18 Absorption spectrum of GaP in red LED

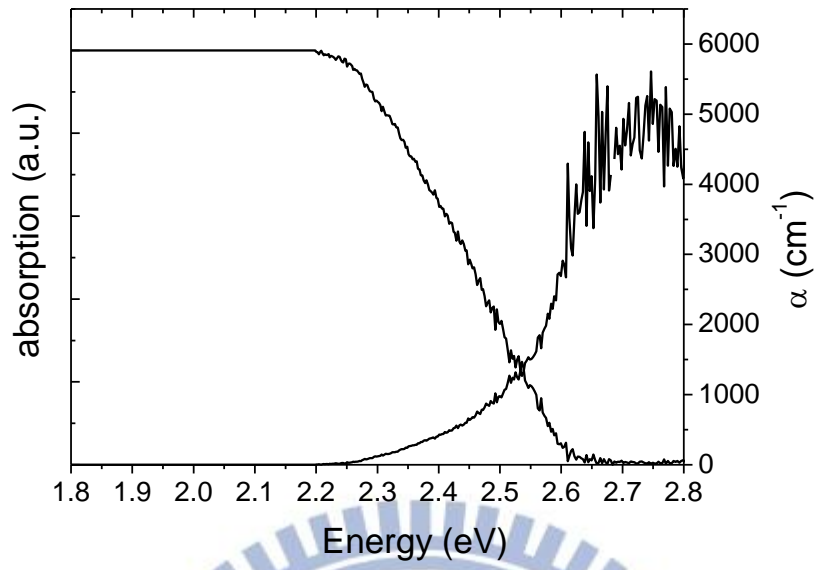


Fig. 3.19 Absorption spectrum of GaP in yellow LED

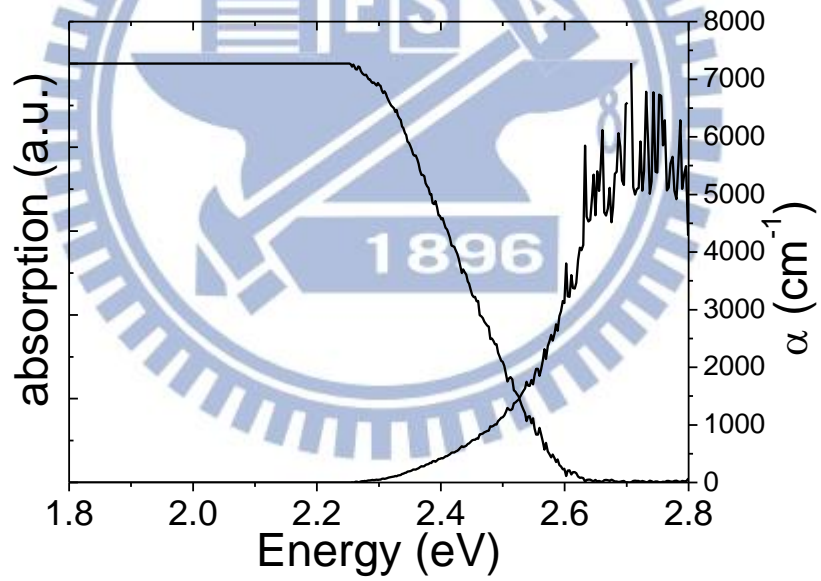


Fig. 3.20 Absorption spectrum of GaP in yellow-green LED

# Chapter 4 Optical joint density of states in InGaN/GaN multiple-quantum-well light-emitting diodes

## 4.1. Introduction

Because of the wide range of energy gaps in group-III nitride-based materials, InGaN/GaN-based multiple quantum wells (MQWs) have been used in a broad range of emission wavelengths, such as blue, green and yellow light-emitting diodes (LEDs) [1]. Although the number of applications of these devices has increased in the past decade, their special features still attract considerable attention. For example, despite their high dislocation density (typically in the range  $10^8$ - $10^{10}$  cm<sup>-2</sup>), their luminescence efficiency is peculiarly higher than expected [2]. Also, a large Stokes-like shift occurs between the emission peak and the absorption edge, and this shift correlates with indium content [3]. Many studies have confirmed that indium atoms are important to these phenomena [4]. Since localized states that result from self-organized In-rich regions are regarded as quantum dots [5] or quantum disks [6], electron-hole pairs are likely associated with the localized states rather than being transferred to threading dislocations that act as nonradiative centers [7,8]. Additionally, the quantum-confined Stark effect (QCSE) that is caused by the piezoelectric field has been found to have a large influence on the emission [9]. Because of a large lattice mismatch between GaN and InGaN, a strong strain-induced piezoelectric field tends to shift the quantum-confined level to lower energy [10]. However, the reasons for the blueshift of the emission peak with increasing current and the anomalous broadening of the full width at half

maximum (FWHM) are still under debate. Since both the photoluminescence (PL) and the electroluminescence (EL) peaks are at the absorption tail, some researchers have suggested that the blueshift results mainly from the band filling effect of the localized states that correspond to the formed In-rich regions [11]. Others have argued that the blueshift is related to the screening of the piezoelectric field by carriers [12]. Chichibu *et al.* [13] argued that the blueshift is a combined effect of band filling of localized states and screening of the QCSE. Notably, most related studies have used PL excitation (PLE) to obtain the absorption spectrum. However, the electrically injected carriers and the corresponding emission prevent the absorption spectrum from being obtained under large forward bias. Therefore, the band filling effect of localized states and the piezoelectric effect with a forward current are difficult to determine, and definitive explanations of the blueshift and anomalous increase in the FWHM are still unavailable. On the other hand, the reason of S-shift (redshift-blueshift-redshift) in InGaN/GaN LEDs with varying temperatures is also need more evidence. The explanation of the S-shift has been study for many decades [14,15]. The recombination mechanism of the InGaN LEDs in different temperature ranges can be explained as follows: (i) For  $T < 50\text{K}$ , since radiative lifetime at the lowest temperature is fast and dominant the recombination process, carriers should recombination radiatively in quantum states before relax down into localized states. Thus, when temperature further increased, carriers relax into localized states and induce emission peak decreased. (ii) For  $50\text{K} < T < 150\text{K}$ , since carriers are recombined in localized states and the occupation of probability in each state by an electron-hole pair should obtained by Boltzmann distribution function. Thus, when temperature increased, the occupation of probability at higher states should increase and induce emission

peak increased. (iii) For  $T > 150\text{K}$ , since temperature induced band gap shrinkage dominate the emission peak, the emission peak decrease with increasing temperature [16-19]. However, the research of these current and temperature induced peak shift has left many questions unanswered, more work must be done.

This work presents a method for determining the optical joint density of states of nitride-based LEDs using an EL spectrum instead of a PLE. The proposed method of extracting the optical joint density of states is to divide the EL spectrum by the Boltzmann distribution function, to determine the effect of current on the blueshift and the increase in the FWHM [20]. Similar methods, in the form of relations among spontaneous emission, absorption and gain spectra, have been extensively used in studying the details of InGaAsP, AlGaAs, InGaAs and GaAs laser diodes in various aspects [21-28]. Besides, the authors have successfully explained the carrier dynamics, the redshift of the edge emission, the junction temperature and the broadening of the emission spectrum of AlGaInP LEDs by using this method [29,30]. All of these successful precedents justify the method used in this paper. The samples investigated herein are commercial products that were grown on *c*-plane sapphire substrates by metal organic vapor deposition. Three InGaN/GaN-based light-emitting diodes with different emission wavelengths (violet, blue and green) were adopted. To obtain their spectra, the devices were placed on a heat sink and operated in pulsed mode with a frequency of 1000Hz and a duty cycle of 10% to diminish any possible effect of Joule heating. Thus, the junction temperatures of the measured devices were determined only by the environment, and the corresponding Boltzmann distribution functions are obtained from the ambient temperatures.

#### **4.2 Current dependent of emission spectra**

Figure 4.1 presents the normalized EL spectra of the samples under various currents at 300K. The peaks shifted to higher energy as the current increased, and the degree of shift was correlated with the indium content. From 10mA to 80mA, the blueshifts for the violet, blue and green LEDs were 0meV, 19meV and 37meV, respectively. The FWHM for the violet, blue and green LEDs were 89meV, 140meV and 160meV, respectively, indicating that the FWHM was strongly correlated with the indium content but weakly correlated with current density. Similar results concerning the blueshift and the increase in the FWHM have been observed in many studies, including those mentioned above.

To determine how localized states and piezoelectric field affect the spectrum under various currents, the optical joint densities of states of these devices are determined under various currents from the measured spectra. The spontaneous emission spectrum of an LED is [20,29,30]

$$r(h\nu) \propto \rho(h\nu) e^{-h\nu/KT} \dots\dots\dots (4.1)$$

where  $\rho(h\nu)$  is the optical joint density of states, which is the density of allowable transition states that satisfy the k-selection rule, or equivalently, the density of states for electron-hole pairs, and  $e^{-h\nu/KT}$  is the Boltzmann distribution function, which describes the probability of occupation of each state by an electron-hole pair. Generally, the optical joint density of states has the same mathematical form as the electron (hole) density of states, except in that the effective mass of electron (hole) should be replaced by the reduced mass of electron-hole pairs [20]. Thus, when the optical joint density of states is obtained, the characteristics of the electron and hole densities of states are also obtained, and the optical joint density of states can easily be deduced from the spontaneous emission spectrum by merely dividing the emission spectrum by

the Boltzmann distribution function. Notably, such a method is preferable to PLE, since PLE obtains the optical joint density of states via an absorption spectrum, which cannot be obtained at large forward bias. Figure 4.2 shows the relative optical joint densities of states obtained from the EL spectra. All of these curves show two distinct regions – a low-energy tail and a high-energy region, where the density of states increases steeply with increasing energy. Since the low-energy tails of all of these samples are independent of current, the tails are attributed to the formation of localized states. In contrast, the steep increase of the density of states in the high-energy region indicates that these states correspond to the unlocalized states of the two-dimensional quantum structure [25], and its characteristics depend strongly on the samples. The violet LED yields the largest slope among these samples, and its density is independent of current; for blue and green LEDs, the curves of densities strongly depend on current, and their slopes increase with the current, as revealed by the linear fitted dashed lines. These dependences of density on both the sample and the current can be explained by the effect of the piezoelectric field and the screening of this field by carriers. The large amount of indium in the wells in blue and green LEDs makes the piezoelectric field therein wells significant. This field tilts the potential of the quantum well, as shown in Fig. 4.3(a), and electrons and holes in the same well should be spatially separated on opposite sides of the well. Thus, both the electron-hole wave-function overlap and the effective band gap of the well are decreased [32]. As the operating current was increased, the number of carriers in the wells increased, and the piezoelectric field drove the carriers to screen the field itself. Therefore, both the wave-function overlap and the band gap energy increased, as shown in Fig. 4.3(b). S. F. Chichibu *et al.* [33] and C. K. Choi *et al.* [34] reported similar results. Their results reveal that the slope of the



absorption edge is determined by the piezoelectric field and can be screened by increasing the Si-doping concentrations in the barriers.

Since the slopes of the densities of states in the high-energy region depend on current, the blueshift of the spectra may be attributed to this phenomenon. To examine quantitatively this possibility, the densities of states of blue and green LEDs at various currents were approximated by the linear fitted dashed lines plotted in Fig. 4.2; then, the theoretical emission spectra were obtained by multiplying these fitted curves by the Boltzmann distribution function, as shown in Fig. 4.4. Figure 4.5 presents the blueshifts that were obtained from these theoretical spectra and from the experiment. The agreement between these two sets of data clearly demonstrates the proposed cause of the blueshift, and provides evidence of the screening of the piezoelectric field by carriers. However, the FWHMs of the simulated spectra are lower than those obtained experimentally, as shown in Fig. 4.6. This discrepancy results from the linear approximations of the densities of states that wholly ignored the existence of localized states in the low-energy tails [5]. Although these localized states are known to be independent of current, as mentioned above, they still contribute appreciably to the emission spectra. In fact, the low-energy sides of the EL spectra are determined by the energy distribution of these localized states. Thus, as the indium content is increased, the low-energy tail should be further extended, and the corresponding FWHM of the emission spectrum should increase.

In summary, the optical joint densities of states of three InGaN/GaN-based LEDs with different emission wavelengths were determined at various currents. The optical joint density of states has two distinct regions, a high-energy region, which corresponds to the unlocalized quantum well states and a low-energy tail,

which corresponds to the localized states. As the operating current is increased, the slope of the density of states at high-energy region increases with the screening of the piezoelectric field. This fact causes the peak of the EL spectrum to blue-shift with increasing current. The low-energy tail of the optical joint density of states determines the extension of the low-energy side of the EL spectrum, and this fact explains the anomalous increase in the FWHM of the emission of nitride-based LEDs. Furthermore, both of these effects are enhanced by increasing indium content, which relationship is responsible for the increase in blueshift and FWHM with the emission wavelength of the device.

### **4.3 Temperature dependent of emission spectra**

Figure 4.7 presents the normalized PL spectrum of the sample with varying temperatures from 20K to 340K. Figure 4.8 shows the S-shaped variation with temperature. The peak energy shifts from 2.76eV to 2.75eV when temperature increased from 20K to 80K, and shifts to 2.76eV when temperature increased to 200K. The peak energy shifts to 2.744eV when temperature further increased to 340K.

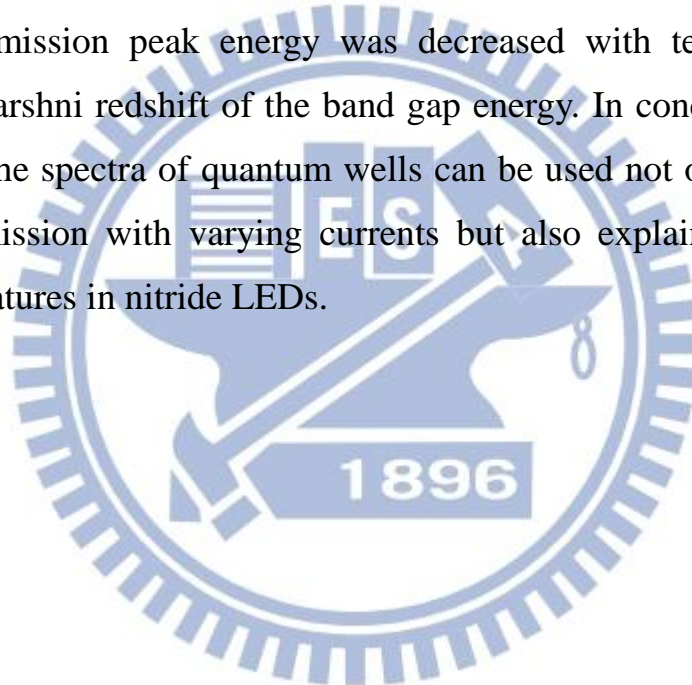
To further understand the S-shaped shift of the emission peak under various temperatures, the optical joint densities of states of the sample are determined under various temperatures from the measured spectra. Figure 4.9 shows the relative optical joint densities of states obtained from the PL spectra with varying temperature. Similar to the optical joint densities of states obtained from the EL spectra, these curves also show two distinct regions – a low-energy tail and a high-energy region. According to the previous result, the low-energy tails are attributed to the formation of localized states and the steep increase of the density of states in the high-energy regions are attributed to the unlocalized states of the two-dimensional quantum structure. Here, the unlocalized states of the two-dimensional quantum structure can be linear fitted as shown in Fig. 4.10.

To further consider the effects of the emission peak by these two regions, the theoretical emission spectra of these two regions were obtained. The theoretical emission spectra of the two-dimensional quantum structure were obtained by using the fitted dish lines multiplying the Boltzmann distribution function, as shown in Fig. 4.11. On the other hand, the optical joint densities of states of localized states can be obtained by divided from the origin optical joint densities of states and linear fitted lines as shown in Fig. 4.12. The theoretical emission spectra of localized states were obtained by multiplying the Boltzmann distribution function, as shown in Fig. 4.13.

To further compare these two theoretical emission spectra with varying temperatures, the theoretical emission peak of the localized states shows S-shaped shift, however, the theoretical emission peak of the two-dimensional quantum structure shows only redshifts, as shown in Fig. 4.14. This result indicates that the S-shaped shift is mainly attributed to the localized states and can be explained by the delocalization of excitons out of potential minima. The emission spectrum corresponded to the quantum structure is only affected by the Varshni redshift of the band gap energy. Furthermore, when the temperature increased to 200K, the emission peak positions are contributed by both localized states and quantum structure and redshifts with temperature. The value of the shifts is smaller than the theoretical emission peak of the localized states, which indicated that the emission spectrum corresponded to the unlocalized two-dimensional quantum structures become to dominate the PL emission peak.

In summary, the optical joint densities of states of a nitride-based LED were determined with varying temperatures. The optical joint density of states can be divided into two regions, a low-energy tail is attributed to the localized states and a high-energy tail is attributed to the unlocalized states of the two-dimensional quantum well. The theoretical emission spectra of the two regions were obtained by multiplying the Boltzmann distribution function separately. Since the Boltzmann distribution can not be used in the lowest range

of temperatures due to the thermal equilibrium could not be obtained. Thus, the optical joint densities of states in the range of temperature were not discussed. As temperature in the range of 80K to 200K, the emission spectrum corresponded to localized states dominates the PL emission peak, as shown in Fig. 4.15(a). The emission peak energy increased with temperature, which results the PL emission peak blue shift. This phenomenon can be explained by the delocalization of excitons out of potential minima. As temperature higher than 200K, the emission spectrum corresponded to the two-dimensional quantum well becomes to dominate the PL emission peak, as shown in Fig. 4.15(b). The emission peak energy was decreased with temperature, which results in the Varshni redshift of the band gap energy. In conclusion, the model for describing the spectra of quantum wells can be used not only to explain the blueshift of emission with varying currents but also explain the S-shift with varying temperatures in nitride LEDs.

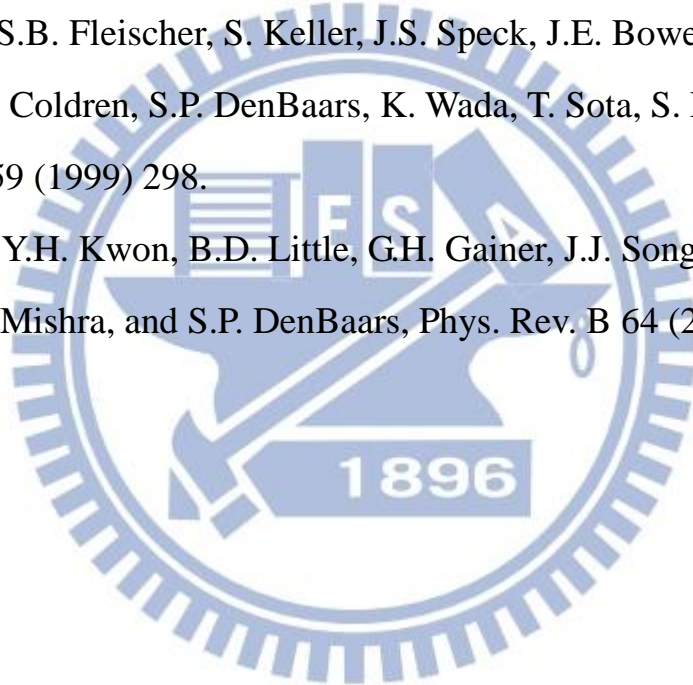


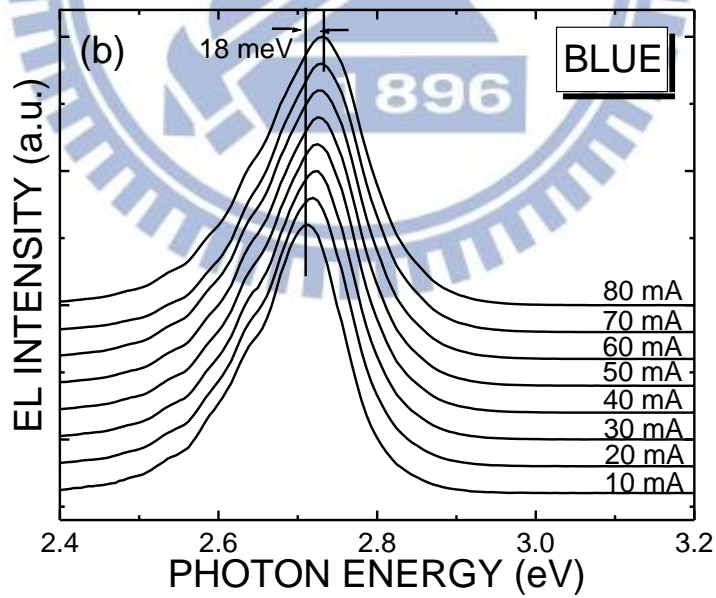
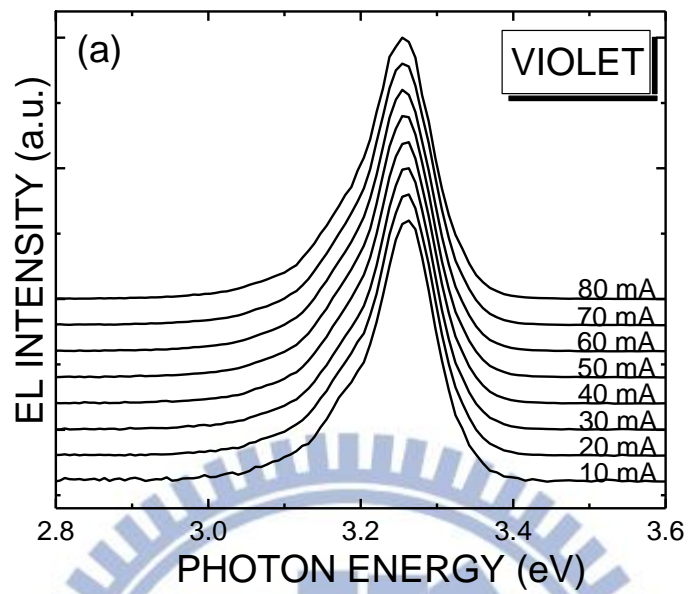
## References

- [1] S. Nakamura, M. Senoh, N. Lwasa, and S. Nagaham, *Jpn. J. Appl. Phys.*, Part 1 34 (1995) 797.
- [2] S.D. Lester, F.A. Ponce, M.G. Craford, and D.A. Steigerwald, *Appl. Phys. Lett.* 66 (1995) 1249.
- [3] S. Chichibu, T. Azuhata, T. Sota, and S. Nakamura, *Appl. Phys. Lett.* 70 (1997) 2882.
- [4] Y. Narukawa, Y. Kawakami, M. Funato, Sz. Fujita, Sg. Fujita, and S. Nakamura, *Appl. Phys. Lett.* 70 (1997) 981.
- [5] S. Chichibu, T. Azuhata, T. Sota, and S. Nakamura, *Appl. Phys. Lett.* 69 (1997) 4188.
- [6] M. Sugawara, *Phys. Rev. B* 51 (1995) 10743.
- [7] S.J. Rosner, E.C. Carr, M.J. Ludowise, G. Girolami, and H.I. Erikson, *Appl. Phys. Lett.* 70 (1997) 420.
- [8] S.Y. Karpov and Y.N. Makarov, *Appl. Phys. Lett.* 81 (2002) 4721.
- [9] P. Riblet, H. Hirayama, A. Kinoshita, A. Hirata, T. Sugano, and Y. Aoyagi, *Appl. Phys. Lett.* 75 (1999) 2241.
- [10] M. E. Aumer, S. F. LeBoeuf, S. M. Bedai, M. Smith, J. Y. Lin, and H. X. Jiang, *Appl. Phys. Lett.* 77 (2000) 821.
- [11] R. Zheng and T. Taguchi, *J. Appl. Phys.* 89 (2001) 6260.
- [12] Y.D. Qi, H. Liang, D. Wang, Z.D. Lu, W. Tang, and K.M. Lau, *Appl. Phys. Lett.* 86 (2005) 101903.
- [13] S. Chichibu, T. Sota, K. Wada, and S. Nakamura, *J. Vac. Sci. Technol. B* 16 (1998) 2204.
- [14] T. Li, A. M. Fischer, Q. Y. Wei, F. A. Ponce, T. Detchprohm, and C. Wetzel, *Appl. Phys. Lett.* 96 (2010) 031906.

- [15] A. Bell, S. Srinivasan, C. Plumlee, H. Omiya, F. A. Ponce, J. Christen, S. Tanaka, F. Fujioka, and Y. Nakagawa, *J. Appl. Phys.* 95 (2004) 4670.
- [16] Y. Kawakami, K. Omae, A. Kaneta, K. Okamoto, Y. Narukawa, T. Mukai, and S. Fujita, *J. Phys.: Condens. Matter* 13 (2001) 6993.
- [17] Y. H. Cho, G. H. Gainer, A. J. Fischer, J. J. Song, S. Keller, U. K. Mishra, and S. P. DenBaars, *Appl. Phys. Lett.* 73 (1998) 1370.
- [18] H. P. D. Schenk, M. Leroux, and P. de Mierry, *J. Appl. Phys.* 88 (2000) 1525.
- [19] J. Li, K. B. Nam, J. Y. Lin, and H. X. Jiang, *Appl. Phys. Lett.* 79 (2001) 3245.
- [20] B.E.A. Saleh and M.C. Teich, *Fundamentals of Photonics*, (Wiley, New York, 1991), p. Chap. 15.
- [21] C.H. Henry, R.A. Logan, H. Temkin, and F.R. Merritt, *IEEE J. Quantum Electron.* QE-19 (1983) 941.
- [22] C.H. Henry, R.A. Logan, and F.R. Merritt, *J. Appl. Phys.* 51 (1980) 3042.
- [23] C.H. Henry, R.A. Logan, and K.A. Bertness, *J. Appl. Phys.* 52 (1981) 4453.
- [24] P. Blood, A.I. Kucharska, J.P. Jacobs, and K. Griffiths, *J. Appl. Phys.* 70 (1991) 1144.
- [25] P. Blood, E.D. Fletcher, P.J. Hulyer, and P.M. Snowton, *Appl. Phys. Lett.* 48 (1986) 1111.
- [26] J.D. Thomson, H.D. Summers, P.J. Hulyer, P.M. Snowton, and P. Blood, *Appl. Phys. Lett.* 75 (1999) 2527.
- [27] G.M. Lewis, P.M. Snowton, J.D. Thomson, H.D. Summers, and P. Blood, *Appl. Phys. Lett.* 80 (2002) 1.
- [28] H.D. Summers, J.D. Thomson, P.M. Snowton, P. Blood, and M. Hopkinson, *Semicon. Sci. Tech.* 16 (2001) 140.

- [29] N.C. Chen, W.C. Lien, Y.K. Yang, C. Shen, Y.S. Wang, and J.F. Chen, J. Appl. Phys. 106 (2009) 074514.
- [30] N.C. Chen, C.M. Lin, C. Shen, W.C. Lien, and T.Y. Lin, Opt. Express 16 (2008) 20759.
- [31] S.M. Sze and K.K. Ng, *Physics of Semiconductor Devices 2nd Edition* (Wiley, New York, 1982), p. 61.
- [32] R. André, J. Cibert, and L.S. Dang, Phys. Rev. B 52 (1995) 12013.
- [33] S.F. Chichibu, A.C. Abare, M.P. Mack, M.S. Minsky, T. Deguchi, D. Cohen, P. Kozodoy, S.B. Fleischer, S. Keller, J.S. Speck, J.E. Bowers, E. Hu, U.K. Mishra, L.A. Coldren, S.P. DenBaars, K. Wada, T. Sota, S. Nakamura, Mater. Sci. Eng. B 59 (1999) 298.
- [34] C.K. Choi, Y.H. Kwon, B.D. Little, G.H. Gainer, J.J. Song, Y.C. Chang, S. Keller, U.K. Mishra, and S.P. DenBaars, Phys. Rev. B 64 (2001) 245339.







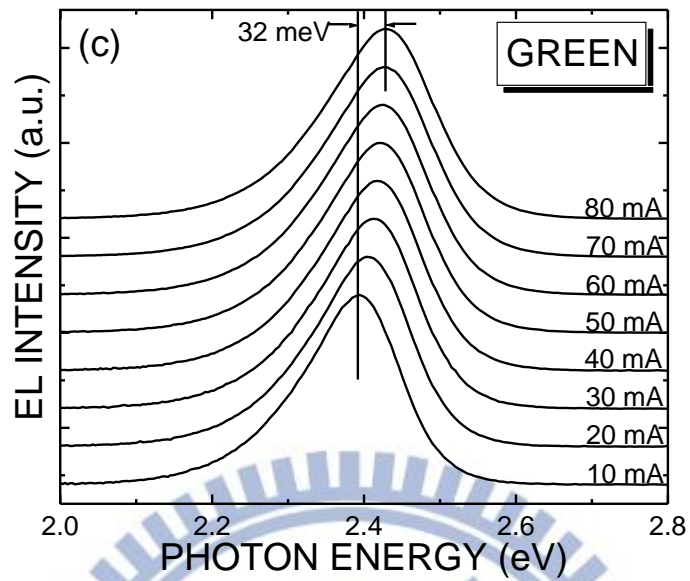


Fig. 4.1. EL spectra of (a) violet, (b) blue, and (c) green InGaN/GaN-based LEDs at various currents from 10 to 80 mA at 300K. Emission peak shifts in the three spectra are 0 meV, 19 meV, and 37 meV, respectively

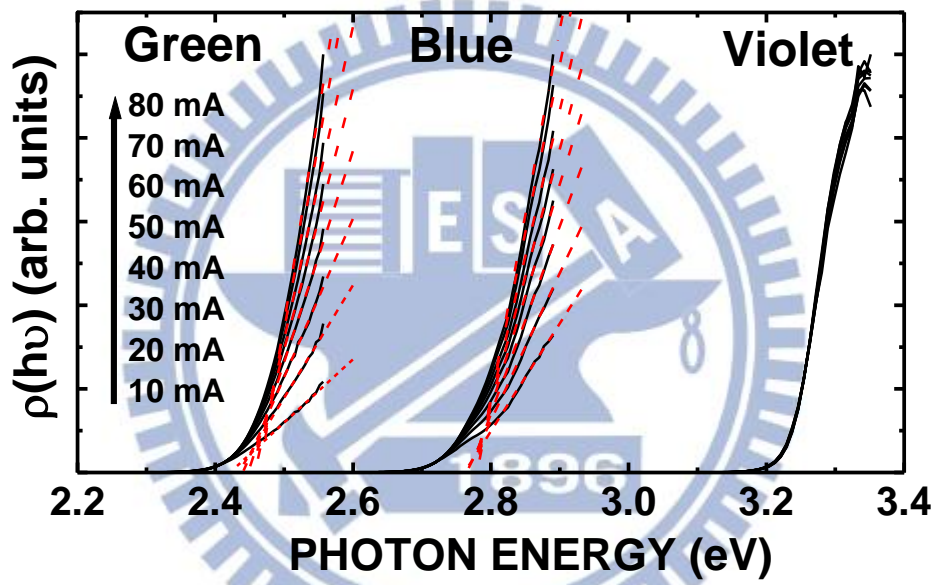


Fig. 4.2. Relative optical joint density of states in violet, blue, and green LEDs under currents from 10 to 80 mA, calculated by dividing EL spectra by thermal distribution

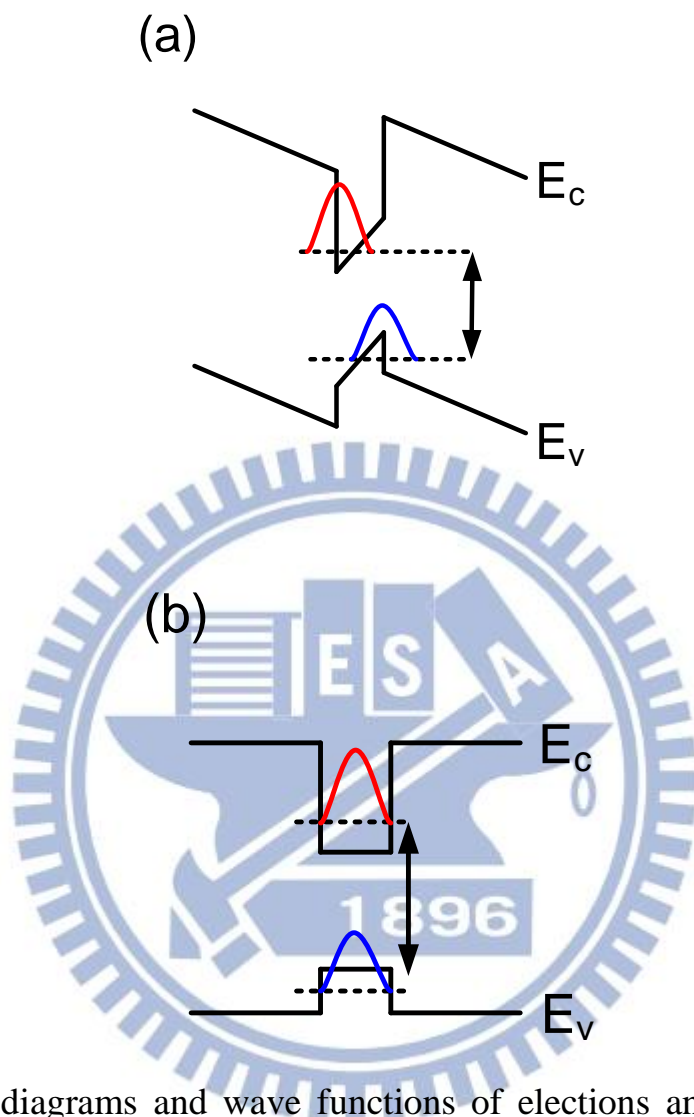
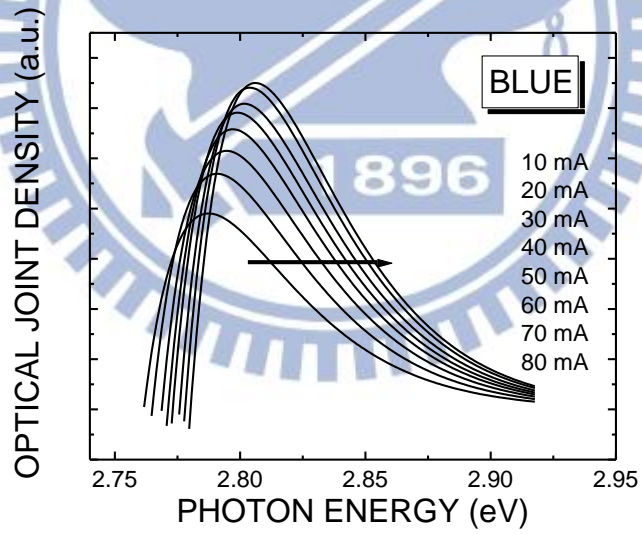
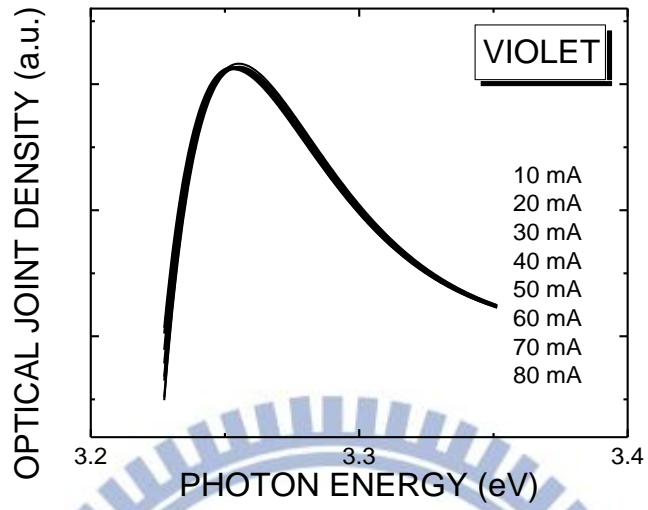


Fig. 4.3. Band diagrams and wave functions of electrons and holes under (a) piezoelectric field and (b) screened piezoelectric field



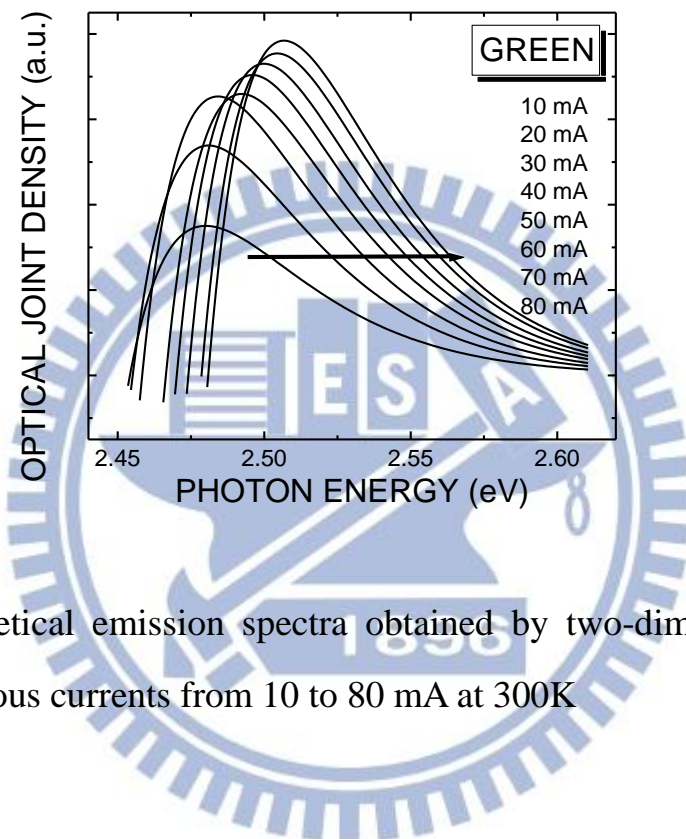


Fig. 4.4. Theoretical emission spectra obtained by two-dimensional quantum structure at various currents from 10 to 80 mA at 300K

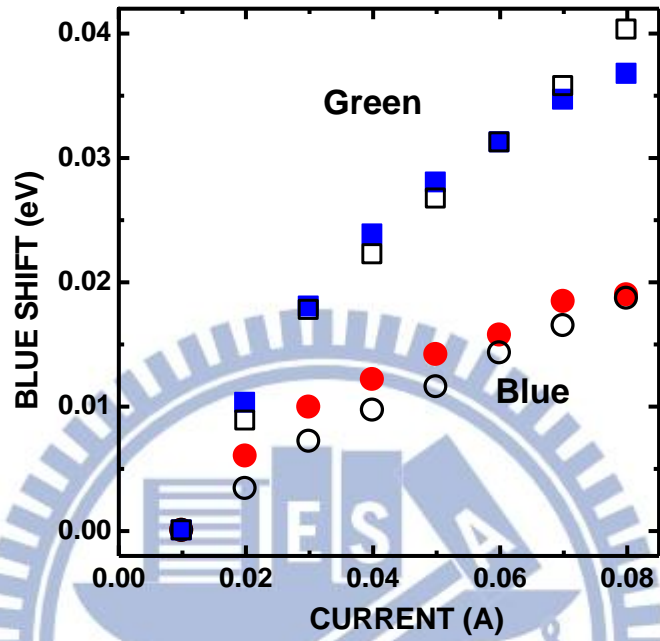
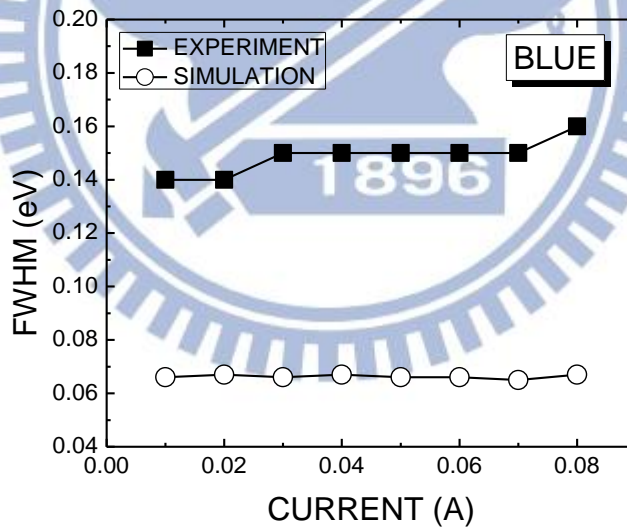
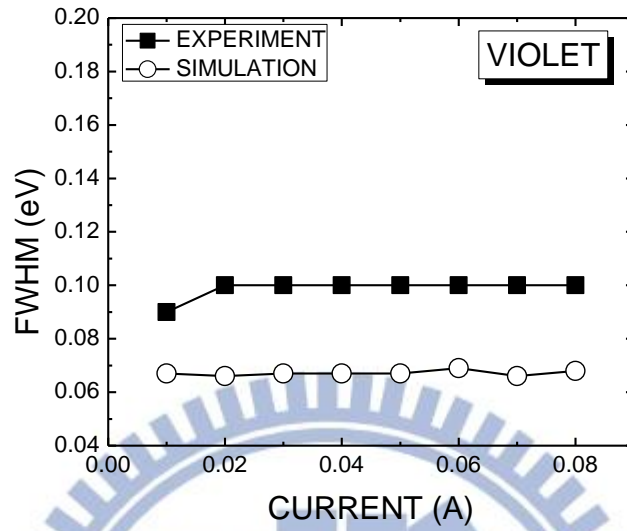


Fig. 4.5. Experimental and theoretical EL peak shifts with current in blue (green) LED are denoted by solid circles (solid squares) and open circles (open squares), respectively



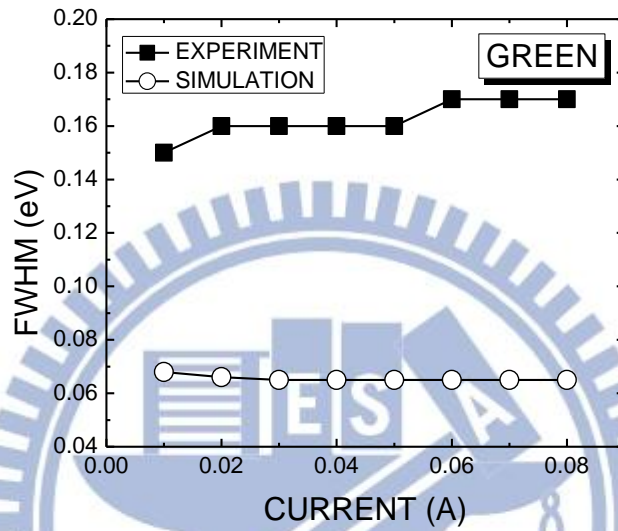


Fig. 4.6. The FWHMs of the experimental spectra and simulated spectra for violet, blue and green LEDs



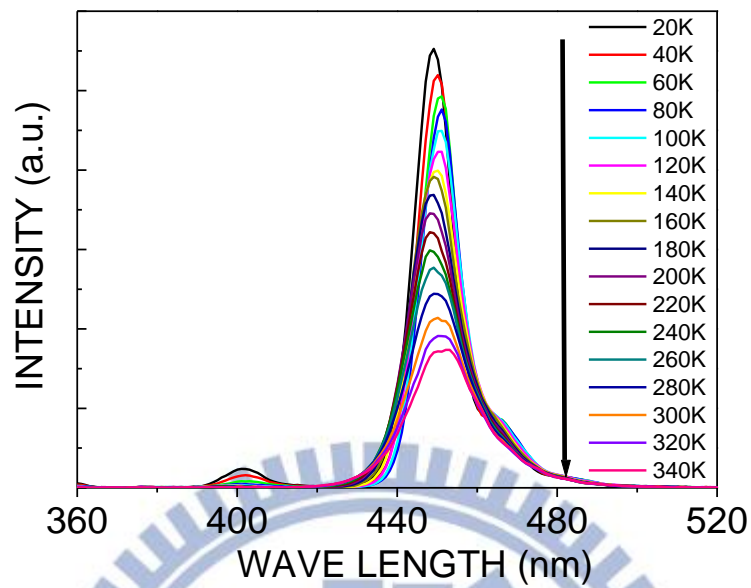


Fig. 4.7. PL spectra of an LED at various temperatures from 20 to 340K

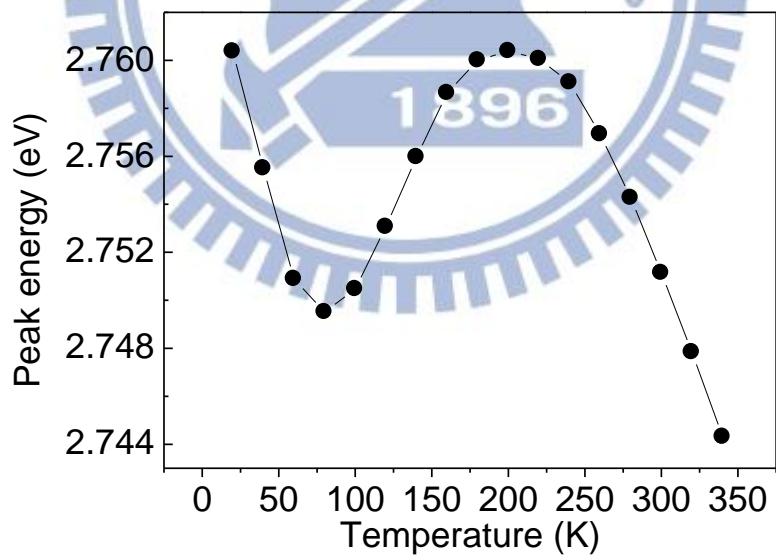


Fig. 4.8. The emission peak positions of the PL spectra at various temperatures from 20 to 340K

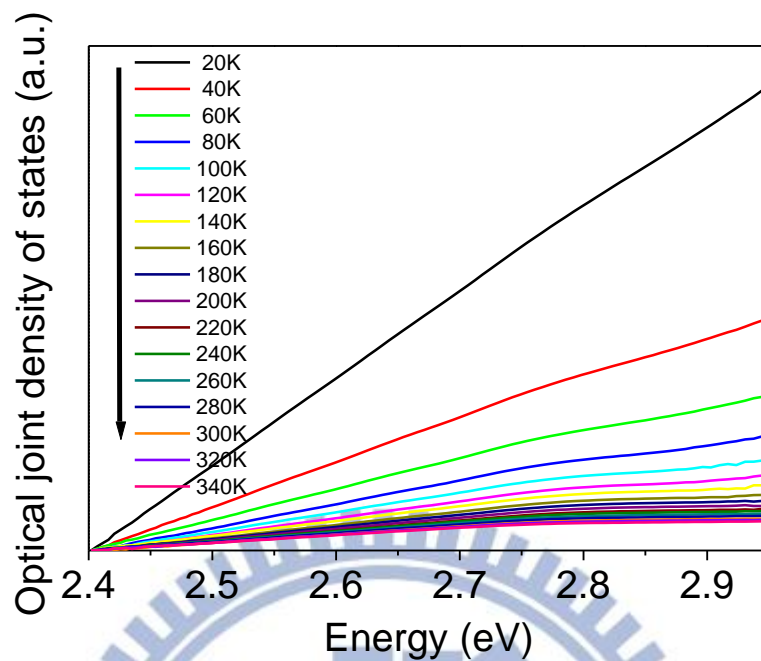


Fig. 4.9. Relative optical joint density of states under temperatures from 20 to 340K, calculated by dividing PL spectra by thermal distribution

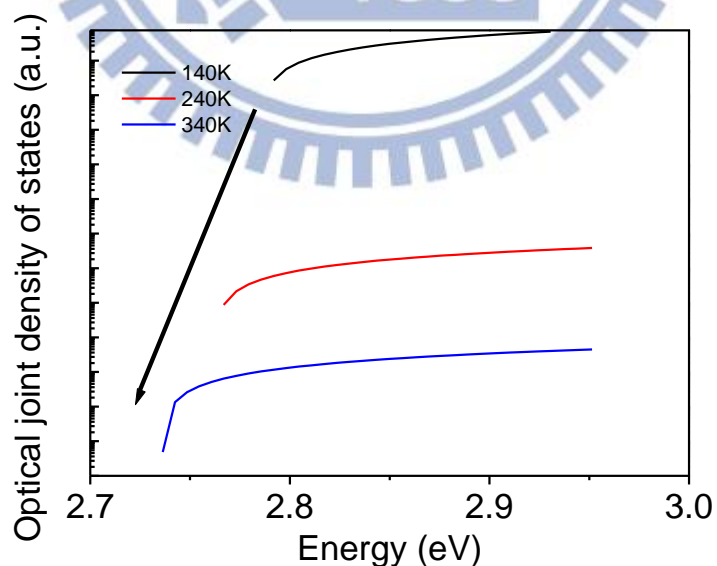


Fig. 4.10. The linear fitted lines of the step increased of optical joint density of states at 140K, 240K and 340K

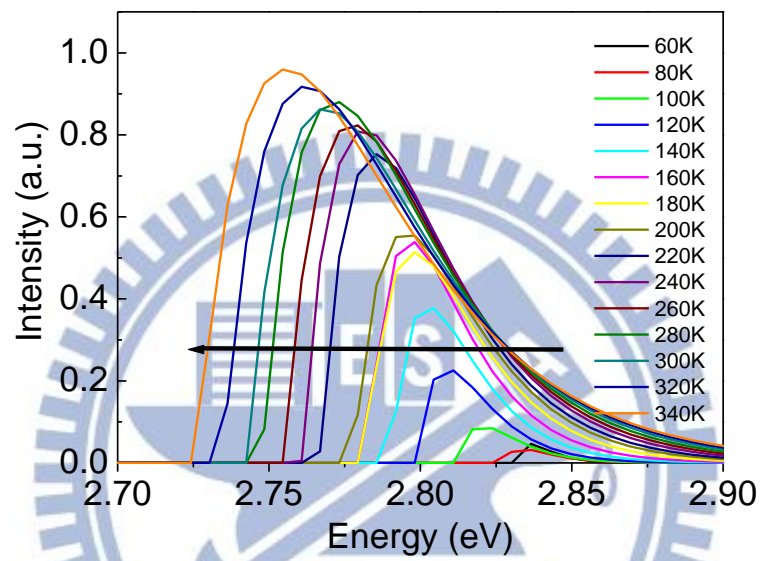


Fig. 4.11. The theoretical emission spectra obtained by two-dimensional quantum structure from 20 to 340K

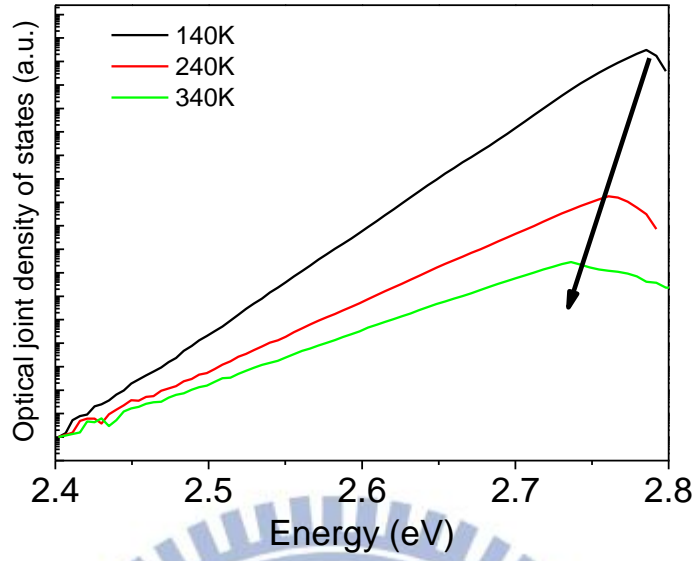


Fig. 4.12. The optical joint density of states with eliminating linear fitted lines at 140K, 240K and 340K

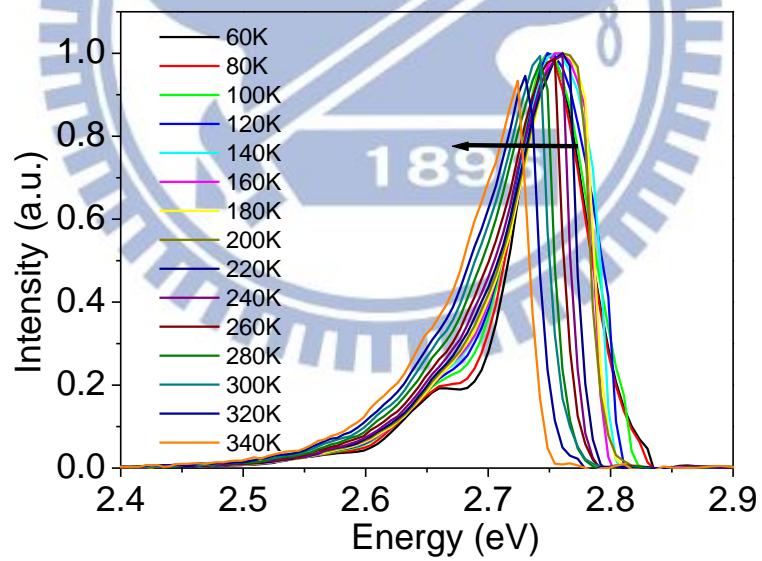


Fig. 4.13. The theoretical emission spectra obtained by localized states from 20 to 340K

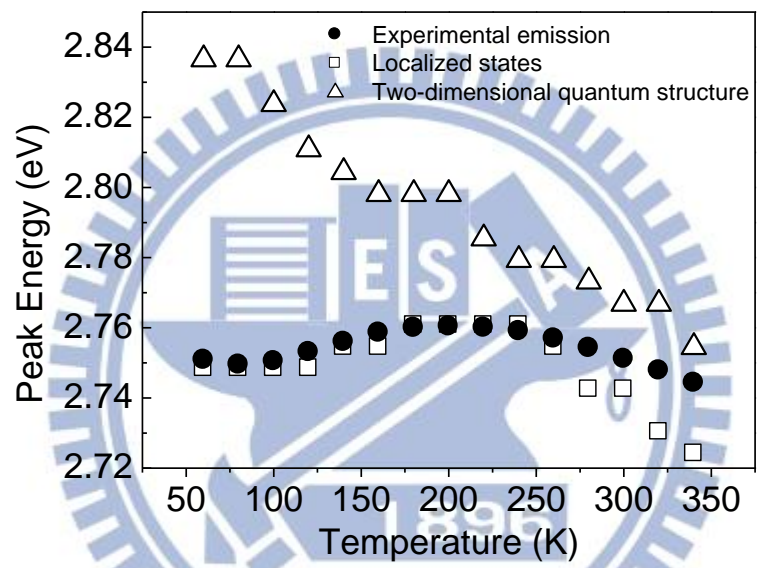


Fig. 4.14. The peak positions of experimental emission spectrum and theoretical emission spectrum obtained by two-dimensional quantum structure and localized states from 60 to 340K

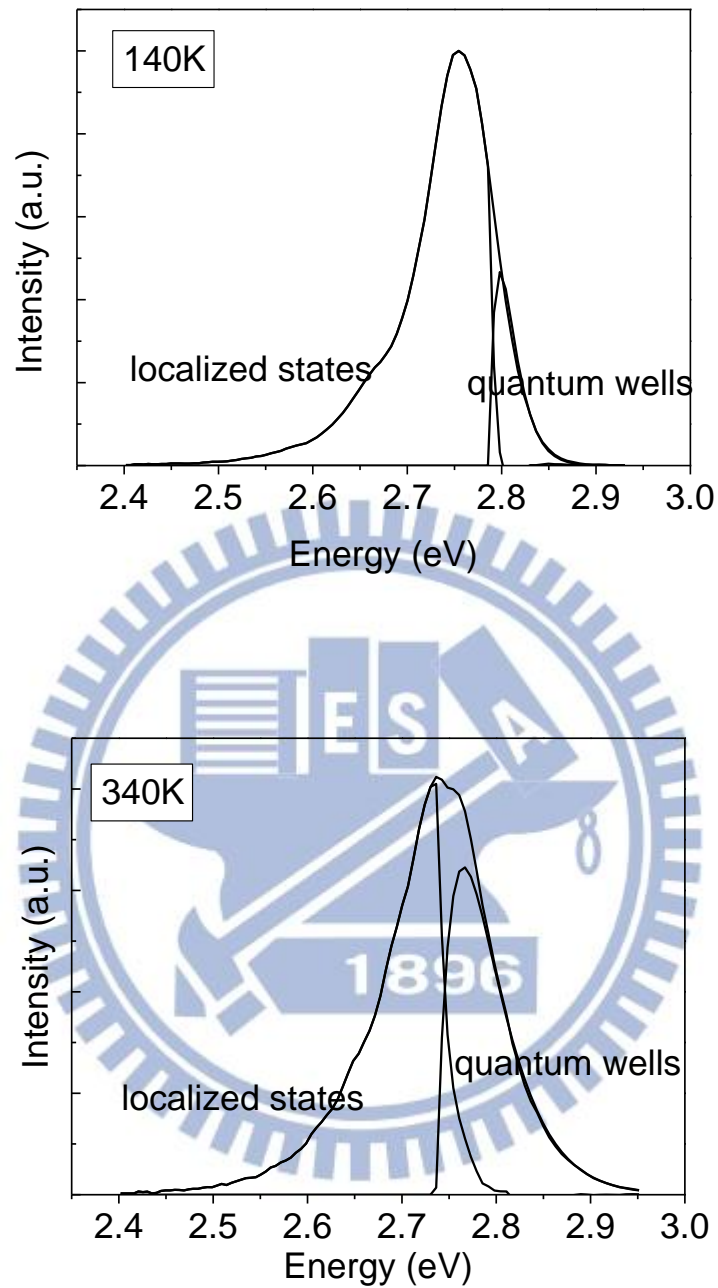


Fig. 4.15. The experimental emission spectrum and theoretical emission spectrum obtained by two-dimensional quantum structure and localized states at (a) 140 K and (b) 340K

# Chapter 5 Diffusion-controlled effects of luminescence efficiency in InGaN/GaN light-emitting diodes

## 5.1. Introduction

In this chapter, the influence of the dislocation in nitride LEDs was investigated. Although much investigation of dislocations, which are recognized as nonradiative centers, has been reported in decades, the mechanism of emission luminescence is still much left unknown. The most attractive feature is the peculiarly high luminescence efficiency despite high dislocation density (typically in the range of  $10^8$ - $10^{10}$  cm<sup>-2</sup>) [2,3]. Many studies have addressed that the reason for the high efficiency is attributed to the formation of localized states which are formed by self-organized of In-rich regions in wells. Therefore, excitons are more likely associated with localized states and recombine radiatively rather than captured by dislocations and then recombine nonradiatively [4]. On the other hand, some groups suggested that the dislocation provides an inner potential barrier to prevent carriers to be captured into it while it gathers a large number of negative charges and the potential barrier can be estimated by using Shockley-Read-Hall (SRH) theory [5,6]. It should be noticed that this theory has been widely used to investigate the thermal quenching mechanism [7], such as quantum dots, quantum wells or point defects. However, P. Ščajev *et al.* [8] argued that the diffusive flow of carriers to grain boundaries may lead to interface recombination at dislocations, thus, carriers should diffuse toward the dislocations before captured by dislocations. Similar to the chemical reaction process, diffusion of reactants

should be involved until they encounter each other in the right stoichiometry and from an activated complex. Also, the observed rate of chemical reactions is the rate of the slowest step. In diffusion controlled reactions, when the formation of activated complex is much faster than the diffusion of reactants, the rate is governed by diffusion. Such investigation have been report by Wight *et al.*[9] by using diffusion-controlled kinetics to explain the recombination process for line-sink defects (dislocations) in *n*-type GaP, as shown in Fig. 5.1, and S. Y. Karpov *et al.*[10] used the two-dimensional steady-state diffusion equation to estimate the light emission efficiency in GaN. Moreover, this phenomenon, the inhomogeneity of dark regions which present the locations of threading dislocation, can be observed by cathodoluminescence (CL) images and provides that diffusion process may be an important role in the nonradiative recombination process [11,12]. Since the investigations of diffusion-controlled kinetics on the emission mechanism in InGaN/GaN QWs are rarely discussed, more scientific researches in this issue are still needed.

In this work, the dynamic of recombination process in InGaN/GaN LEDs with diffusion-controlled kinetics was investigated by using temperature dependence of photoluminescence (PL) and time-resolve photoluminescence (TRPL). The influence of localized states and the impact of threading dislocations on luminescence efficiency are discussed in detail.

## 5.2 Experiments

The sample studied was a typical LED structure and grown on a *c*-plane sapphire substrate in a vertical Thomas Swan metal organic chemical vapor deposition (MOCVD) system. First, a 20 nm thick GaN nucleation layer was grown at 620°C, followed by a 0.5 $\mu$ m-thick GaN buffer layer and 3 $\mu$ m-thick



*n*-type GaN grown at 1200°C, respectively. Then, 9 pairs of multiple quantum wells (MQWs) consisting of a 2nm InGaN well grown at 885°C and a 8nm GaN barrier at 990°C. Thereafter, a 100nm *p*-type AlGaN electron blocking layer and a 200nm *p*-type GaN were sequentially deposited at 1080°C and 1060°C, respectively. Hydrogen was used as carrier gas and switched to nitrogen while growing MQWs. The source gases were trimethylgallium, triethylgallium, trimethylindium, trimethylaluminum, and ammonia. Silicon and biscyclopentadienylmagnesium were used for *n*-type dopant source and *p*-type dopant source, respectively. The microstructure of the sample and the carrier density in QWs were measured by transmission electron microscopy (TEM) and capacitance-voltage method, respectively. The temperature dependence of PL and TRPL were excited by a 325nm He-Cd laser.

### 5.3. Transmission electron microscopy

Figure 5.2 shows a TEM cross-sectional image of the sample, and a large number of threading dislocations threading through the quantum wells can be exhibited. Since the average distance between the dislocations is around 500nm, the dislocation density can be briefly calculated  $1/\pi(500nm)^2 \approx 1.27 \times 10^8 cm^{-2}$ , which is a typical value for nitride LEDs. Symbol A and B are present the positions of normal well and dislocation, respectively.

### 5.4 Photoluminescence

Figure 5.3 shows the PL intensity for the sample. The PL intensity of the sample weakly depended on temperature when temperature was <100K and decreased steeply when temperature was >100K. Furthermore, when the temperature was increased to 300K, the PL intensity was 23% of that at 20K. Figure 5.4 shows the Arrhenius plots of the PL emission and can be fitted by the

follow equation:

$$I(T) = \frac{I(0)}{1 + a \exp\left(-\frac{E_A}{K_B T}\right)} \dots\dots\dots (5.1)$$

The thermal activation energy  $E_A$  in our sample is approximately 20meV which is attributed to thermal delocalization of carriers from localized states to quantum wells and leading to the decrease of PL intensity.

### 5.5 Time-resolved photoluminescence

To further explain the decrease of luminescence efficiency and the dynamic of recombination process with varying temperature, the temperature dependence of carrier lifetime  $\tau_{PL}$  was measured by TRPL, as shown in Fig 5.5(a) and Fig 5.5(b). Since the diffusion lifetime is dominated by recombination of holes, the diffusion length of the sample can be approximated as,  $\ell = \sqrt{D_h \tau_c}$ , where  $D_h$  is diffusion coefficient of holes. At the lowest temperature, the diffusion length of the sample was estimated to be around 279nm, where  $\tau_c = 11.7ns$  and  $D_h = 0.07 cm^2/s$  at 25K. It indicated that the diffusion length is shorter than the average distance between dislocations at low temperature, thus, the electron-hole pairs will not move toward the dislocations. However, when the temperature increased to 300K, the diffusion length of the sample was increased to 780nm which is larger than the average distance between dislocations, where  $\tau_c = 7.16ns$  and  $D_h = 0.85 cm^2/s$  [16] at 300K. Therefore, the electron-hole pairs should move toward the dislocations, and the luminescence efficiency was decreased at high temperature.

Furthermore, since the internal quantum efficiency of the sample can be estimated from normalized PL intensity, as shown in Fig. 5.6(a):

$$\eta = \frac{\tau_{nr}}{\tau_r + \tau_{nr}} \dots\dots\dots(5.2)$$

And since carrier recombination contains radiative recombination and nonradiative recombination, the radiative lifetime  $\tau_r$  and the nonradiative lifetime  $\tau_{nr}$  herein can be separated from  $1/\tau_c = 1/\tau_r + 1/\tau_{nr}$  [17], as shown in Fig. 5.6(b). It shows that the radiative lifetime was temperature independent when the temperature was <100K and was linearly increase with temperature when temperature was >100K. On the other hand, the nonradiative lifetime decreased rapidly with temperature and mainly dominated the carrier lifetime when the temperature was >250K. By comparing with the PL measurement, the temperature dependence of luminescence efficiency is correlated with the variation of radiative lifetime and nonradiative lifetime with temperature. When the temperature was <100K, the weakly temperature dependence of PL intensity is attributed to the temperature independence of radiative lifetime and the nonradiative is extremely larger than the radiative lifetime. It indicated that when temperature was <100K, the electron-hole pairs were mainly associated with localized states where are recognized as a zero-dimensional system, and since the temperature is low, the diffusion coefficient should very small and the electron-hole pairs will not move a long distance before recombining. However, when the temperature was >100K, the electron-hole pairs are no longer quenched in localized states and recombining in two-dimensional system. Therefore, the electron-hole pairs can move a long distance toward dislocations and then recombine nonradiatively.

To investigate the recombination processes in InGaN/GaN LEDs, the schematic of the processes are presented in Fig. 5.7. Symbol A and B are the

positions of normal well and dislocation, respectively. The electron-hole pairs in wells herein is assumed to be optically generated uniformly by a 325nm laser, and the recombination rate in the region of normal well (point A) and dislocation (point B) is obtained by bimolecular recombination process and SRH theory, respectively. Since dislocations are locally distributed and the recombination rates in wells are different, the electron-hole pairs in wells are non-uniform and then should diffuse from a region of higher concentration toward a region of lower concentration. To simplify the investigation of recombination processes, some conditions herein are considered; the radiative recombination rate in every region of well is equal, and the effects of point defects, well width fluctuation, indium composition fluctuation and localized states are neglected. Thus, the radiative recombination rate and nonradiative recombination rate in this work can be presented and discussed below, respectively.

### 5.6 Radiative lifetime

In radiative recombination process, the electron-hole pairs generated at point A can recombine radiatively, and the radiative lifetime can be obtained by the following expression:

$$\tau_r = \frac{1}{Bn_0} \dots\dots\dots(5.3)$$

where  $\tau_r$  is radiative lifetime,  $B$  is bimolecular coefficient and  $n_0$  is background net donor concentration in wells. According to the correlation between bimolecular coefficient and temperature, the radiative lifetime is linear

dependent with temperature in two-dimensional system ( $B_{2D} \propto T^{-1}$ ) [13] and temperature independent in zero-dimensional system ( $B_{0D} \propto T^0$ ) [14].

Since both PL intensity and radiative lifetime of the sample were temperature independent when temperature was  $< 100\text{K}$ , the recombination process of carriers can be mainly correlated to the localized states. The formation of localized states in InGaN/GaN quantum wells are resulting from the spontaneously formed of In-rich regions which act as ODs. Thus, carriers at low temperature should be recombined in zero-dimensional system. Furthermore, the radiative lifetimes with different wavelength at lowest temperature were also investigated, as shown in Fig. 5.8(a). The decay time increase as the emission energy decreases, and saturate on the low-energy side, as shown in Fig. 5.8(b). The decay time of excitons is not only due to radiative recombination but also to transfer processes to the low-energy tail. The low energy tail originates from small potential fluctuations of either the indium composition or the well width. The energy tail in InGaN quantum wells can be modeled by using mobility edge formalism. Between the mobility edge and the exciton energy in the tail, the weakly localized states overlap with the extended states, but below the mobility edge, these localized states eventually become separated. M. Oueslati *et al.* [8] presented a model to describe the density of localized states, as shown in Fig. 5.9, and the dynamic of the recombination process of can be written as:

$$\frac{dn(E,t)}{dt} = -\frac{n(E,t)}{\tau(E)} - \sum_{E' < E} W(E \rightarrow E')n(E,t) + \sum_{E' > E} W(E' \rightarrow E)n(E',t) \dots\dots\dots (5.4)$$

and the decay time as a function of emission energy can be compared with a fitting function:

$$\tau_{PL} = \frac{\tau_{rad}}{1 + \exp\left(\frac{E - E_m}{E_0}\right)} \dots\dots\dots (5.5)$$

where  $\tau_{PL}$  is PL decay time,  $\tau_{rad}$  is radiative lifetime,  $E_m$  is mobility edge, and  $E_0$  is the activation energy, as shown in Fig. 5.10. Here, we have  $E_0 \approx 30meV$  which is similar to the activation obtained by Arrhenius plots of PL intensity. In this case, the weak localized states are overlapped with these extended states, and carriers should be transfer toward the local potential minima at low temperature. This is the reason why excitons recombine in localized states and the radiative lifetime is temperature independent at low temperature.

### 5.7 Nonradiative lifetime

In nonradiative recombination process, since dislocations are locally distributed, the electron-hole pairs should overcome the diffusion reaction toward the dislocations before captured by dislocations. Therefore, the nonradiative lifetime is the sum of diffusion lifetime of carriers from point A to point B and capture lifetime by dislocations. The capture lifetime can be written by SRH theory [5]:

$$\tau_{SRH} = \frac{1}{N_T \rho_T v_{th}} \dots\dots\dots (5.6)$$

where  $N_T$  is trap concentration,  $\rho_T$  is capture cross section and  $v_{th}$  is thermal velocity. Since dislocations are recognized as an efficient sink and some authors considered that nonraditaive recombination velocity at a dislocation is assumed to be infinite for minority carriers, the capture lifetime can be neglected in this work. Therefore, the nonraditaive recombination process should be

dominated by diffusion-controlled and the nonradiative lifetime can be given by the following expression [9]:

$$\tau_D = \frac{1}{4\pi\rho_D D} \left[ -\ln(\pi\rho_D r_0^2) - \frac{6}{5} \right] \dots\dots\dots(5.7)$$

where  $\rho_D$  is dislocation density,  $D$  is diffusion coefficient and  $r_0$  is effective capture distance. In equation 6, the diffusion lifetime is related to dislocation density and diffusion coefficient. Since the diffusivity of holes is much slower than electrons, the diffusion lifetime should be dominated by recombination of holes.

Here, the diffusion coefficient is obtained by Fick's law:

$$J = -eD_h \nabla h \dots\dots\dots(5.8)$$

where the diffusion coefficient of hole ( $D_h$ ) is composed of thermal velocity ( $v_{th}$ ) and mean-free path ( $l$ ).

$$D_h = v_{th} \times l \dots\dots\dots(5.9)$$

The mean-free path is the average distance a hole travels between collisions ( $l = v_{th} \times \tau_{ch}$ ). Where  $\tau_{ch}$  is the average relaxation time of hole.

The thermal velocity is  $v_{th} = \sqrt{\frac{2kT}{m_h^*}}$  in two dimensional and  $v_{th} = \sqrt{\frac{3kT}{m_h^*}}$  in three dimensional. Thus, the diffusion coefficient can be written as

$$D_h = \frac{2KT}{m_h^*} \times \tau_{ch} \quad (2-D) \dots\dots\dots(5.10)$$

$$D_h = \frac{3KT}{m_h^*} \times \tau_{ch} \quad (3-D) \dots\dots\dots(5.11)$$

Since relaxation time is related to the scattering mechanism, the temperature dependence of diffusion coefficient is varied with different scattering mechanisms. In GaN, there are different types of scattering mechanisms

dominate the relaxation time: ionized impurity scattering, neutral impurity scattering, deformation potential acoustic phonons scattering, piezoelectric acoustic phonons scattering and dislocation scattering. In a typical nitride based LED, there are no Si doping in InGaN wells. Thus, ionized impurity scattering would not occur and neutral impurity scattering dominate the relaxation time in the low temperature range. The relaxation time of neutral impurity scattering can be estimated as below.

$$\tau_{ni} = \frac{m_h^*}{20N_h\hbar a_0} \dots\dots\dots(5.12)$$

where  $N_h$  is the concentration of neutral impurity and  $a_0$  is the effective Bohr radius of acceptor. It is temperature independence and the temperature dependence of diffusion coefficient can be obtained ( $D \propto T$ ) in the low temperature range. As the temperature increases from high temperature range, the lattice scattering becomes to dominate the relaxation time. The relaxation time of deformation potential acoustic phonons scattering is considered shortest in the lattice scattering mechanism. Thus, the deformation potential scattering dominated the relaxation time in the high temperature and can be written as

$$\tau_{dp} = \frac{\sqrt{8\pi}\hbar^4 c_1}{3m_h^{*3/2}(KT)^{3/2} E_1^2} \dots\dots\dots(5.13)$$

where  $c_1$  is the longitudinal elastic constants and  $E_1$  is the acoustic deformation potential. Thus, the temperature dependence of diffusion coefficient can be obtained ( $D \propto T^{-1.5}$ ) in the high temperature range. Moreover, the variation of diffusion-limited lifetime with temperature is controlled by the temperature dependence of diffusion coefficient ( $\tau_{id} \propto T^{-1}$  in the low temperature range and  $\tau_{id} \propto T^{1.5}$  in the high temperature range).



In addition,  $\tau_{ch}$  in a semiconductor is obtained by  $\tau_{ch} = \mu_h \frac{m_h^*}{e}$ , then the diffusion coefficient can be rewritten as

$$D_h = \mu_h \frac{2KT}{e} \quad (2-D) \dots \dots \dots (5.14)$$

$$D_h = \mu_h \frac{3KT}{e} \quad (3-D) \dots \dots \dots (5.15)$$

where  $\mu_h$  is the mobility of holes and the diffusion coefficients are obtained by Einstein relation. Therefore, the temperature dependence of nonradiative lifetime can be estimated from diffusion coefficient obtained by Einstein relation ( $D \sim \mu_h \frac{KT}{e}$ ). In two-dimensional system, the excess carrier mobility is mainly dominated by neutral impurity scattering which is temperature independent [15]. Therefore, the trend of diffusion lifetime with varying temperature can be estimated ( $\tau_D \propto T^{-1}$ ). Since the trend of theoretical nonradiative lifetime with varying temperature is ( $\tau_D \propto T^{-1}$ ) which is mainly dominated by diffusion control, the experimental result shows well fitted with the trend, as shown in Fig. 5.11. It implies that the nonradiative recombination process is mainly dominated by diffusion control in the range of 20-300K.

To further validate the theoretical results, the radiative lifetime and nonradiative lifetime at 300K were estimated by using the Eq (1) and Eq (3) respectively, for bimolecular coefficient  $B = 1.45 \times 10^{-10} \text{ cm}^3 \text{ s}^{-1}$ , background concentration of electrons  $n_0 = 1 \times 10^{17} \text{ cm}^{-3}$ , dislocation density  $\rho_D = 1.27 \times 10^8 \text{ cm}^{-2}$ , diffusion coefficient of holes  $D_h = 0.85 \text{ cm}^2/\text{s}$  and effective capture distance  $r_0 = 3.178 \times 10^{-8} \text{ cm}$ . Here, we have  $\tau_r = 68.9 \text{ ns}$  and  $\tau_D = 11.7 \text{ ns}$  which are in good agreement with the experimental results. Therefore, both the radiative

lifetime and nonradiative lifetime can be estimated and fully ascribed by using this method.

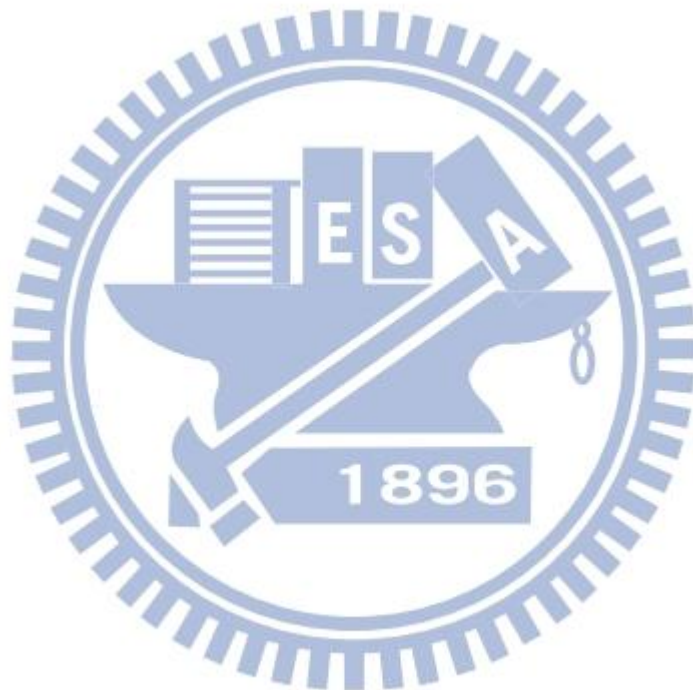
## 5.8 Conclusion

In conclusion, the temperature dependence of PL and TRPL of InGaN/GaN LEDs were investigated and we presented a method to describe the recombination processes. The results exhibited that the decrease of luminescence efficiency with temperature is attributed to the increase of radiative lifetime and decrease of nonradiative lifetime. In radiative recombination process, the electron-hole pairs recombined in zero-dimensional when temperature was  $<100\text{K}$  which is attributed to the existence of localized states, and recombined in two-dimensional process when temperature was  $>100\text{K}$  which is attributed to a typical quantum-confined effect. In nonradiative recombination process, since dislocations which act as line sinks for minority carriers are locally distributed, and the nonradiative lifetime was found to be correlated with diffusion coefficient with varying temperature, the nonradiative recombination process are mainly dominated by diffusion-controlled kinetics. Therefore, both radiative lifetime and nonradiative lifetime can be estimated by using this method and the theoretical results are in agreement with the experimental results.

## References

- [1] S. Nakamura, M. Senoh, N. Lwasa, and S. Nagaham, *Jpn. J. Appl. Phys. Part 1* 34, 797 (1995).
- [2] S. D. Lester, F. A. Ponce, M. G. Craford, and D. A. Steigerwald, *Appl. Phys. Lett.* 66, 1249 (1995).
- [3] D. Cherns, S. J. Henley, and F. A. Ponce, *Appl. Phys. Lett.* 78, 2691 (2001).
- [4] S. Chichibu, T. Azuhata, T. Sota, and S. Nakamura, *Appl. Phys. Lett.* 69, 4188 (1997).
- [5] T. Wosiński, *J. Appl. Phys.* 65, 1566 (1989).
- [6] D. Cherns and C. G. Jiao, *Phys. Rev. Lett.* 87, 205504 (2001).
- [7] D. S. Jiang, H. Jung, and K. Ploog, *J. Appl. Phys.* 64, 1371 (1988).
- [8] P. Ščajev, A. Usikov, V. Soukhoveev, R. Aleksiejūnas, and K. Jarašiūnas, *Appl. Phys. Lett.* 98, 202105 (2011).
- [9] D. R. Wight, I. D. Blenkinsop, and W. Harding, *Phys. Rev. B* 23, 5495 (1981).
- [10] S. Y. Karpov and Y. N. Makarov, *Appl. Phys. Lett.* 81, 4721 (2002).
- [11] S. J. Rosner, E. C. Carr, M. J. Ludowise, G. Girolami, and H. I. Erikson, *Appl. Phys. Lett.* 70, 420 (1997).
- [12] N. Pauc, M. R. Phillips, V. Aimez, and D. Drouin, *Appl. Phys. Lett.* 89, 161905 (2006).
- [13] J. Feldmann, G. Peter, E. O. Göbel, P. Dawson, K. Moore, C. Foxon, and R. J. Elliott, *Phys. Rev. Lett.* 59, 2337(1987).
- [14] J. S. Huang, Z.Chen, X. D. Luo, Z. Y. Xu, and W. K. Ge, *J. Crystal Growth* 260, 13 (2004).
- [15] S. Gökden, *phys. Stat. sol. (a)* 200 (369).

- [16] R. Aleksiejūnas, M. Sūdžius, T. Malinauskas, J. Vaitkus, K. Jarašiūnas, S. Sakai, Appl. Phys. Lett. 83, 1157 (2003).
- [17] R. C. Miller, D. A. Kleinman, W. A. Nordland, Jr., and A. C. Gossard, Phys. Rev. B 22, 863 (1980).



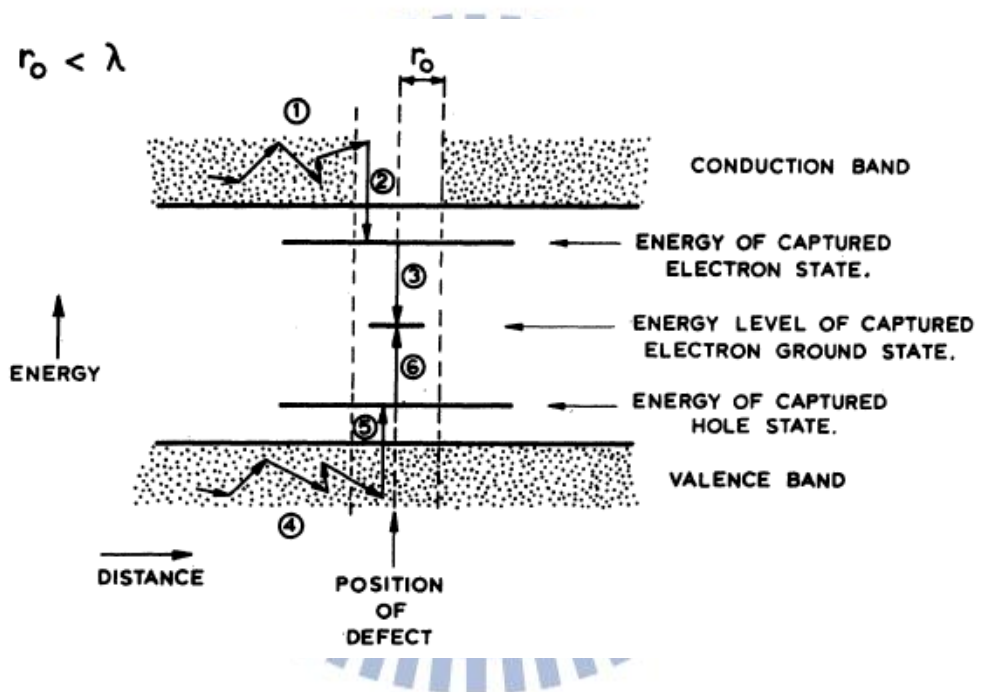


Fig. 5.1 Diffusion-controlled kinetics of recombination process for line-sink defects [9]

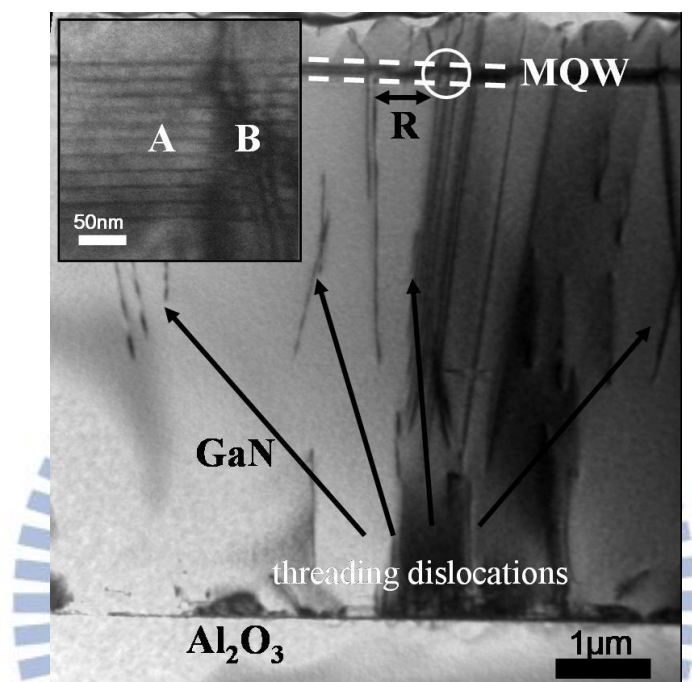


Fig. 5.2. Cross-sectional TEM image of the LED structure. Inset: magnified TEM shows a dislocation thread through the active layers where point A is the location of active layers and point B is the location of a dislocation

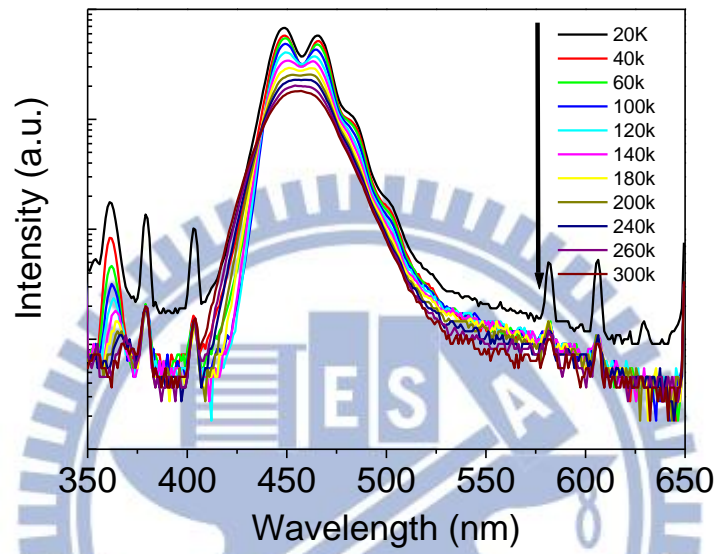


Fig. 5.3. Temperature dependence of PL spectra

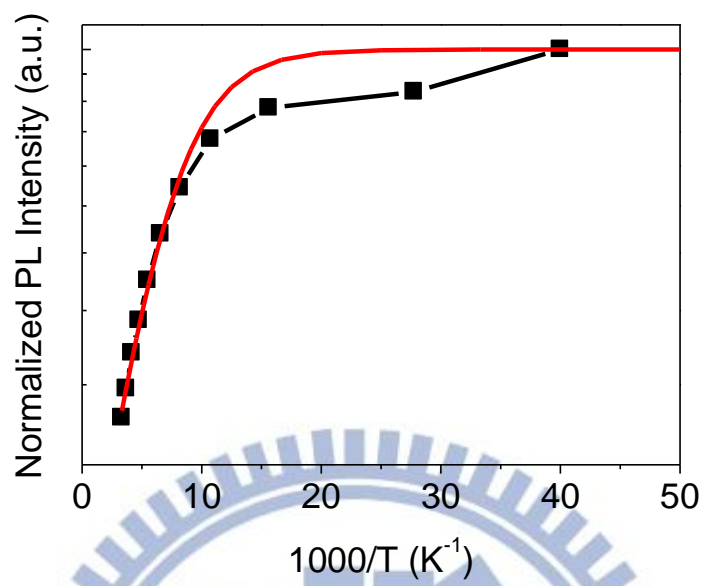


Fig. 5.4. The fitted Arrhenius plot of the PL intensity



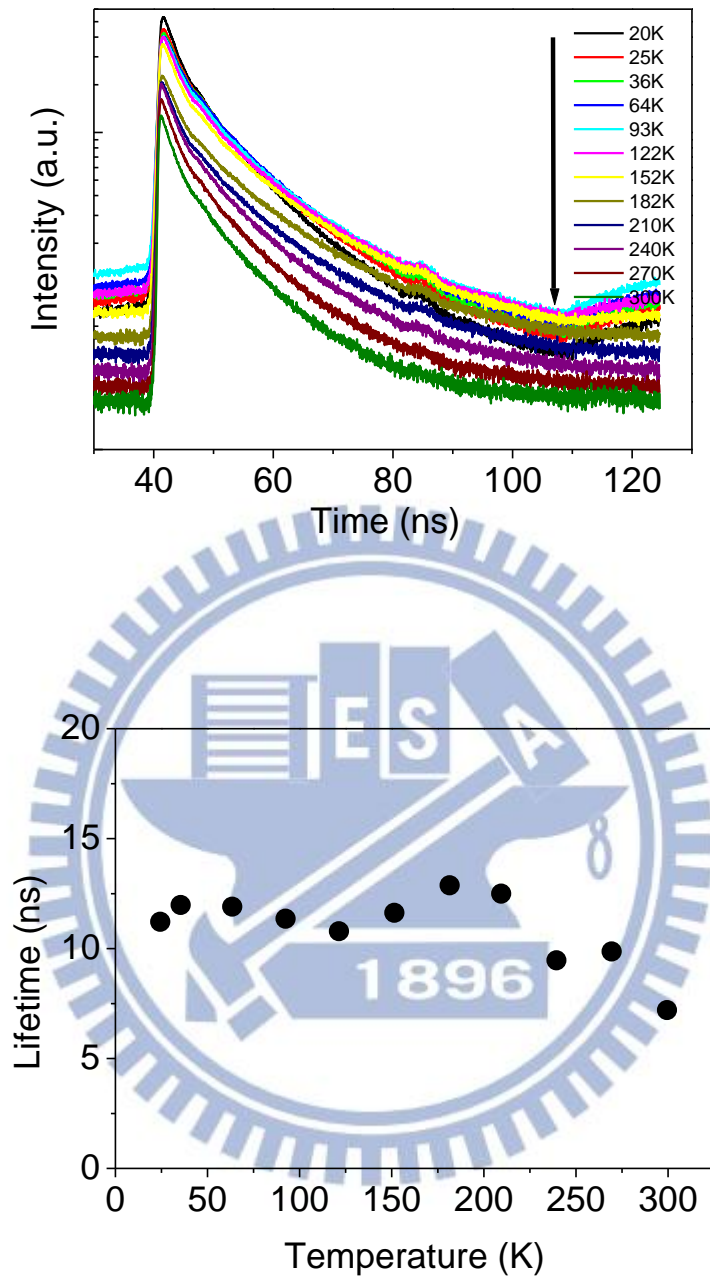


Fig. 5.5. (a) Temperature dependence of TRPL (b) Temperature dependence of the PL lifetimes

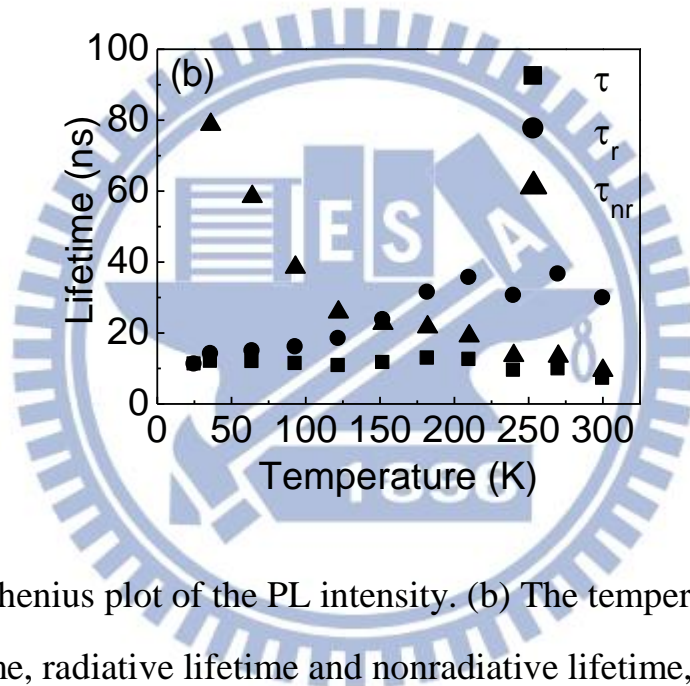
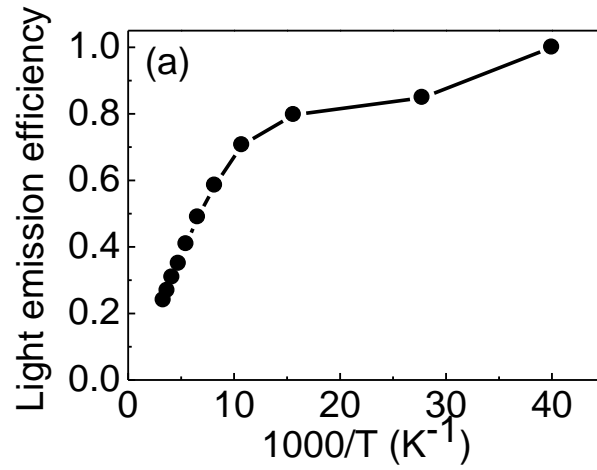


Fig. 5.6. (a) Arrhenius plot of the PL intensity. (b) The temperature dependence of carrier lifetime, radiative lifetime and nonradiative lifetime, respectively

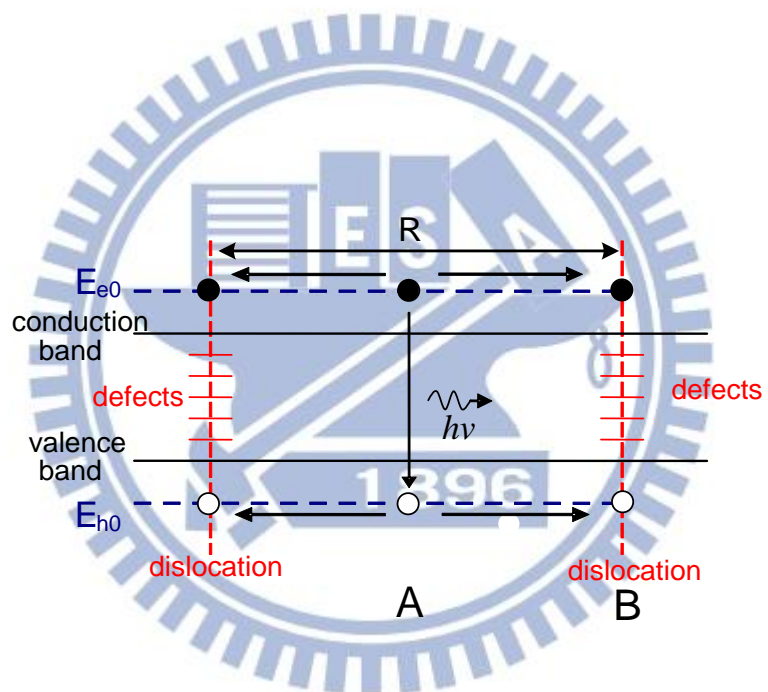


Fig. 5.7. Schematic band diagram of the recombination processes with carriers and dislocations

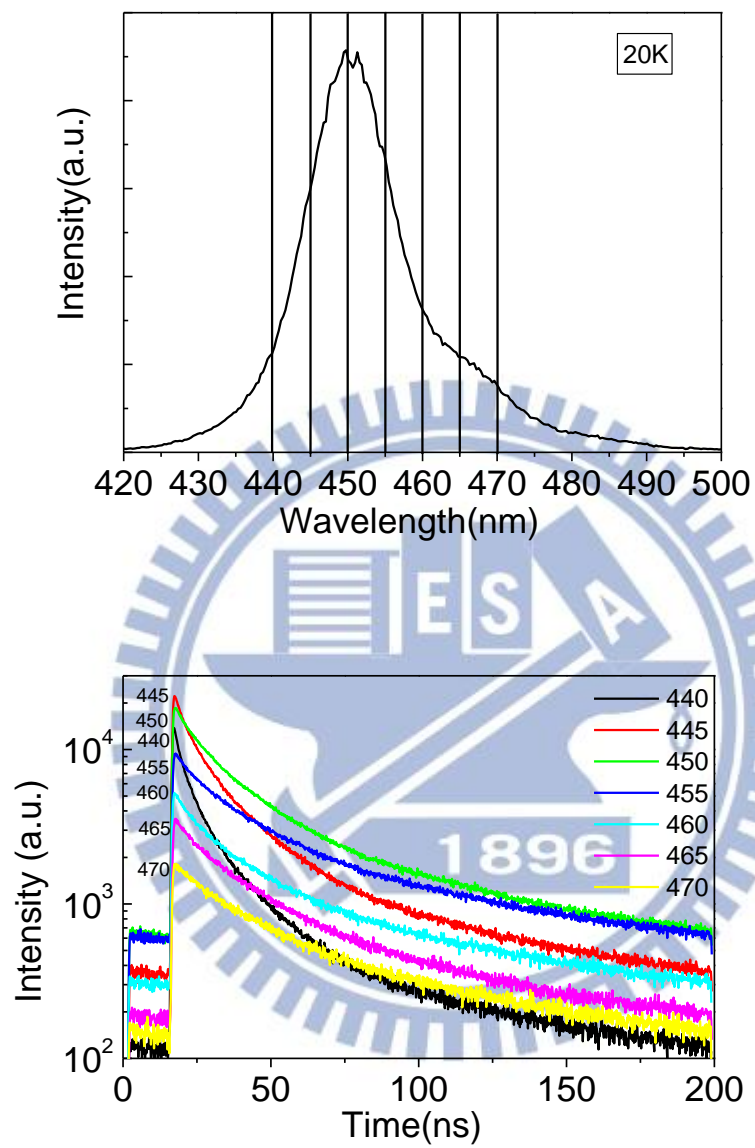


Fig. 5.8. (a) PL spectrum at 20K. (b) PL decay time as function of the emission energy

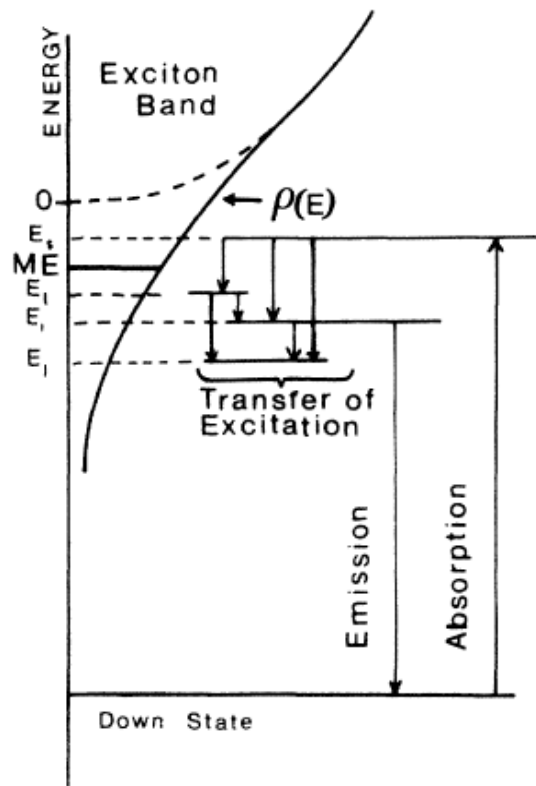


Fig. 5.9 The Schematic representation of localized excitonic states and processes in GaAs<sub>1-x</sub>P<sub>x</sub> alloys

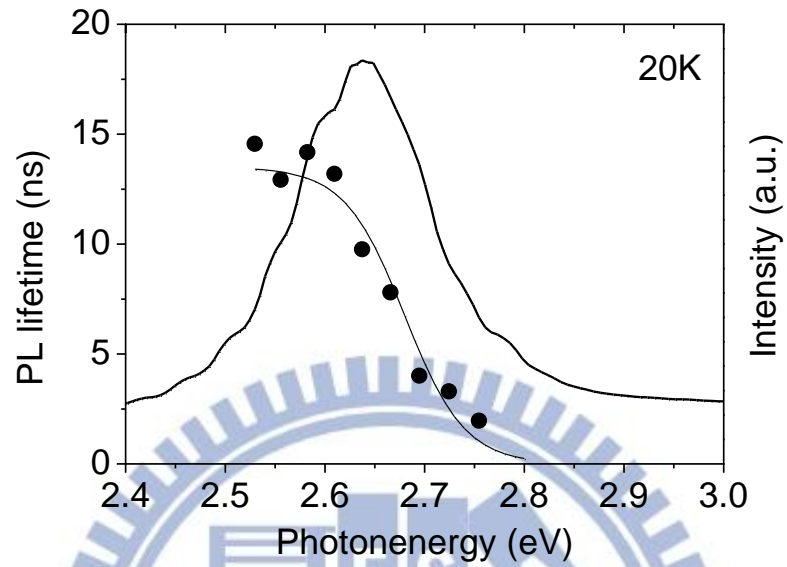


Fig. 5.10. The PL spectrum at 20K with PL decay time as function of the emission energy

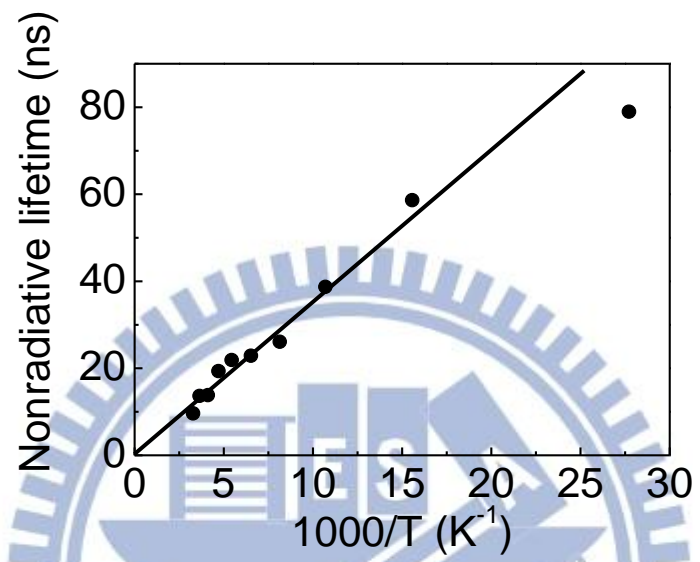


Fig. 5.11. Temperature dependence of nonradiative lifetime. The trend of nonradiative lifetime with varied temperature is controlled by diffusivity

# Chapter 6 Potential barriers and current-blocking structures induced by V-shaped pits in InGaN/GaN light-emitting diodes

## 6.1 Introduction

According to the last chapter, threading dislocations have been identified as efficient nonradiative centers. To prevent carrier diffuse toward the dislocations becomes an important issue to increase the quantum efficiency of the nitride LEDs. Hangleiter *et al.* presented a novel method that uses V-shaped pits to prevent carriers in wells from diffusing to dislocations [6]. The V-shaped pits are generated at threading dislocations under specific crystal growth conditions [7-10], and the crystal growth rate on sidewalls ( $\{10\bar{1}1\}$  planes) of V-shaped pits is much lower than that on a  $c$ -plane. Thus, quantum wells on sidewalls are thinner than those on a  $c$ -plane and produce higher electron-hole transition energies around dislocations. This high transition energy serves as a potential barrier, suppressing carriers in normal wells from diffusing into dislocations. The role of V-shaped pits in this scenario has been characterized [11-15]. However, since these V-shaped pits can extend to the surface of a wafer, they are recognized as leakage paths that may reduce the electrostatic discharge (ESD) tolerance and increase the leakage current of a device [16]. Thus, in this study, a full LED structure that comprised of V-shaped pits in the multiple-quantum-wells (MQWs) region but with a mirror-like surface achieved by tuning the growth parameters of the  $p$ -type layer was prepared. Since the voids associated with the V-shaped pits are now filled by  $p$ -type layer [9,17], the



function of the barrier formed by the different transition energies should be reexamined. The possible influence of the additional *p*-type material on the current distribution should also be considered. Thus, both of these issues are the topics of this work, and the results are presented in the follows.

## 6.2 Experiments

The samples studied herein were grown on (0001) *c*-plane sapphire substrates by low-pressure metal-organic chemical vapor deposition in a Thomas Swan system. The sample structure was shown in Fig. 6.1. First, a GaN nucleation layer was grown at 620°C. Then, a 0.5μm-thick undoped GaN buffer layer and a 3μm-thick Si-doped GaN layer were grown at 1200°C. Subsequently, a 0.65μm-thick heavily Si-doped GaN was grown at a lower temperature (950°C). The ratio of Si/Ga flow rates was 31.7 times that of the previous *n*-type layer. The conditions of the low growth temperature [9] and the high dopant concentration [10] of this layer can force the formation of V-shaped pits. Next, 9 periods of MQWs were deposited, with each period comprising a 2nm-thick InGaN well grown at 885°C and an 8nm-thick GaN barrier grown at 990°C. Thereafter, a 100nm-thick *p*-type AlGaIn electron-blocking layer and a 200nm-thick *p*-type GaN were sequentially deposited at 1080°C and 1060°C, respectively. Finally, a very thin InGaIn contact layer was grown on top of the surface at 900°C to facilitate fabrication of *p*-type ohmic contacts. Following crystal growth, one wafer was processed to form standard 180×235μm<sup>2</sup> LEDs for electrical injection measurements.

## 6.3 Transmission electron microscopy

Figures 6.2 (a) and (b) show the cross-sectional transmission electron microscopic (TEM) images of the LED structure. Because of poor migration of gallium on the (0001) plane at low temperature, V-shaped pits centered by

threading dislocations were generated after the growth of low-temperature GaN (Fig. 6.1 (a)). These V-shaped pits have a six-wall structure with the walls corresponding to the six symmetrical  $\{10\bar{1}1\}$  planes (Fig. 6.4 (a)). Figure 6.2 (b) shows a magnified image of MQWs at the periphery of a pit and figure 6.3 shows a magnified image of MQWs grown on (0001) plane. Since the crystal growth rate on the  $\{10\bar{1}1\}$  planes is slower than that on the (0001) plane when growing MQWs, wells on sidewalls were thinner than those on the top surface. However, after growing the *p*-type AlGaIn and GaN layers at high temperatures to enhance crystal growth rates on the  $\{10\bar{1}1\}$  planes, all voids associated with these V-shaped pits were filled by *p*-type layers [9,17] (Fig. 6.4 (b)), and mirror-like surfaces then formed on these wafers, as shown in Fig. 6.2 (a). Figure 6.5 (a) shows the sample structure of the TEM image and figure 6.5 (b) shows the magnified image of a V-shaped pit. The dashed line shows one quantum well, and A, B, and C identify three different points in the well, where point A is the location of the well grown on (0001) plane, point B is the boundary of the well grown on (0001) plane and on  $\{10\bar{1}1\}$  plane and point C is the location of the well grown on  $\{10\bar{1}1\}$  plane.

#### 6.4 Photoluminescence

Figure 6.6 (a) and (b) show the normal and log scale of photoluminescence (PL) spectra of the LED sample excited by a 325nm laser and measured at temperatures of 30-300K. The spectrum obtained at the lowest temperature has three emission peaks-362nm, 390nm, and 470nm. The emission with the shortest wavelength (362nm), determined based on the closeness of its energy to the band gap of GaN, is attributed to the near band edge emission of the GaN layer. Since this emission is irrelevant to quantum wells, this emission is not discussed

further. The existence of the two other emissions, 470nm and 390nm, is consistent with the observation from TEM images that two different quantum wells exist in the sample. The 470nm main peak was attributed to the thick wells grown on the normal (0001) plane, while the 390nm high-energy peak was from the thinner wells on the sidewalls of V-shaped pits. The temperature dependences of these two peaks are markedly different (Fig. 6.7 (b)). The intensity of the main peak decreased gradually as temperature increased throughout the entire temperature range. At 300K, the main peak intensity still had 25% of its lowest temperature value. In contrast, although the intensity of the high-energy peak decreased in a manner similar to the main peak when temperature was  $<100\text{K}$ , the decline was worse when temperature exceeded 120K, and the signal was indiscernible when temperature exceeded 180K. This result implies that the optically generated electron-hole pairs in these two different quantum wells behave similarly at low temperatures but quite differently at high temperatures.

To explain the origins of this difference, Fig. 6.8 shows a band diagram of a well along the dashed line presented in Fig. 6.5 (b); namely, it includes regions of the normal wells on the (0001) plane and thinner wells on the  $\{10\bar{1}1\}$  plane. In Fig. 6.8, symbols A and C are the locations of normal and thin wells, respectively, and B is the boundary of these two regions. Due to the large quantum confinement effect in the thin well, the effective band gap at point C, which includes the material band gap and zero point energies of electrons and holes, was larger than that at point A [6, 14]. This is why the energy of the 470nm main peak is 0.54eV lower than that of the 390nm high-energy peak, and this energy difference forms a potential barrier inside the wells. When the sample was illuminated by the 325nm laser, both the normal and the thin wells

can contain the optically generated electron-hole pairs. These electron-hole pairs can diffuse along the wells before they are recombined. If the temperature is very low, the diffusion coefficient  $D$  should be very small, since diffusion is a manifestation of thermally random motion of carriers. Additionally, the lifetime  $\tau$  of electron-hole pairs at low temperature should also be very short, since radiative recombination rate is inversely proportional to temperature in a two-dimensional structure [18,19]. Thus, according to the equation of diffusion length,  $\ell = \sqrt{D\tau}$ , the electron-hole pairs will not move a long distance before recombining. This is why both the main peak and high-energy peak of the sample only weakly depended on temperature when the temperature was  $<100\text{K}$ . However, as the temperature increased gradually and the diffusion length was eventually comparable to the lateral dimension of wells on the sidewalls of V-shaped pits, the temperature dependence changed drastically. Under this condition, the electron-hole pairs generated at point C in Fig. 6.8 (thin wall) can diffuse to the left to the normal quantum well and then recombine radiatively or diffuse to the right to the dislocation and then recombine nonradiatively. This is why the intensity of the high-energy peak of the sample decreased rapidly when temperature exceeded  $120\text{K}$ . On the other hand, if the electron-hole pairs are generated at point A in Fig. 6.8 (normal well), although these carriers can also diffuse a long distance, these carriers can only reside in normal wells since a potential barrier exists at point B. Thus, the main emission peak continued to exhibit excellent performance, even at room temperature. Accordingly, the internal quantum efficiency of LEDs should benefit from V-shaped pits, since the formation of a potential barrier in wells around dislocations effectively keeps electron-hole pairs in normal wells away from defective dislocation regions.

## 6.5 Electroluminescence

Figure 6.9 shows the electroluminescence (EL) spectra of an LED chip with a typical forward current of 20mA obtained at various temperatures. Similar to the PL spectra, both the high-energy and the main peaks were observed. Besides, when temperature was  $>180\text{K}$ , the intensities of both peaks decreased as temperature increased, as shown in Fig 6.10 (a). This temperature dependence is also similar to that obtained by PL measurement. However, when temperature was  $<180\text{K}$ , the intensities of these peaks increased as temperature increased, as shown in Fig 6.10 (b). Also, we compared the EL and PL spectra at different temperature. At 50K, the high-energy peak of EL spectrum is much lower than the peak of the PL spectrum, as shown in Fig. 6.11 (a). However, at 140K, both the high-energy peak of EL spectrum and PL spectrum are equal, as shown in Fig. 6.11 (b). Moreover, at 300K, both the high-energy peak of EL spectrum and PL spectrum are vanished, as shown in Fig. 6.11 (c). This temperature dependence obviously differs from that obtained by PL measurement, and should be related to the carrier injection method. The most probable reason is the high activation energy of Mg dopants that causes the  $p$ -type layer highly electrical resistive at low temperature [20]. Thus, as a current is forced to flow through the device at a low temperature, part of the injected electrons should pass through the quantum-well region and overflow to the highly resistive  $p$ -type region to compensate for the inefficient hole injection. As the temperature is increased, the overflow is reduced due to the increase of hole concentration in  $p$ -type region, and both the high-energy and the main quantum-well signals are increased [21,22].

Another significant difference between the data obtained by electrical injection and by optical excitation is the intensity ratio between the high-energy signal and the main signal. For example, at the lowest temperature, the ratio

obtained by EL (Fig. 6.12 (b)) was 0.49%, which is only 1/47 of that obtained by PL (Fig. 7(b)). This finding suggests that the ratio between the numbers of electron-hole pairs injected into the thin wells and into the normal wells by electrical current is only 1/47 of that by optical excitation [23,24]. If the optical generation rates of both wells are the same, this value corresponds to the ratio of electrical current densities between the thin wells and the normal wells. Further considering the fact that the thickness of *p*-type layer upon the thin wells is larger than that upon the normal wells, the optical generation rate of thin wells is lower than that of normal wells due to the unavoidable absorption of the excitation laser by *p*-type layer. Therefore, the ratio of current densities between the thin wells and the normal wells should be smaller than 1/47, which implies that an unintentionally formed current blocking structure that limits the current of thin wells should be present. Such a blocking structure is beneficial to the internal quantum efficiency of LEDs, since the nonradiative centers associated with threading dislocations are surrounded by these thin wells. As the temperature was increased but was still lower than 160K, a large difference of the intensity ratio (high-energy peak/main peak) between the two sets of data still existed, and the blocking mechanism should also be functioning well. However, as the temperature was higher than 160K, since the high-energy signal of PL became indiscernible, the effectiveness of this blocking mechanism cannot be determined from the present data, and another evaluating method is needed. Besides, the details of the blocking mechanism are not clear at this moment. It may be resulted from the additional *p*-type layer that filled the V-shaped pits and causes an additional resistance or a poor ohmic contact of the region upon the V-shaped. Thus, both of these two questions are left for further investigations.

## 6.6 Conclusions

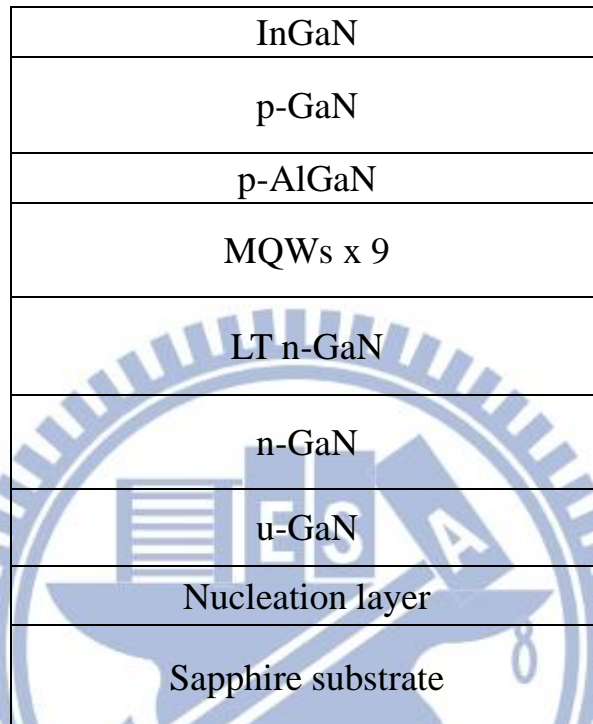
The effects of V-shaped pits on the performance of LEDs were studied. The TEM images indicate that these V-shaped pits initiated at threading dislocations and, thus, enclosed the pits. Additionally, the quantum wells grown on the sidewalls of V-shaped pits were thinner than those grown on normal regions. Due to the quantum confinement effect, the wells surrounding the threading dislocations had a larger effective band gap compared with that of normal wells grown on the (0001) plane. Accordingly, a potential barrier formed at the interface between these two wells. This barrier is beneficial to internal quantum efficiency since electron-hole pairs in normal wells cannot overcome the barrier to nonradiative dislocations. The two emission peaks in PL spectra confirmed the existence of these two effective band gaps. The energy of the barrier in the sample, based on the energy difference of these two PL peaks, was 0.54eV, which is sufficient for blocking electron-hole pairs since it is much larger than thermal energy  $KT$ , even at room temperature. The merit of this barrier is also demonstrated by the weak dependence of main peak intensity on temperature compared with that of the high-energy peak. Furthermore, the EL spectra were studied. Since the injection mechanism of electron-hole pairs by electrical current differs from that of optical excitation, an unintentionally formed current-blocking structure formed on the V-shaped pit was found by comparing the EL and PL spectra. This blocking structure effectively suppresses current flowing into the dislocations at the centers of V-shaped pits. In light of the possible paths from electron-hole to dislocations, since both are blocked either by a potential barrier in a well or current blocking structure upon a V-shaped pit, the drawbacks arising from dislocations are reduced, and the internal quantum efficiencies of nitride LEDs are improved by these V-shaped pits. However, the details of the blocking mechanism need further investigations.

## References

- [1] S. Nakamura, M. Senoh, N. Iwasa, and S. Nagahama, *Jpn. J. Appl. Phys.* Part 2 34 (1995) 797.
- [2] S. D. Lester, F. A. Ponce, M. G. Craford, and D. A. Steigerwald, *Appl. Phys. Lett.* 66 (1995) 1249.
- [3] S.J. Rosner, E. C. Carr, M. J. Ludowise, G. Girolami, and H. I. Erikson, *Appl. Phys. Lett.* 70 (1997) 420.
- [4] S. Chichibu, T. Azuhata, T. Sota, and S. Nakamura, *Appl. Phys. Lett.* 69 (1997) 4188.
- [5] A. Satake, Y. Masumoto, T. Miyajima, T. Asatsuma, F. Nakamura, and M. Ikeda, *Phys. Rev. B* 57 (1998) R2041.
- [6] A. Hangleiter, F. Hitzel, C. Netzel, D. Fuhrmann, U. Rossow, G. Ade, and P. Hinze, *Phys. Rev. Lett.* 95 (2005) 127402.
- [7] M. Shiojiri, C. C. Chuo, J. T. Hsu, J. R. Yang, and H. Saijo, *J. Appl. Phys.* 99 (2006) 073505.
- [8] J. E. Northrup, L. T. Romano, and J. Neugebauer, *Appl. Phys. Lett.* 74 (1999) 2319.
- [9] N. Sharma, P. Thomas, D. Tricker, and C. Humphreys, *Appl. Phys. Lett.* 77 (2000) 1274.
- [10] K. S. Son, D. G. Kim, H. K. Cho, K. H. Lee, S. W. Kim, and K. S. Park, *J. Crystal Growth* 261, (2004) 50.
- [11] F. Hitzel, G. Klewer, S. Lahmann, U. Rossow, and A. Hangleiter, *Rhys. Rev. B* 72 (2005) 081309.
- [12] C. Netzel, H. Bremers, L. Hoffmann, D. Fuhrmann, U. Rossow, and A. Hangleiter, *Rhys. Rev. B* 76 (2007) 155322.



- [13] D. Fuhrmann, T. Retzlaff, M. Greve, L. Hoffmann, H. Bremers, U. Rossow, and A. Hangleiter, *Phys. Rev. B* 79 (2009) 073303.
- [14] J. Abell, and T. D. Moustakas, *Appl. Phys. Lett.* 92 (2008) 091901.
- [15] K. Ding, and Y. Zeng, *Jpn. J. Appl. Phys.* 49 (2010) 028001.
- [16] C. M. Tsai, J. K. Sheu, P. T. Wang, W. C. Lai, S. C. Shei, S. J. Chang, C. H. Kuo, C. W. Kuo, and Y. K. Su, *IEEE Photon. Technol. Lett.*, 18 (2006) 1213.
- [17] S. Mahanty, M. Hao, T. Sugahara, R.S.Q. Fareed, Y. Morishima, Y. Naoi, T. Wang, and S. Sakai, *Mater. Lett.* 41 (1999) 67.
- [18] N. C. Chen, C. M. Lin, C. Shen, W. C. Lien, and T. Y. Lin, *Optics Express* 16 (2008) 20759.
- [19] E. Berkowicz, D. Gershoni, G. Bahir, E. Lakin, D. Shilo, E. Zolotoyabko, A. C. Abare, S. P. Denbaars, and L. A. Coldren, *Phys. Rev. B* 61 (2000) 10994.
- [20] W. Götz, N. M. Johnson, J. Waller, D. P. Bour, and R. A. Street, *Appl. Phys. Lett.* 68 (1996) 667.
- [21] C. M. Lee, C. C. Chuo, J. F. Dai, X. F. Zheng, and J. I. Chyi, *J. Appl. Phys.* 89 (2001) 6554.
- [22] N. C. Chen, W. C. Line, Y. S. Wang, and H. H. Liu, *IEEE T. Electron Dev.* 54 (2007) 3223.
- [23] J. Christen, T. Riemann, F. Bertram, D. Rudloff, P. Fischer, A. Kaschner, U. Haboek, A. Hoffmann, and C. Thomsen, *phys. stat. sol. (c)* 0(6) (2003) 1795.
- [24] G. Onushkin, J. Lee, J. J. Yang, S. S. Lee, I. C. Lee, M. H. Kim, and M. Koike, *phys. stat. sol. (c)* 4(7) (2007) 2814.



InGaN
p-GaN
p-AlGaN
MQWs x 9
LT n-GaN
n-GaN
u-GaN
Nucleation layer
Sapphire substrate

Fig. 6.1 Sample structure

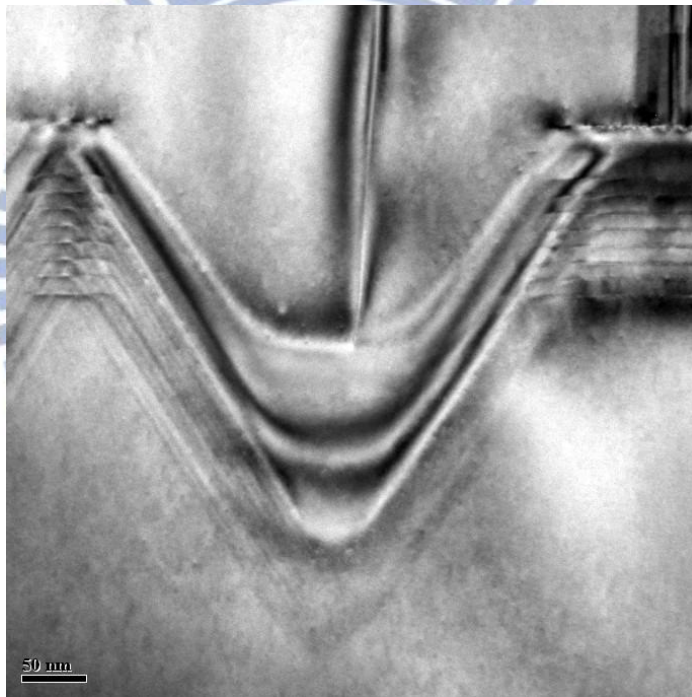
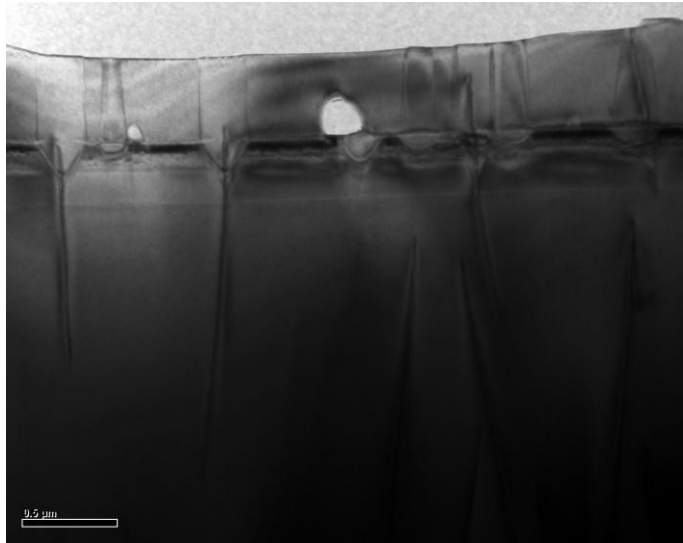


Fig. 6.2 (a) Cross-sectional TEM image of the LED structure. (b) The magnified image of a V-shaped pit. The well grown on the sidewall is narrower than that on the c-plane

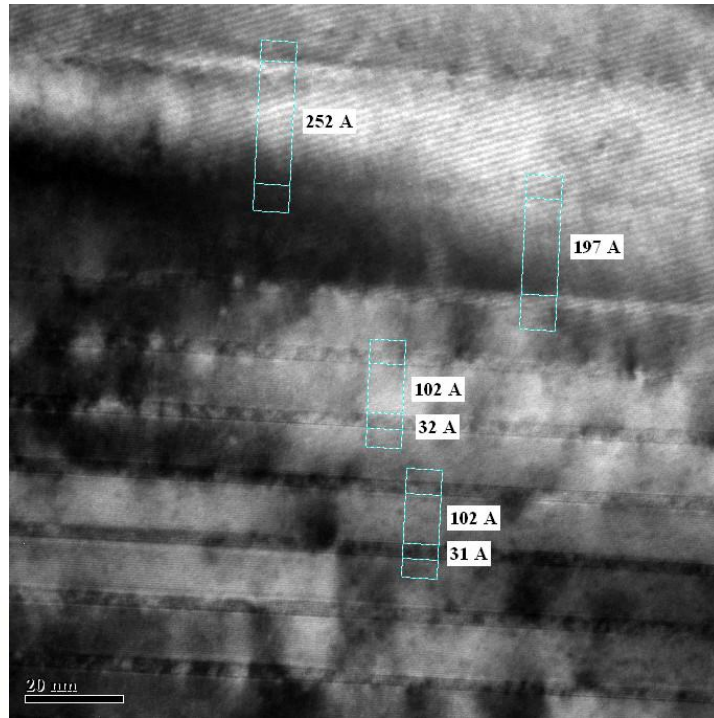
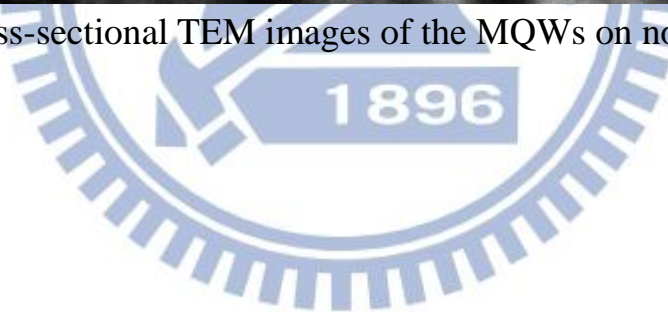


Fig. 6.3 The Cross-sectional TEM images of the MQWs on normal plane



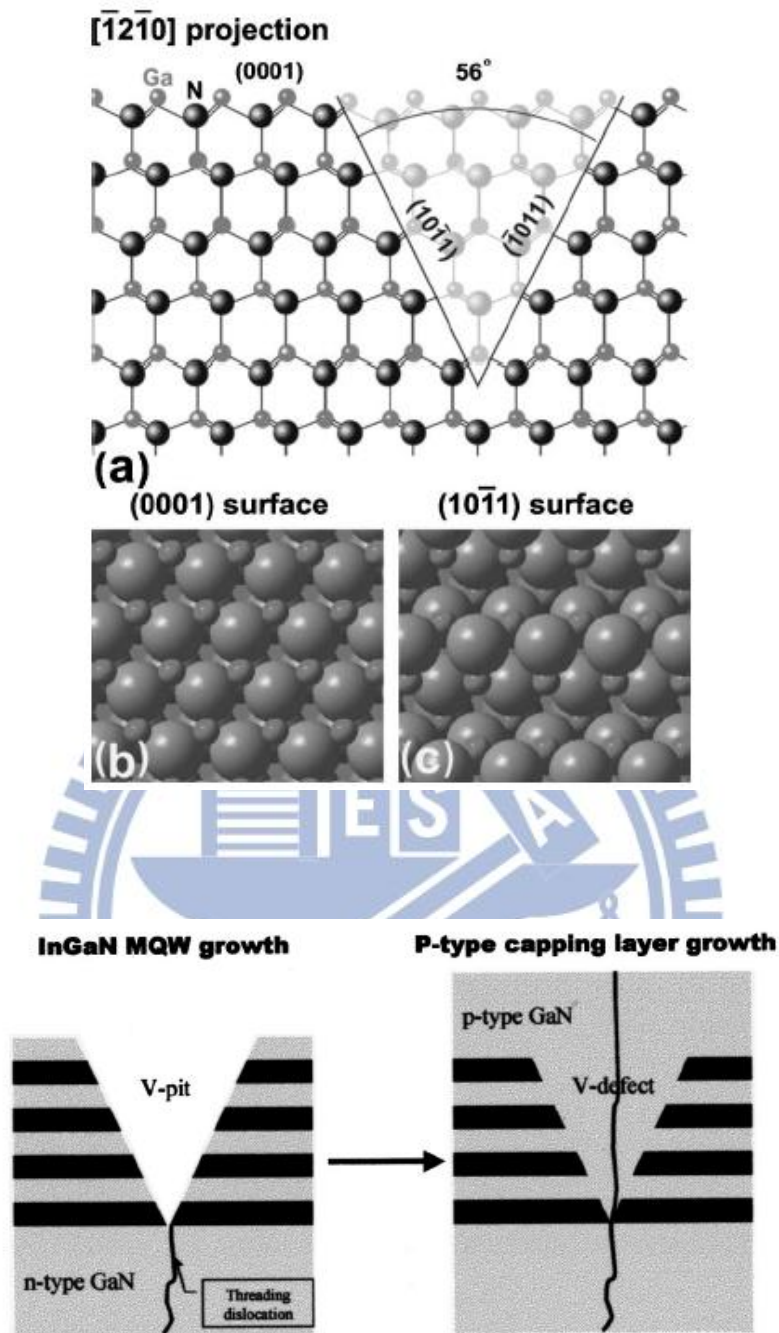


Fig. 6.4 (a) These V-shaped pits have a six-wall structure with the walls corresponding to the six symmetrical  $\{10\bar{1}1\}$  planes. [7] (b) The void associated with V-shaped pits can be filled by  $p$ -type layers [9]

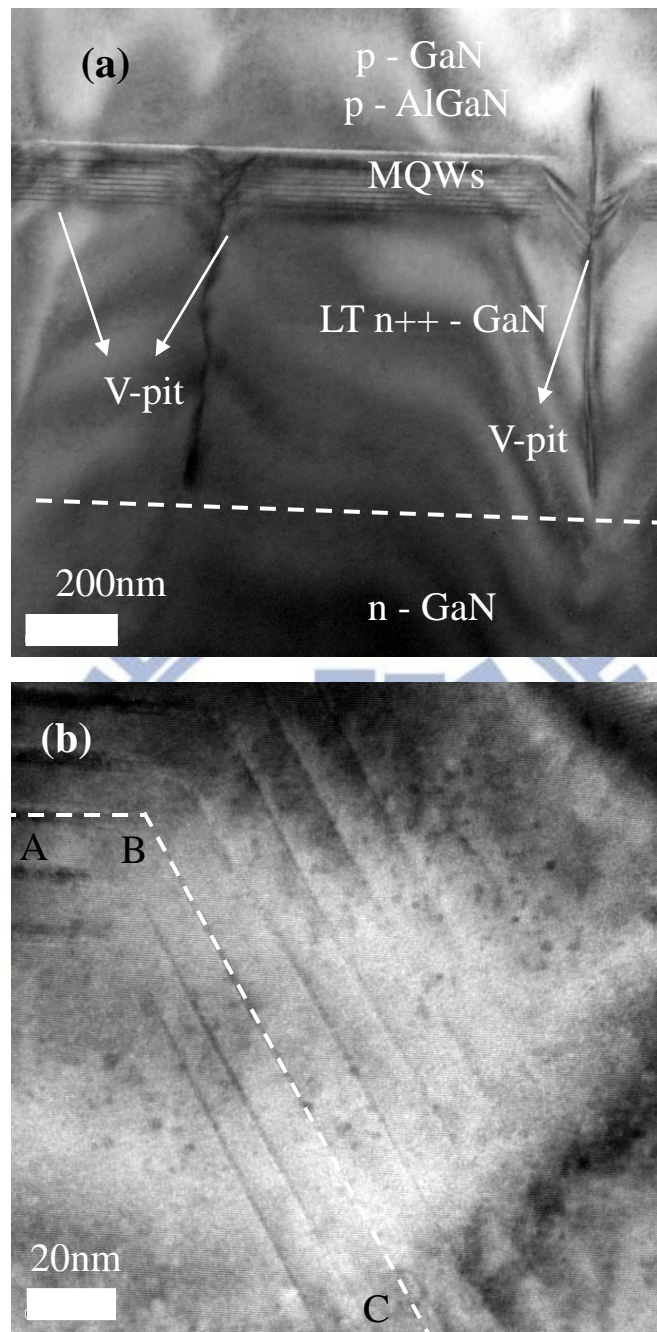


Fig. 6.5 (a) Cross-sectional TEM image of the LED structure. (b) Magnified image of a V-shaped pit. The dashed line shows one quantum well, and A, B, and C identify three different points in the well

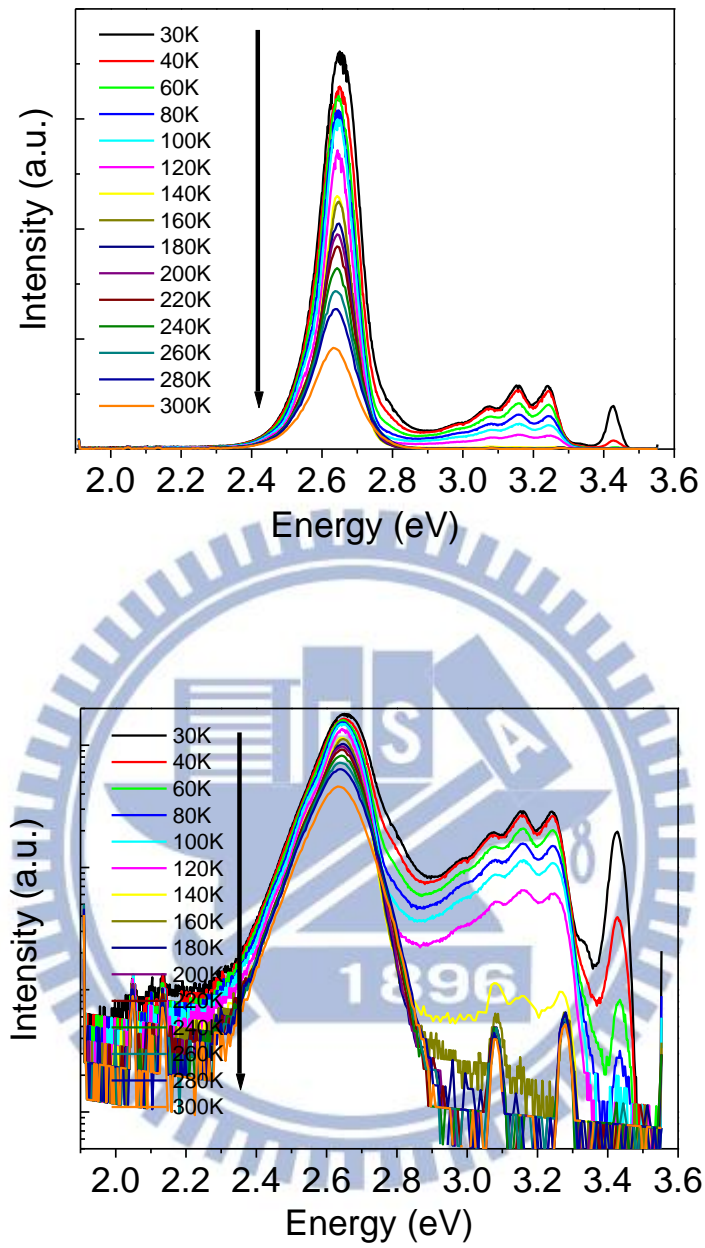


Fig. 6.6 (a) The PL spectra measured at different temperatures. (b) The log scale of the PL spectra

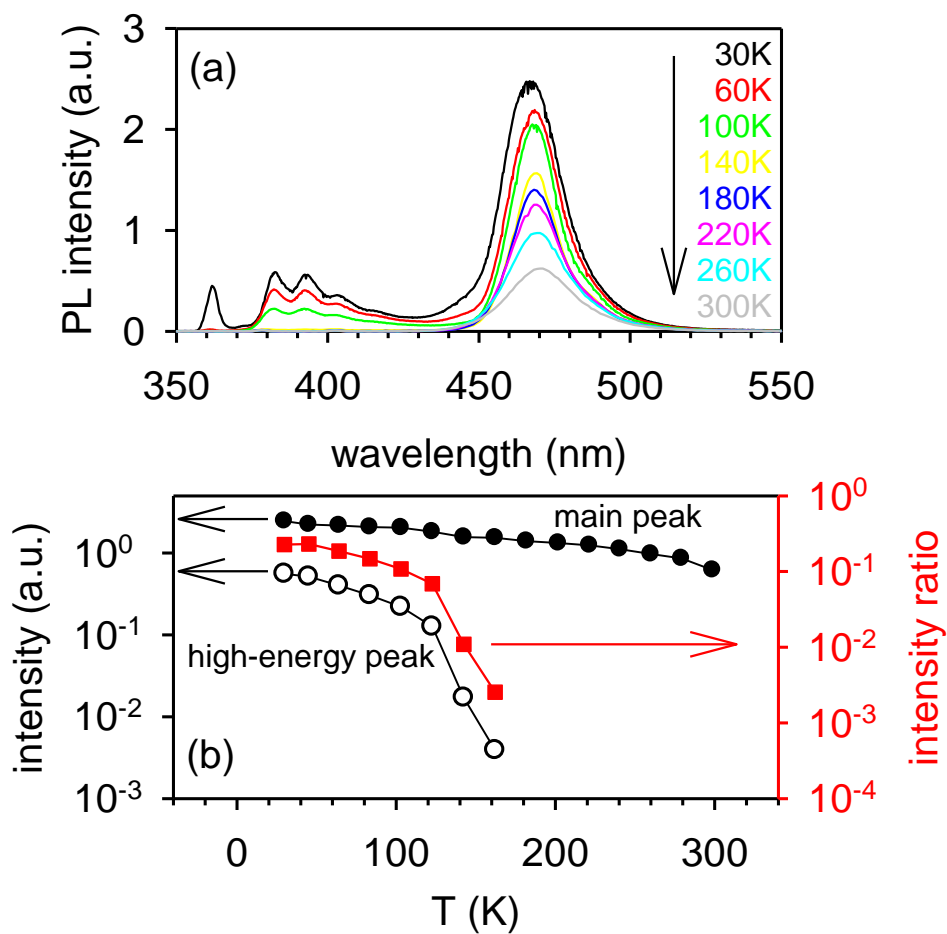


Fig. 6.7 (a) The PL spectra measured at different temperatures. (b) The PL intensities and intensity ratio of the high-energy peak and main peak in (a)



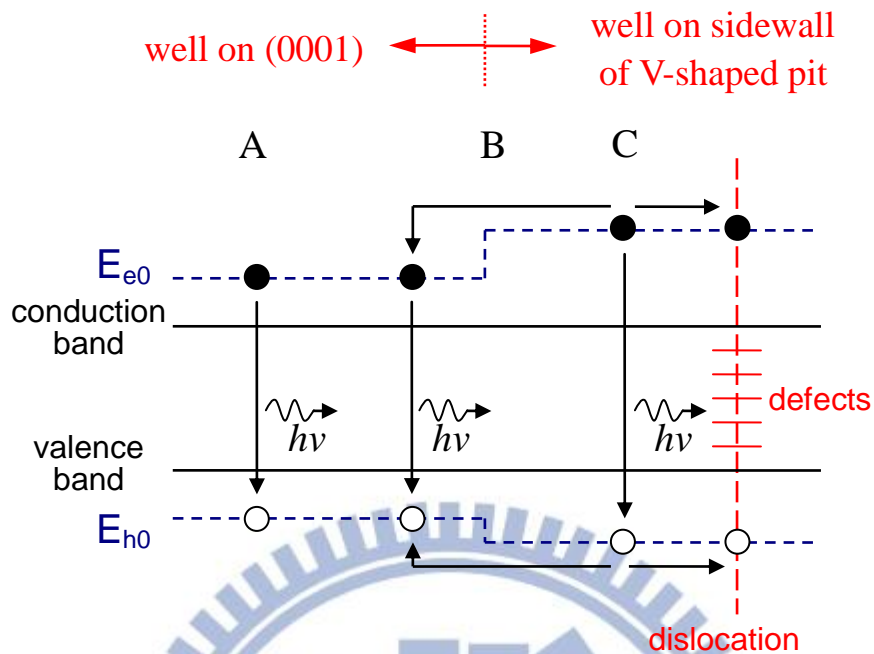


Fig. 6.8 Band diagram of the well along the dashed line (Fig. 1(b)). A, B, and C denote different points and correspond to A, B, and C in Fig. 1(b), respectively. The solid lines denote the conduction band and valence band edges, while dashed lines denote the ground-states of electrons and holes. The electrons and holes are denoted by solid and empty circles, respectively

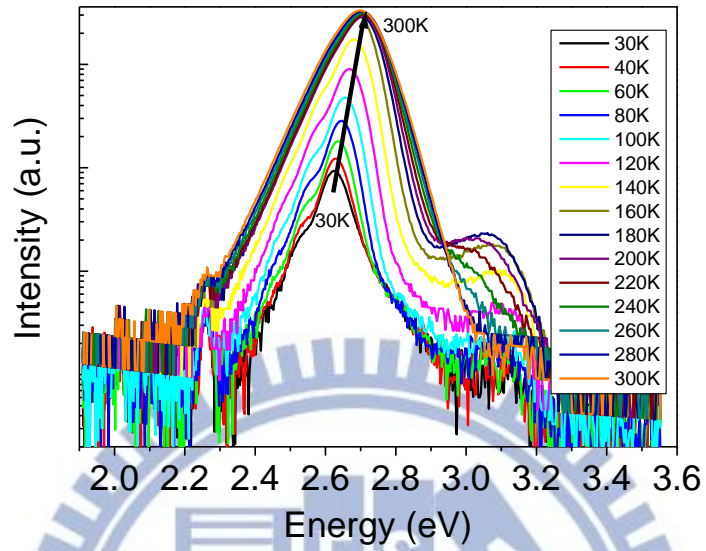


Fig. 6.9 The EL spectra of the device measured under 20mA injection at different temperatures

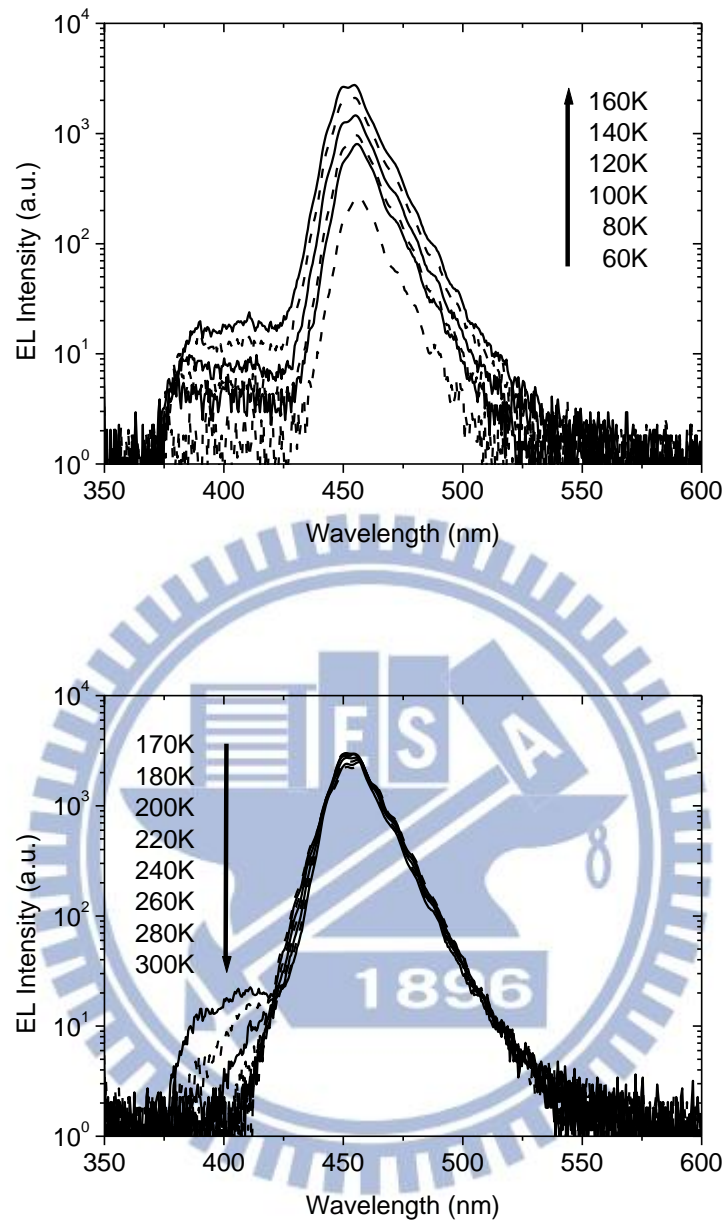
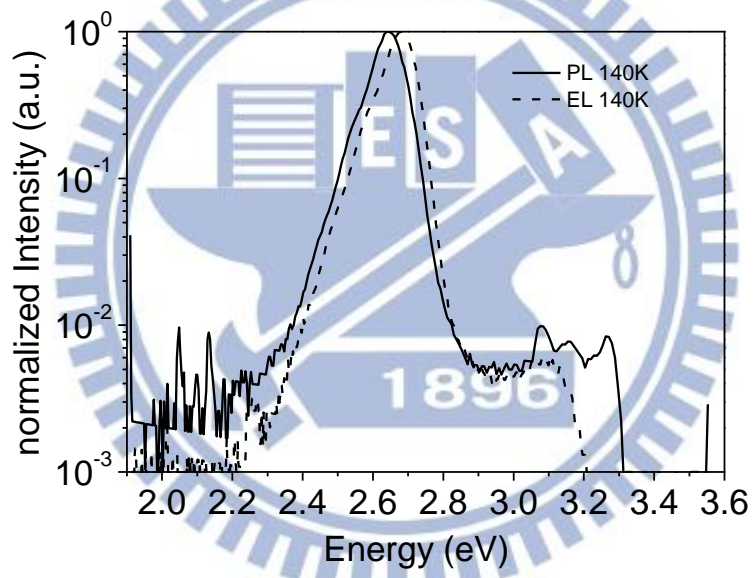
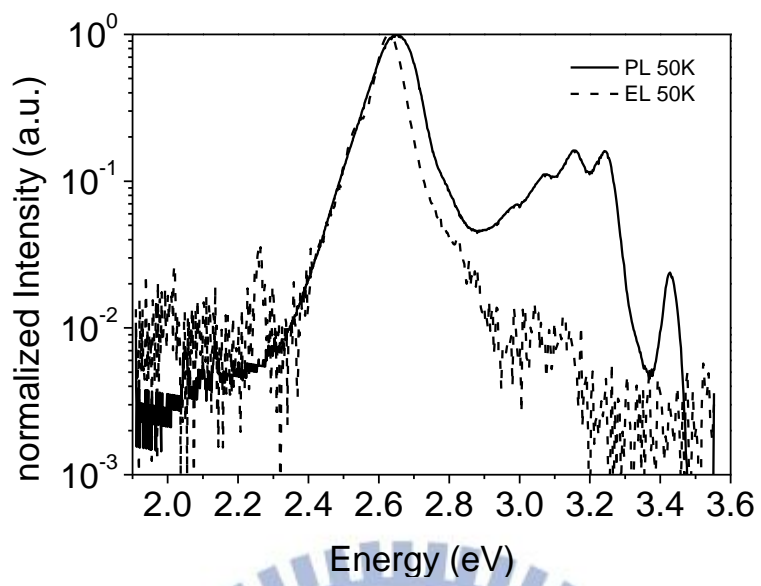


Fig. 6.10 The EL spectra of the device measured under 20mA injection in the different range of temperatures. (a) 60K - 160K (b) 170K – 300K



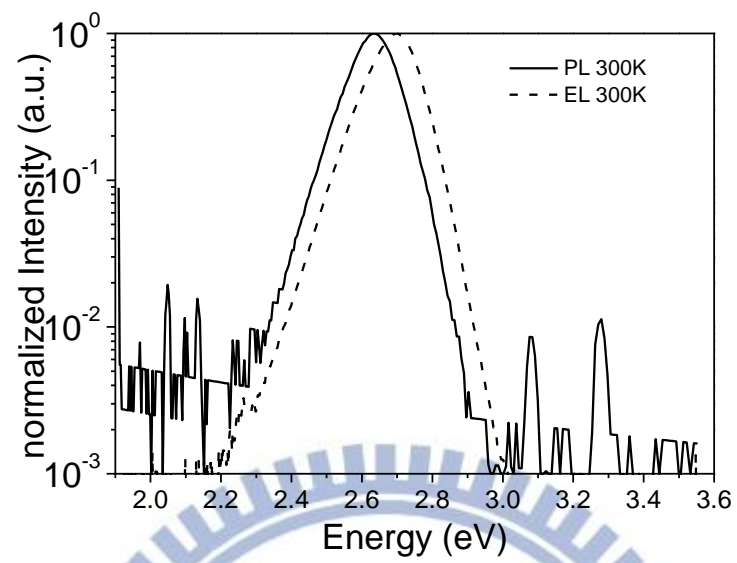
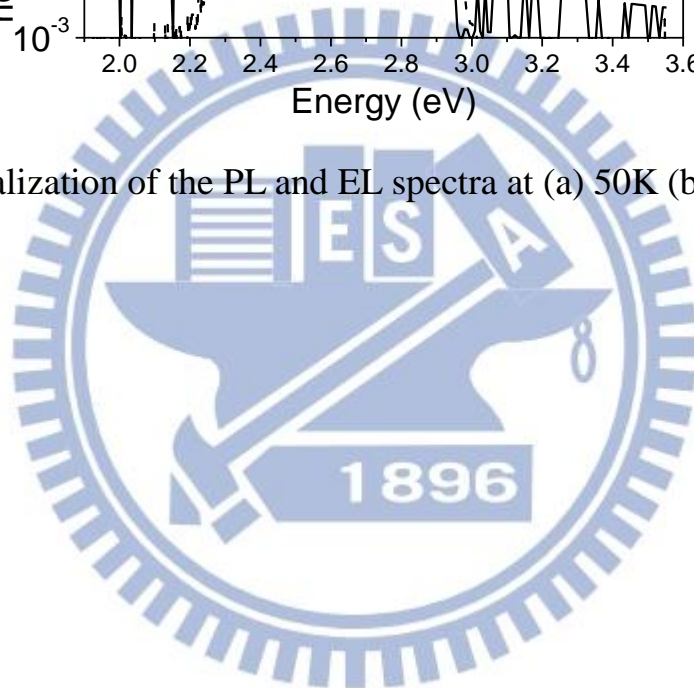


Fig. 6.11 Normalization of the PL and EL spectra at (a) 50K (b) 140K (c) 300K



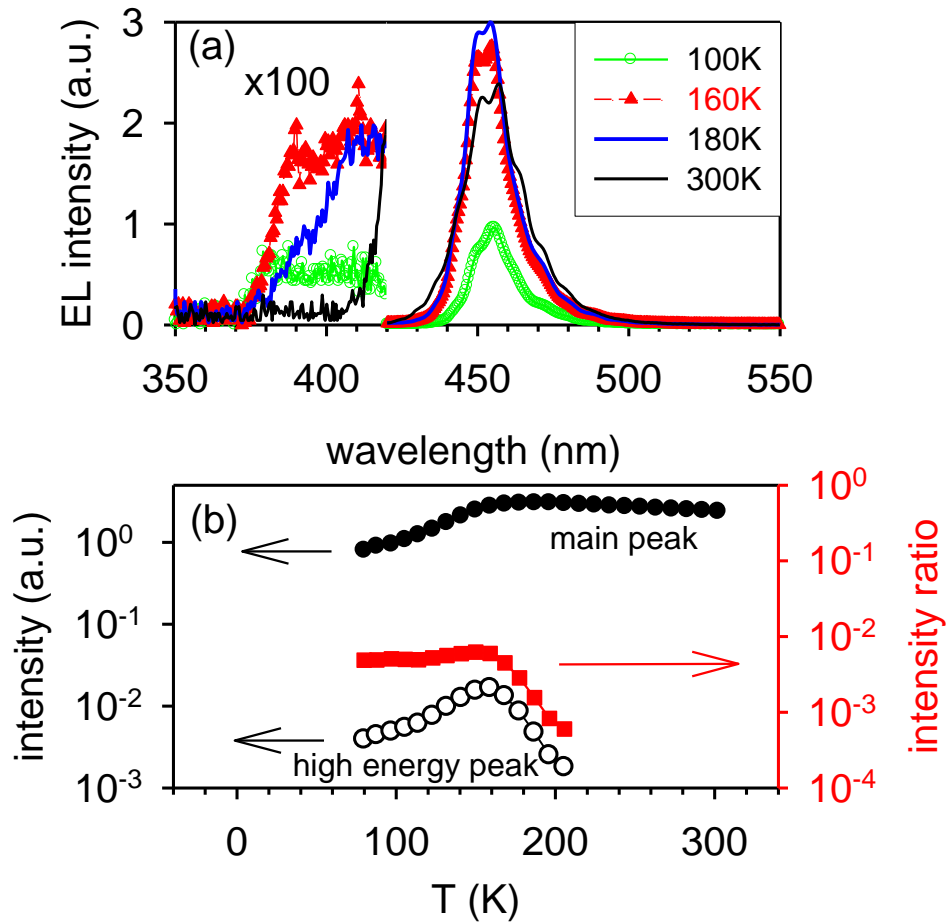


Fig. 12 (a) The EL spectra of the device measured under 20mA injection at different temperatures. (b) The EL intensities and intensity ratio of the high-energy peak and main peak in (a)

## Publish list

### Refereed Papers

1. Y. S. Wang, N. C. Chen, C. Y. Lu, and J. F. Chen, “Optical joint density of states in InGaN/GaN-based multiple-quantum-well light-emitting diodes”, Physica B. 406, 4300 (2011). (SCI)
2. M. C. Hsieh, J. F. Wang, Y. S. Wang, C. H. Yang, Ross C. C. Chen, C. H. Chiang, Y. F. Chen, and J. F. Chen, “Role of the N-related localized states in the electron emission properties of a GaAsN quantum well”, J. Appl. Phys. 110, 103709 (2011) (SCI)
3. M. C. Hsieh, J. F. Wang, Y. S. Wang, C. H. Yang, C. H. Chiang, and J. F. Chen, “Electron emission properties of GaAsN/GaAs quantum well containing N-related localized states: the influence of illuminance”, Jpn. J. Applied Phys. 51, 02BJ12 (2012). (SCI)
4. N. C. Chen, W. C. Lien, Y. K. Yang, C. Shen, Y. S. Wang, and J. F. Chen, “Spectral shape and broadening of emission from AlGaInP light-emitting diodes”, J. Appl. Phys. 106, 074514 (2009). (SCI)
5. N.C. Chen, Y.N. Wang, Y.S. Wang, W.C. Lien, and Y.C. Chen, “Damage of light-emitting diodes induced by high reverse-bias stress”, J. Crystal Growth 311, 994, (2009). (SCI)
6. J. F. Chen, C. H. Yang, R. M. Hsu, and Y. S. Wang, “Influence of thermal annealing on the electron emission of InAs quantum dots containing a misfit defect state”, J. Appl. Phys. 105, 063705 (2009). (SCI)
7. N.C. Chen, W.C. Lien, Y.S. Wang, and H.H. Liu, “Capacitance-Voltage and Current-Voltage Measurements of Nitride Light-Emitting Diodes”, IEEE T Electron Dev. 54, 3223 (2007). (SCI)

### Conference papers

#### a. International conference

1. Y. S. Wang, N. C. Chen, M. C. Hsieh, J. B. Huang, L. S. Hong, and J. F. Chen. “Elucidating the electrical characteristics of an inversion domain boundary in p-type GaN of light-emitting diodes” p-7-5 2011 Internal Conference on Solid State Devices and Materials, Nagoya, Japan, 28~30, September, 2011.
2. Y. S. Wang, N. C. Chen, and J. F. Chen, “Diffusion-controlled effects of luminescent efficiency in InGaN/GaN light-emitting diodes”, 2700-P0-6, International Quantum Electronics Conference and Conference on Lasers and Electro-Optics, IQEC/CLEO Pacific Rim 2011, Sydney, Australia, August 28 - September 1, 2011.
3. N. C. Chen, W. C. Lien, Y. K. Yang, Y. S. Wang, and J. F. Chen, “GaN grown on boron-implanted silicon (111) substrates”, G2-7, 2011 IEEE Internal NanoElectronics Conference, Chang Gung Univ., Taoyuan, Taiwan June 21-24, 2011.
4. Y. K. Yang, Y. S. Wang, J. W. Chiu, and N. C. Chen, “Heat flow properties analysis of light emitting diodes luminaire”, G11-3, 2011 IEEE Internal NanoElectronics Conference, Chang Gung Univ., Taoyuan, Taiwan June 21-24, 2011.
5. Y. C. Huang, Y. S. Wang, W. J. Wang, and N. C. Chen, “AlGaInP LEDs Reliability Dependence on Different Mg Doping Concentration”, 4700-P0-7, International Quantum Electronics Conference and Conference on Lasers and Electro-Optics, IQEC/CLEO Pacific Rim 2011, Sydney, Australia, August 28 - September 1, 2011.
6. Y.S. Wang, C. H. Chiang, W. C. Lien, Y. K. Yang, J.B. Huang, L. S. Hong, P. H. Ho, N. C. Chen, and J. F. Chen, “Effects of inversion domain in p-type GaN of Nitride light-emitting diodes” , GB16, 2009 International Electron Devices and Materials Symposia, Chang Gung Univ., Taoyuan, Taiwan 19~20, November, 2009.



7. N. C. Chen, W. C. Lien, Y. K. Yang, Y. S. Wang, J. F. Chen, T. Y. Chen, and P. H. Ho, "GaN grown on silicon (111) substrates of transferred surface morphology", GB16, 2009 International Electron Devices and Materials Symposia, Chang Gung Univ., Taoyuan, Taiwan 19~20, November, 2009.
8. Y.N. Wang, Y.S. Wang, W.C. Lien, Y.C. Chen and N.C. Chen, "Damage of light-emitting diodes induced by high reverse-bias stress", 106, The 4<sup>th</sup> Asian Conference on Crystal Growth and Crystal Technology, Sendai, Japan, 21-24<sup>th</sup>, May, 2008

**b. Domestic conference**

9. C. Y. Lu, Y. S. Wang, W. C. Lien, and N. C. Chen, "Density of States and Blue Shift of Nitride LED", OPT8-P-022, Optics and Photonics Taiwan 2010, Southern Taiwan University, 3-4, December, 2010.
10. Y. C. Huang, Y. S. Wang, and N. C. Chen, "AlGaInP LEDs Reliability Dependence on Different Mg Doping Concentration", OPT8-P-023, Optics and Photonics Taiwan 2010, Southern Taiwan University, 3-4, December, 2010.
11. 王俞授、陳乃權、張本秀，” Multipurpose-Mask for LED Device Analysis-Use Sheet resistance & Contact resistance”，2005年物理年會。
12. 王俞授、王宥楠、施權峰、張本秀、陳乃權，” 多功能MASK與LED物性量測分析”，第三屆台塑關係企業應用技術研討會， p. C-08, 2003.